Molecular Transport and Reactivity in Confinement

THU NGOC LE

A dissertation submitted in partial fulfilment of the requirements for the degree of

Doctor of Philosophy

of the

University College London

Department of Chemical Engineering

Primary Advisor: Professor Alberto Striolo

December 2016

Declaration

I, Thu Ngoc Le confirm that the work presented in this thesis is my own. Where information has been derived from other sources, I confirm that they have been properly indicated in the thesis.

To my parents
Phuong Le and Thu Do

Kính tặng bố mẹ
vì tình yêu thương vô bờ dành cho con

Acknowledgements

It is my genuine pleasure to express my deepest thanks and gratitude to my advisor **Professor Alberto Striolo**, whose expertise, support and guidance have helped me tremendously in completing my PhD study.

I would like to extend my sincere gratitude to **Professor Heath Turner** from University of Alabama for his generosity, kindness and encouragement on the most difficult topic of my study.

I would like to give immense appreciation to **Dr. Paul Ashby** from Lawrence Berkeley National Laboratory and **Professor Roy Penny** from University of Arkansas for teaching me, not only valuable academic knowledge, but also how to be a better person. Thank you for having much faith in me.

This thesis is especially dedicated to my **Father** and **Mother**, who have always been my inexorable stronghold. Being brought to the world as your daughter is the upmost divine blessing I could ever ask for in this life. To my sisters **Han Le** and **Tran Le**, I am thankful for being my upright idols, my greatest supports, and my best friends.

Last of all, I would like to give special thanks to **Shane Do**, **Rami Akkari**, **Dr. Manaswee Suttipong**, **Dr. Siddharth Gautam**, **Dr. Hieu Pham** and everyone else who, either directly or indirectly, have kindly lent their helping hands in my challenging yet rewarding venture.

Contents

List of Abbreviations

CCS	Carbon dioxide Capture and Storage
CNT	Carbon Nano Tube
COM	Center of Mass
DFT	Density Functional Theory
EISF	Elastic Incoherent Structure Factor
EOR	Enhanced Oil Recovery
FMQ	Fayalite-magnetite-quartz (mineral)
FTT	Fischer-Tropsch-Type (synthesis)
GCMC	Grand Canonical Monte Carlo (simulations)
GROMACS	Groningen Machine for Chemical Simulations (software)
HWHM	Half-Width at Half Maximum
ISF	Intermediate Scattering Function
IUPAC	International Union of Pure and Applied Chemistry (organization)
LJ	Lennard-Jones (potential)
MD	Molecular Dynamics (simulations)
MC	Monte Carlo (simulations)
MOF	Metal Organic Framework
MSD	Mean Square Displacement
NMR	Nuclear Magnetic Resonance
OCF	Orientational Correlation Functions
PBC	Periodic Boundary Conditions
PPM	Pyrite-pyrrhotite-magnetite (mineral)
QENS	Quasielastic Neutron Scattering
RDF	Radial Distribution Function
RISF	Rotational Intermediate Scattering Function
RxMC	Reactive ensemble Monte Carlo (simulations)
SANS	Small Angle Neutron Scattering
TISF	Translational Intermediate Scattering Function
TraPPE	Transferable Potentials for Phase Equilibria Force Field
VDW	Van der Waals (potential)

List of Tables

List of Figures

Abstract

For decades, tremendous efforts have been made through extensive experimental, theoretical and molecular simulated approaches to study numerous extraordinary phenomenon occur at sub-surface environments. As parts of such expedition, the works presented in this thesis employ (1) molecular dynamics (MD) simulations to investigate different structural and dynamic properties of confined fluids and (2) reactive ensemble Monte Carlo (RxMC) to explore thermodynamic properties of carbon dioxide methanation at nano-confinement. At the beginning, a series of studies by MD were conducted to examine the adsorption, structures and diffusion of (1) pure hydrocarbon and (2) mixtures of different hydrocarbons and carbon dioxide in silica pores at sub-, near-, and super-critical conditions. At equilibrium, pronounced layering was observed for propane near the pore surface. Counterintuitively, simulated MD results, in agreement with experimental quasielastic incoherent neutron scattering data, reveal that pure propane confined in silica meso-pore yields higher self-diffusivity at higher loading, isothermally. In the case of binary mixture, CO_2 preferential adsorption on the pore surface is likely to attenuate the surface adsorption of hydrocarbon, lower the activation energy for hydrocarbon diffusivity, and consequently enhance hydrocarbon mobility at low CO_2 loading. At high CO_2 loading, hydrocarbon diffusivity is hindered by molecular crowding. Hence, the non-monotonic change in hydrocarbon self-diffusion coefficients as functions of CO_2 concentration displays local maxima. On the other hand, results obtained from RxMC simulations show strong dependency of the confined reaction equilibrium conversions X_{CO_2} and equilibrium constants K_p on the pore size, pore chemistry and pore morphology. Conditions that facilitate the preferential adsorption of water on the pore walls (e.g., small pore width, high hydrophobicity of pore substrate, and rough pore surface) yield high X_{CO_2} and K_p, with the possibility of changing significantly the equilibrium composition of the reactive system with respect to bulk observations.

Chapter 1. Introduction

Nanoporous materials offer unique properties due to their high specific surface area and large specific pore volume. For example, activated carbon has a surface area of more than 3000 m^2 per gram[1] and NaX (a type of zeolite) has a pore volume of 0.26 cm^3 per gram.[2] These characteristics render them suitable for many important chemical and material science applications, including ion exchange, catalysis, gas storage, separation and purification. According to the International Union of Pure and Applied Chemistry (IUPAC) organization, nanoporous materials can be divided into three categories: micropore (<2 nm), mesopore (2-50 nm) and macropore (50 nm-1 μm).[3] Metal organic framework, zeolite and aerogel silica are both famous examples of nanoporous materials. Numerous researches have been dedicated on the synthesis, characterization, molecular modelling and design on these materials. In particularly, measuring or predicting their properties with high accuracy have been a great technical challenge. Additionally, extreme conditions at which some devices operate (i.e., high temperature and pressure) could also complicate this laboratory process. For decades, scientists and engineers have been devoting tremendous efforts to study and explore the extraordinary nature of fluids under confinement through different methods. Recently, together with the growth of computational power, atomically detailed simulations have been implemented intensively to complement experimental observation and theoretical predictions. These simulation techniques not only provide insight into physics and chemistry phenomena at the atomistic scale, but also help save time and reduce cost in preparing the materials in order to perform lab works. In addition, simulation and modelling allow scientists, in some context, to study the materials structures that have not been synthesized for exploratory purpose and provide guideline for future experimental designs.

The pseudo-algorithm for computation is presented in **Figure 1-1**, where required inputs are the structural topology and force fields that define the nature of chemical interactions. The works in this thesis use two atomistic modelling techniques, namely Molecular Dynamics (MD) and Monte Carlo (MC) simulations, whose details will be explained in the following paragraphs. The outcomes of these simulations will be either time evolution (from MD) or ensemble evolution of atomistic coordinates (from MC).

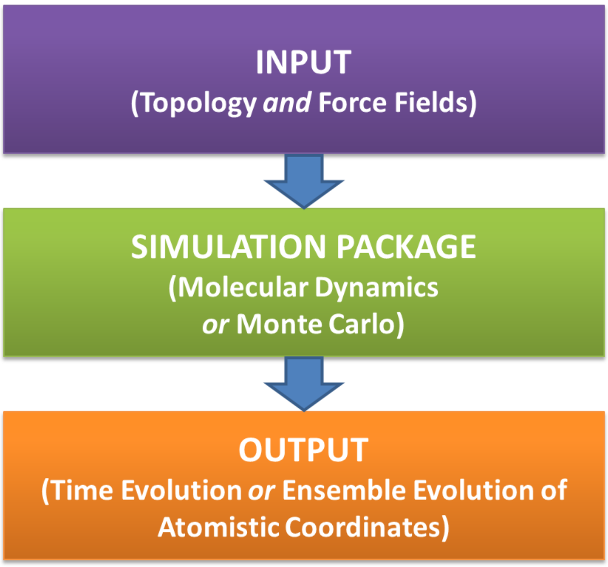

Figure 1-1 Basic molecular simulation algorithm.

In MD simulations, the *time evolution* of a system is recorded by solving Newton's second law of motion $\sum_{i\neq j}^{N} \boldsymbol{F}_{ij} = m_i \frac{d^2\boldsymbol{r}_i}{dt^2}$ where $\boldsymbol{F}_{ij}$ is the force between atom i and j; N is the total number of atoms, and m_i and $\boldsymbol{r}_i$ are the atomic mass and atomic position of atom i; and t is the time. Results in **Chapter 3** and **4** are obtained using Groningen Machine for Chemical Simulations (GROMACS) MD package, version 4.5.5.[4-5] For all MD simulations presented in this thesis, the canonical ensemble is adopted (i.e., the number of molecules N, the system volume V and system temperature T were kept constant). From the output trajectories, structural and dynamic properties of the system can be extracted, e.g., density profile, radial distribution function, diffusion coefficients and others. These results are essential to interpret the thermodynamic behaviours and transport of fluids in nano-confinement.

Unlike the MD approach, classical MC simulations are independent with time and they only involve random configurations samples of the systems. A new configuration is automatically accepted if the change in energy, $\Delta E=E^{new}-E^{old}$, is negative, which obviously suggests a favourable move. If ΔE is positive, however, the configuration is accepted with the probability $\exp(-\Delta E/k_BT)$ according to the Metropolis-Hastings algorithm, where k_B is the Boltzmann constant and T is the temperature. Hence, the final simulated outcome is the *evolution of ensembles* towards the global minimum through the three dimensional space. Depending on the purposes of studies, different MC techniques were developed, including classical MC, kinetic MC, configurational bias MC, among others. The approach used in **Chapter 5**, reactive ensemble Monte Carlo (RxMC), is an advanced technique for the investigation of chemically reactive systems with accessibility to phase change. Balance between forward and reversed reaction steps is settled to achieve equilibrium conversion, regardless of the transient states and kinetic effects. The results are useful to study the reactivity of mixtures in nano-confinement.

The main goal of this thesis is to obtain some fundamental understanding about various molecular phenomena that occur in natural processes at sub-surface environments by the means of computational simulations at the nano-scale.

Until now, the chemical engineering society has obtained quite a solid understanding about the effects of confinement on the thermodynamic and transport properties of fluids. ***Chapter 3** is dedicated to investigate the adsorption isotherms, structure and kinetics of pure propane confined within silica slit-shape nanopore.* Fortunately, experimental data are available, and rather plentiful, for the adsorption of propane in silica gel via various techniques. In this chapter, results from MD simulations are used to qualitatively interpret the experimental adsorption isotherms reported by Gruszkiewicz et al.[6] and to support part of the insights obtained using SANS by Rother et al.[7] Details concerning structural (i.e., density profiles and molecular orientation) and dynamic properties (i.e., self-diffusion coefficients and residence time of molecules at contact with the pore surface) of confined propane are then reported.

An extended work resulting from a joined project with The Ohio State University is presented in the **Appendix** where studies were carried out for pure propane confined in 20 nm silica pore at different temperatures and pressures by MD simulations in combination with quasielastic neutron scattering (QENS) experiments. The two techniques are often employed together to study the properties of confined fluids because of their unique compatibility (in term of length scale and time scale) which render direct comparison and complementary explanation between experimental results and simulated observations. Dynamic properties were quantified by the decay rates of the intermediate scattering functions (ISF).

*The examination of pure propane in silica pore by MD simulations is set as a milestone for the next studies in which binary mixtures of various n-hydrocarbons (including butane and octane) and carbon dioxide in confinement were explored. The results from these studies are reported in **Chapter 4**.* The diffusivity of fluids within materials at nanoscale is extremely important for many technical applications. Since global warming has been first noticed in

1896 by Svante Arrhenius, climate change due to high atmospheric carbon dioxide level has become the greatest environmental threat to earth.[8] Among different technologies, CO_2 capture and storage (CCS) is considered one of the most attractive alternatives.[9] According to the Global CCS Institute, thirteen large scale CCS projects are currently in operation, with another nine projects being under construction.[10] A common approach is coupling CO_2 sequestration with enhanced oil recovery, in which CO_2 can be used as an additive for tertiary oil recovery in depleted petroleum reservoirs. Much is known about structure and dynamics of carbon dioxide and methane confined in various materials such as activated carbons,[11] carbon nanotubes (CNTs),[12] and zeolites.[13-15] However, few results are available for mixtures of CO_2 and higher molecular weight hydrocarbons. Should CO_2 exhibit higher affinity to the rock formations than hydrocarbons, it could help increase production. Recently, CO_2 has been injected into basaltic formations whose high content of Ca, Mg, and Fe suggests the possibility of achieving CO_2 mineralization.[16-18] Hence, the relation between competitive adsorption and transport of CO_2 and hydrocarbons in rock formations is considered crucial to optimize both CO_2 storage capacity[19] and natural gas production.

The reactivity of confined fluids is also subjected to great interests for scientists. ***Chapter 5*** *reports the RxMC simulations employed to investigate the thermodynamic properties of the Sabatier reaction, in which CO_2 reacts with hydrogen to produce methane and water, under nanoporous confinement.* The reaction is also known as carbon dioxide methanation. The production of methane from carbon dioxide is extremely exothermic and has a net reduction in the number of moles. Thus, thermodynamically, the reaction is strongly favourable at low temperature and high hydrogen fugacity. Various studies have been conducted to address the possibility of sub-surface formations to catalyse the reaction. Some of the observations reported in the literature appear to be controversial.[20-21] Here, what has not been fully explored in sufficient details is the effect of confinement on the thermodynamics (not on the kinetics) of the Sabatier reaction. Is it possible that confinement lowers the concentration of water and hence, facilitating the production of methane in the bulk phase? Because the main goal of this study is on the thermodynamic equilibrium of the reaction conversion (and not the reaction mechanism), RxMC method[22-23] was implemented. This method has been used extensively, and only requires information regarding the thermodynamic properties of reactants and products (not of the intermediates) at ideal gas conditions (these properties are available, for example from NIST),[24] and detailed information regarding fluid-fluid and fluid-pore interactions (such information is available for the systems of interest here, although some uncertainties in the force fields are always present).

To summarize, this thesis is organized as follows.

In **Chapter 2**, detailed simulation model and methodology is provided, including (1) molecular models and force fields, (2) equilibrium MD and RxMC, and (3) result analysis explanation.

Chapter 3 reports equilibrium MD simulation employed to study the systems consisting of pure bulk propane in contact with fully protonated slit-shaped silica pores of 0.8 and 2.7 nm widths. Adsorption isotherms and excess adsorption are analysed. Details concerning structural (i.e., density profiles and molecular orientation) and dynamic properties (i.e., self-diffusion coefficients and residence time of molecules staying in contact with the pore surface) of confined propane are reported.

In **Chapter 4**, MD simulation study of different alkanes and carbon dioxide mixtures confined in slit-shaped silica pores is presented. Simulated results at thermodynamic equilibrium (in the absence of gradients) include structural (i.e., density profiles, molecular orientation, and preferential adsorption sites) and dynamic properties (i.e., self-diffusion coefficients, trajectories, and residence times at contact with the solid surface) of the confined fluids.

The thermodynamic properties of carbon dioxide methanation in the bulk phase and under confinement are studied and presented in **Chapter 5** using RxMC simulations. Results in terms of equilibrium mole fractions, reaction equilibrium conversions, and equilibrium constants are reported.

Finally, a comprehensive conclusion about the work presented in this thesis and the future outlook are provided in **Chapter 6**.

Chapter 2. Model and Methodology

This chapter provides detailed information about the molecular models and simulation methodologies. Values adopted for simulated parameters as well as comprehensive explanation for result analysis are also given thoroughly.

2.1. SIMULATION MODEL AND METHODOLOGY

Silica is chosen as the solid substrate and is used throughout all simulations presented in this thesis. It has been studied intensively by Professor Alberto Striolo's research group previously.[25-29] Silica surfaces were obtained by cutting the β-cristobalite SiO_2 crystal along the (1 1 1) crystallographic face. Because quartz (made up by SiO_4 tetrahedra structure) is an abundant mineral in earth, the cristobalite crystal with fully protonated non-bridging oxygen atoms can be considered a reasonable proxy for hydrophilic rock pore surfaces.[30] For the silica model used in this thesis, all the uncompleted tetrahedral silicon atoms were removed and the non-bridging oxygen atoms were then saturated with hydrogen atoms. The hydrogen atoms were initially put at 1 Å atop the nonbridging oxygen atoms, which is roughly perpendicular to the surface. The final configuration from hydrogen insertion yields a hydroxyl group surface density of 13.6 per nm^2. The slit-shaped pore configuration was created by placing two identical silica slabs in opposite directions, making the OH-terminated silica planes the pore inner surfaces. The supercell sizes were taken into account so that the pore is periodic along all directions. Because of periodic boundary conditions, the silica slabs are infinitely long along the X and Y directions, and separated along the Z direction by the slit-shaped pore. The solid substrate bears no net charge. Representative snapshots of the substrate from different coordinate planes are shown in **Figure 2-1**.

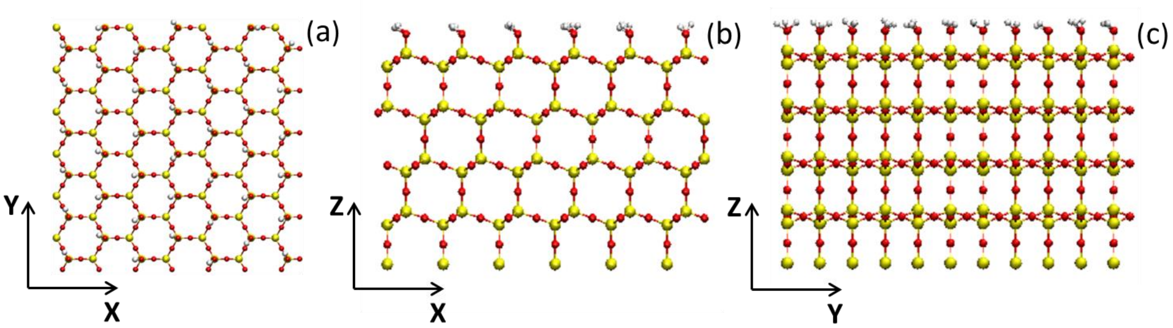

Figure 2-1 Representative snapshots for the fully protonated β-cristobalite SiO_2 crystal from different coordinate planes. (a) OH-terminated silica surfaces along X-Y axis; only the upper 2 atomic layers are shown for clarity. (b), (c) Side views of silica slabs along X-Z and Y-Z axis, respectively. White sphere is H, red is O, and yellow is Si.

Various fluids were considered for different research purposes (e.g., preferential adsorption, competitive diffusion, etc.), including different straight, saturated hydrocarbon chains (i.e., methane, propane, butane, and octane), hydrogen, carbon dioxide, and water. The fluids' simulated models, snapshots and corresponding force fields are provided in **Table 2.1**.

Table 2.1 Simulation models, snapshots and force fields for all fluids studied. Note that the sizes of the snapshots do not present true molecular and atomic sizes and ratios.

Specie	Simulated Model	Snapshot	Force Field
Hydrogen	Spherical		Huber and Herzberg[31]
Methane	Spherical		TraPPE-UA[32]
Propane	Flexible chain	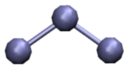	TraPPE-UA[32]
Butane	Flexible chain	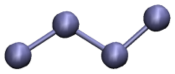	TraPPE-UA[32]
Octane	Flexible chain	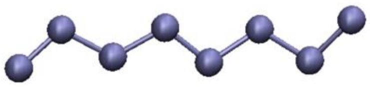	TraPPE-UA[32]
Carbon Dioxide	Rigid		TraPPE[32]

Water	Rigid	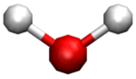	SPC/E[33]

The system total energy is obtained as the sum of the dispersive (van der Waals) interactions, E_{VDW}, the electrostatic (Coulombic) interactions, $E_{\text{electrostatic}}$, and the bonded interactions including $E_{bond\ stretch}$, $E_{angle\ bend}$, and $E_{dihedral}$

$$E_{total} = E_{VDW} + E_{\text{electrostatic}} + E_{bond\ stretch} + E_{angle\ bend} + E_{dihedral} \qquad (2.1)$$

The short-range VDW interactions is presented by the conventional Lennard-Jones (LJ) 6-12 potential

$$E_{VDW} = 4\varepsilon_{ij}\left[\left(\frac{\sigma_{ij}}{r_{ij}}\right)^{12} - \left(\frac{\sigma_{ij}}{r_{ij}}\right)^{6}\right] \qquad (2.2)$$

where r_{ij}, ε_{ij}, and σ_{ij} are the separation distance, the LJ well depth, and LJ size for the pair of atoms *i* and *j*, respectively. LJ parameters (ε and σ) for non-like components are obtained using Lorentz-Berthelot mixing rules [$\varepsilon_{ij} = (\varepsilon_i\varepsilon_j)^{1/2}$, $\sigma_{ij} = (\sigma_i + \sigma_j)/2$ where $\varepsilon_i = \varepsilon_{ii}$ and $\sigma_i = \sigma_{ii}$].[34]

The electrostatic potential between two charge particles is given by

$$E_{\text{electrostatic}} = \frac{q_i q_j}{4\pi\epsilon_0 r_{ij}} \qquad (2.3)$$

where ϵ_0 is the dielectric permittivity of vacuum while q_i and q_j are the charges of atom *i* and *j*, respectively.

Intramolecular potentials, including bond stretching and angle bending, are represented by the harmonic functions

$$E_{bond\ stretch} = k_{ij}(r_{ij} - r_{ij}^0)^2 \qquad (2.4)$$

$$E_{angle\ bend} = k_{ijk}(\theta_{ijk} - \theta_{ijk}^0)^2 \qquad (2.5)$$

where k_{ij} and k_{ijk} are the force constants, and r_{ij}^0 and θ_{ijk}^0 represent the equilibrium bond length and bond angle, respectively.

The dihedral interactions are presented by the Fourier function of proper dihedrals

$$E_{dihedral} = [C_1(1+\cos(\phi)) + C_2(1-\cos(2\phi)) + C_3(1+\cos(3\phi)) + C_4(1+\cos(4\phi))] \tag{2.6}$$

where ϕ is the angle between the ijk and the jkl planes (with i, j, k, l being the four consecutive atoms).

The CLAYFF force field[35] was implemented to simulate the silica substrate; carbon dioxide and alkane were modelled using the TraPPE-UA force field; and water was modelled as 3-site SPC/E. Within these models:

- Water is rigid with three interaction points which assumes an ideal triangular shape (H–O–H angle of 109.47°) instead of the observed angle of 104.5°;
- CO_2 is rigid with all atoms lying on a straight line. Because CO_2 is a three atomic linear molecules with an angle of 180°, using SHAKE or RATTLE constraint algorithm will cause numeric problems. Therefore, it is common for a molecular simulation package to transform this molecule into a diatomic by implementing two dummy atoms known as "virtual sites" in the middle of two C=O double bonds;
- n-alkanes are flexible molecules described by angle bending, and dihedral constraints (*no* bond stretching);
- Methyl (CH_3) and ethyl (CH_2) groups of n-alkanes are treated within the united-atom formalism in which C and H atoms of each group are incorporated into a single interaction center;
- The hydrocarbon does not bear any partial charges.

All atoms on the solid silica, except for H of the surface –OH groups, were fixed throughout the whole simulations. Non-bond and bond parameters for all substances simulated are shown in **Table 2.2** and **2.3**.

Table 2.2 Intermolecular parameters

Specie		Symbol	ε (kJ/mol)	σ (nm)	q (e)
Molecule	**Atom**				
Hydroxylated Silica	Silicon	Si	7.7E-06	0.3302	2.10
	Briging oxygen	bO	0.6502	0.3166	-1.05
	Non-briging oxygen	nO	0.6502	0.3166	-0.95
	Hydrogen	H	0.00	0.00	0.425
Hydrogen		H_2	0.3076	0.2928	0.00
Methane		CH_4	1.2297	0.373	0.00
C_nH_{2n+2}	Methyl group	CH_3	0.8148	0.375	0.00
	Ethyl group	CH_2	0.4074	0.395	0.00
Carbon Dioxide	Carbon	C	0.2245	0.28	0.70
	Oxygen	Od	0.6568	0.305	-0.35
Water	Oxygen	Ow	0.6502	0.3166	-0.8476
	Hydrogen	Hw	0.00	0.00	0.4238

Table 2.3 Intramolecular parameters

Specie	**Bond strech**			
	i	*j*	k_{ij} (kJ/mol)	r^0 (nm)
Silica	nO	H	463700	0.1
C_nH_{2n+2}	CH_3	CH_2	–	0.154
	CH_2	CH_2	–	0.154
Carbon Dioxide	C	Od	–	0.116
Water	Ow	Hw	–	0.1

Specie	**Angle bend**				
	i	*j*	*k*	k_{ijk} (kJ/mol)	θ^0 (deg)
Silica	Si	nO	H	251.04	109.5
C_nH_{2n+2}	CH_3	CH_2	CH_2/CH_3	519.6417	114
	CH_2	CH_2	CH_2	519.6417	114
Carbon Dioxide	Od	C	Od	–	180
Water	Hw	Ow	Hw	–	109.47

In addition to the conventional force field required for MD simulation used in equation (2.1), RxMC simulation involves the calculation of partition function, Q, which describes the statistical properties of a system in thermodynamic equilibrium.[36] Partition function is the sum of all possible quantum states for a system, and is a function of temperature. For an isolated molecule

$$Q(T, V, 1) = q(T, V) \tag{2.7}$$

For a system of N indistinguishable molecules

$$Q(T, V, N) = \frac{q(T, V)^N}{N!} \tag{2.8}$$

The partition function q of one isolated molecule is the product of translational and internal contributions

$$q = q_{tran} q_{rot} q_{vib} q_{elc} \tag{2.9}$$

where q_{tran}, q_{rot}, q_{vib} and q_{elc} are the translational, rotational, vibrational and electronic partition functions, respectively. Because electronic excited state energies are usually much higher than k_BT (with k_B is the Boltzmann constant), the electronic partition functions do not contribute to the thermodynamic properties except at extremely high temperature. Thus, q_{elc} is neglected in this work. The translational partition can be approximated as

$$q_{tran} \approx \sqrt{\left(\frac{2\pi mkT}{h^2}\right)^3}\, V \tag{2.10}$$

where m is the molecular mass , and h is Planck's constant. For linear polyatomic molecules, the rotational partition function is

$$q_{rot} \approx \frac{kT}{\sigma hB} \tag{2.11}$$

In the case of non-linear polyatomic molecules, the rotational partition function is

$$q_{rot} \approx \frac{1}{\sigma}\sqrt{\frac{\pi}{ABC}\left(\frac{kT}{h^2}\right)^3} \tag{2.12}$$

where σ is the symmetry number and A, B and C are rotational constant (unit of cm^{-1}).

Finally, the vibrational partition function can be approximated as

$$q_{vib} \approx \prod \frac{1}{1 - exp^{\left(-\frac{hv}{kT}\right)}} \tag{2.13}$$

where Π denotes the series product and v is the vibrational frequency.

Vibrational frequencies and rotational constants are obtained from previous literature.[37-39] **Table 2.4** shows the values for all parameters used to calculate the partition functions for different molecules considered in this thesis, together with the corresponding molecular structures and their symmetry numbers.

Table 2.4 Molecular structures, symmetry numbers, rotational constants and vibrational frequencies

Specie	**Structure**	**Symm. No.**	**Rotational Constants (cm^{-1})**			**Vibrational Frequencies (cm^{-1})**			
			A	***B***	***C***	v_1	v_2	v_3	v_4
CO_2	Linear	2	–	0.390	–	1333	667	2349	–
H_2	Linear	2	–	60.853	–	4401	–	–	–
CH_4	Spherical Top	12	–	5.241	–	2917	1534	3019	1306

H_2O	Asymmetric Rotor	2	27.881	14.522	9.278	3657	1595	3756	–

2.2. MOLECULAR DYNAMICS (MD)

MD simulation is used extensively in **Chapter 3** and **4** of this thesis and its algorithms and computational details are presented below.

2.2.1. Basic Background

MD simulation solves Newton’s second law of motion

$$\sum_{i\neq j}^{N} \boldsymbol{F_{ij}} = m_i \frac{d^2\boldsymbol{r_i}}{dt^2} \tag{2.14}$$

where $\boldsymbol{F_{ij}}$ is the force between atom i and j; N is the total number of atoms; m_i and r_i are the atomic mass and atomic position of atom i; and t is time. The equations are solved simultaneously in small timesteps, while maintaining the required temperature (for NVT ensemble) or pressure (for NPT ensemble). Although atomic mass and time step are simple and straightforward to handle, the interactions between atom i and j are extremely sensitive to the force field used and thus, it should be handled with great care.

2.2.2. MD Algorithm

MD simulation is computed based on the pair-wise potential energy calculation between all atoms within the system of interest. Currently, no analytical solution is yet available to solve the equation of motion for a molecular system. New positions and velocities for each atom are found numerically by integrating forward in time with the following procedure

(1) Give atoms initial positions $\boldsymbol{r}^{\mathrm{t}=0}$ and velocity $\boldsymbol{v}^{t=0}$ according to the Boltzmann distribution and choose short timestep δt

(2) Calculate the force $\boldsymbol{F}_i = -\frac{\partial E}{\partial \boldsymbol{r}_i}$ where E is the interaction potential from eq. (2.1)

(3) Update the atoms position $\frac{d^2\boldsymbol{r}_i}{dt^2} = \frac{\boldsymbol{F}_i}{m_i}$ and atoms position $\frac{d\boldsymbol{r}_i}{dt} = \boldsymbol{v_i}$

(4) Move time forward $t = t + \delta t$

(5) Repeat step (2), (3) and (4) for the desired duration of the simulation.

All MD simulations studied in this thesis are only considered at equilibrium and within the canonical (NVT) ensemble. After reaching equilibria, the trajectories are analyzed to produce the simulation results.

2.2.3. Leap-frog Algorithm

The leap-frog algorithm was applied to solve the equations of motion.[40] Within this algorithm, new atomic position and velocity can be calculated as

$$\boldsymbol{r}(t+\delta t)=\boldsymbol{r}(t)+\boldsymbol{v}(t+\frac{1}{2}\delta t)\delta t \tag{2.15}$$

$$\boldsymbol{v}\left(t+\frac{1}{2}\delta t\right)=\boldsymbol{v}\left(t-\frac{1}{2}\delta t\right)+\frac{\boldsymbol{F}(t)}{m}\delta t \tag{2.16}$$

Figure 2-2 below shows an illustration for the integration.

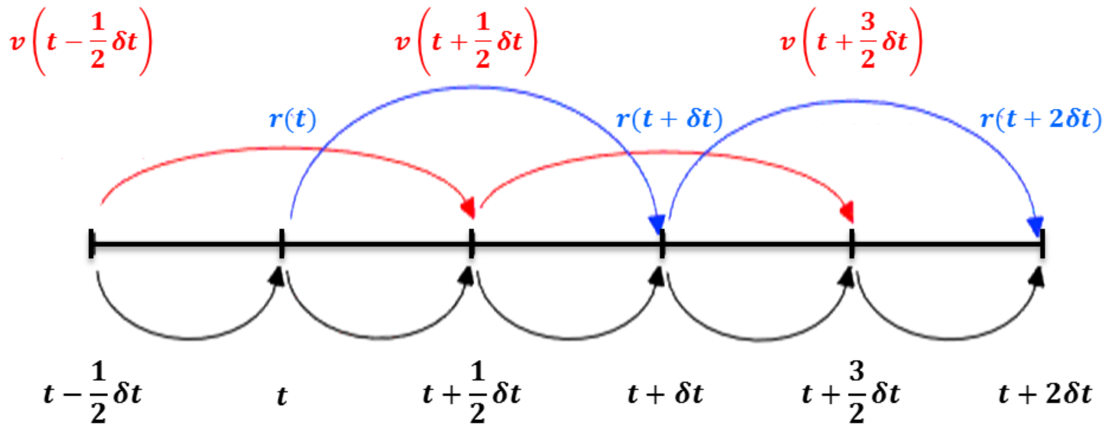

Figure 2-2 Illustration for leap-frog algorithm.

Because the positions $\boldsymbol{r}$ are computed at $(t+\delta t)$ while the velocities $\boldsymbol{v}$ are calculated at $\left(t+\frac{1}{2}\delta t\right)$, the velocities “leap over” the positions and then the positions “leap over” the velocities. The timestep δt is specified by the user and is set at 0.001 ps for all MD simulations presented in this thesis.

2.2.4. Periodic Boundary Condition (PBC) and Centre of Mass (COM) Calculation in PBC

Molecular simulation, including MD, has been widely used as a bridge to connect microscopic dynamics to macroscopic properties. Such ability is possible through the utilization of PBC where infinite system is simulated using finite simulation box (called unit cell) at nano-scale. The central simulation box (grey background box in **Figure 2-3**) is surrounded by its replicas in all directions. When a particle leaves the central box, its image enters back on the opposite side with the same velocity (i.e., no boundary effect). This technique exerts forces to the simulated particles as they are in infinite system, i.e., particles in the unit cell interact not only with other particles in the same box, but also with those in the surrounding image boxes.

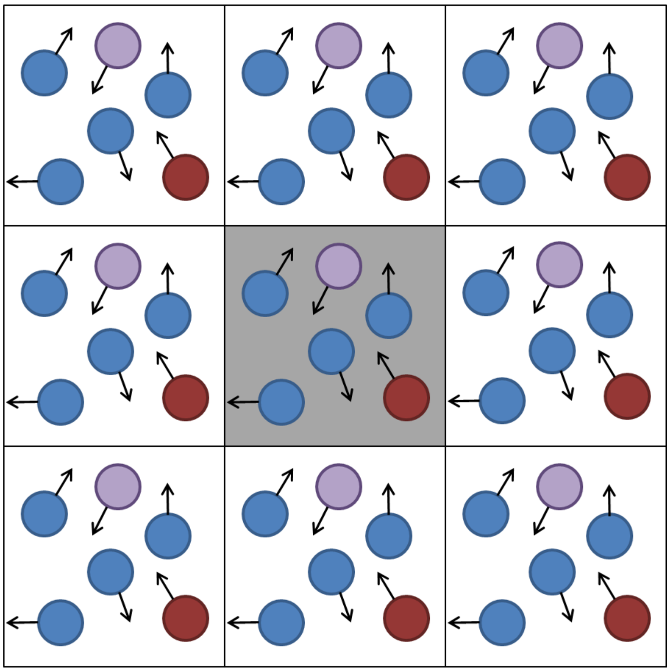

Figure 2-3 Illustration for PBC.

The implementation of PBC, however, brings complication to certain data analyses such as the COM calculation. When a large molecule or aggregate has multiple atoms span across the periodic boundary, simple calculation for COM ($r_{COM} = \frac{\sum_{i=1}^{N} m_i r_i}{\sum_{i=1}^{N} r_i}$ where r_{COM} is the COM, N is the total number of elements and m_i and r_i are the mass and position of element i, respectively) will be incorrect. A common method for computing COM for periodic systems is to convert the Cartesian coordinates into the spherical coordinates.[41] The general idea is to firstly map the Cartesian coordination r_i of all elements of the molecule/aggregate into angles θ_i in a polar coordinate; then calculate the average angle $\bar{\theta}$; and finally project $\bar{\theta}$ back into the Cartesian coordination as x_{COM}.

2.2.5. Simulation Details

All MD simulations were carried out within orthorhombic simulation boxes containing a constant number of molecules, *N*, at fixed volume, *V*, and constant temperature, *T* (i.e., the canonical ensemble). *T* of silica substrate and fluid were controlled *separately* by two Nosé-Hoover thermostats[42-43] with relaxation times of 200 fs each. Corrections for long-range electrostatic interactions were taken into account by the particle-mesh Ewald summation.[44] The cut-off distance for all interactions was set at 14 Å. The simulations were conducted using the Groningen Machine for Chemical Simulations (GROMACS) simulation package, version 4.5.5.[4-5] The leapfrog algorithm[40] with time steps of 1 fs was implemented.

2.3. REACTIVE ENSEMBLE MONTE CARLO (RXMC)

This section provides detailed description of the RxMC method for one chemical reaction performed at constant temperature *T* and pressure *P*.

Thermodynamically, reaction equilibrium is satisfied when

$$\sum_{i=1}^{S} v_i \, \mu_i = 0 \qquad (2.17)$$

where v_i and μ_i denote the stoichiometric coefficient and chemical potential of species *i* for the mixture of *S* components.

Appling the law of conservation of mass to the changes in the number of particles (N_i) due to a reaction step gives

$$N_i = N_i^0 + \, v_i \xi \qquad (2.18)$$

where ξ is the extent of the reaction. In the RxMC approach, ξ equals +1 for forward reaction step and -1 for reverse reaction step.

The grand canonical partition function, Ξ, is

$$\Xi = \sum_{N_1=0}^{\infty} \cdots \sum_{N_S=0}^{\infty} Q\,(N_i, \ldots, N_S, V, T)\, \exp(\beta \sum_{i=1}^{S} N_i \, \mu_i) \qquad (2.19)$$

where β = 1/($k_B T$) with k_B is the Boltzmann constant. The semi-classical canonical partition function, Q, can be approximated as

$$Q(N_i, \dots, N_s, V, T) = \prod_{i=1}^{S} \frac{q_i^{N_i} V^{N_i}}{N_i!\, \Lambda_i^3} \int \exp(-\beta U_{cl})\, dc^{N_1} d\omega^{N_1} \dots dc^{N_s} d\omega^{N_s}$$

(2.20)

where q_i is the internal contributions (rotational and vibrational) to the partition function of isolated molecule *i*; Λ_i is its de Broglie thermal wavelength; $U_{cl} = \sum_{\alpha=1}^{N} \sum_{\beta>i}^{N} u_{\alpha\beta} r_{\alpha\beta}$ (where $u_{\alpha\beta}$ is the pair interaction and $r_{\alpha\beta}$ is the scalar distance between site *α* and *β*, respectively) is the classical pairwise potential energy associated with the classical degrees of freedom; c = $r/(V^{1/3})$ is a set of scaled coordinates; and *ω* is a set of orientations.

Applying equation (2.20) to (2.19) gives[22]

$$\Xi = \sum_{N_1=0}^{\infty} \dots \sum_{N_S=0}^{\infty} \int \dots \int \exp\left[\beta \sum_{i=1}^{S} N_i \mu_i - \sum_{i=1}^{S} \ln(N_i!) + \sum_{i=1}^{S} N_i \ln \frac{V q_i}{\Lambda_i^3} - \beta U\right] dc^{N_1} d\omega^{N_i} \dots dc^{N_s} d\omega^{N_s}$$

(2.21)

Note that the total molecular partition function q_i is related to the molar standard chemical potential μ_i^0 by

$$\frac{\mu_i^0}{RT} = -\ln\left(\frac{q_i}{\beta P^0 \Lambda_i^3}\right) \qquad (2.22)$$

Finally, the transition probability for the reaction in either forward or reverse step, P^{ξ} can be expressed as

$$P^{\xi} = \min\left\{1, (\beta P^0 V)^{\bar{v}\xi} K^{\xi} \prod_{i=1}^{s} \left[\frac{(N_i^0!)}{\left(N_i^0 + v_i \xi\right)!}\right] exp(-\beta \Delta U)\right\} \qquad (2.23)$$

with $\bar{v} = \sum_i^s v_i$ is the net change in the total number of molecules; ΔU is the change in configurational energy; and K is the ideal-gas equilibrium constant

$$U = \frac{\int U_{cl} \exp(-\beta U_{cl}) dc^{N_1} d\omega^{N_i} \dots dc^{N_s} d\omega^{N_s}}{\int \exp(-\beta U_{cl}) dc^{N_1} d\omega^{N_i} \dots dc^{N_s} d\omega^{N_s}} \qquad (2.24)$$

$$K = \exp\left(-\frac{\sum_i^s v_i \mu_i^0}{RT}\right) \qquad (2.25)$$

where *R* is the gas constant.

It is common to combine and implement Gibbs ensemble Monte Carlo (GEMC) with RxMC to study multiple phases reaction. The technique was first considered by Johnson et al. for the dimerization reaction 2A↔B.[22] Lisal et al. later developed the reaction GEMC (RGEMC) approach which treats phase equilibrium as a special case of chemical reaction.[45-46] In this thesis, reaction equilibrium between the pore phase and the bulk phase was performed. The condition for phase equilibrium is

$$\mu_i^b = \mu_i^p \qquad (2.26)$$

where μ_i^b and μ_i^p denote the chemical potential of specie *i* in the bulk and pore phase, respectively. To ensure equality of chemical potentials between phases, the corresponding transition probability is given by

$$P^t = \min\left\{1, \left[\frac{N_i^b V^p}{\left(N_i^p + 1\right)V^b}\right] exp(-\beta\Delta U^b - \beta\Delta U^p)\right\} \qquad (2.27)$$

Lastly, random volume change in the bulk phase is performed to maintain constant bulk pressure

$$P^v = \min\left\{1, exp\left[-\beta\Delta U^b - \beta\Delta U^p + N^b ln\left(\frac{V^b + \Delta V}{V^b}\right)\right]\right\} \qquad (2.28)$$

2.4. RESULT ANALYSIS

2.4.1. Mean Square Displacement and Diffusion Coefficient, *D_s*

The random movement of fluid molecules can be quantified by the mean square displacement (MSD) which is calculated by adding the squares of the distance that molecules travel. For Brownian motion, Albert Einstein expressed the relationship between the mean square distances a molecule travels with time as[47]

$$MSD(t) = \langle|\boldsymbol{r}(t) - \boldsymbol{r}(0)|^2\rangle \qquad (2.29)$$

where $\langle\ldots\rangle$ denotes and average taken over the number of molecules as well as different time origin; $\boldsymbol{r}(t)$ and $\boldsymbol{r}(0)$ are the positions of the molecule at time *t* and time zero, respectively.

At equilibrium, the self-diffusion coefficient D_s at the fluid concentration *c* equals the slope of MSD at long observation times

$$D_s(c) = \lim_{t\to\infty}\frac{1}{2dt}\langle|\boldsymbol{r}(t) - \boldsymbol{r}(0)|^2\rangle \qquad (2.30)$$

where *d* is the number of dimensions the molecule travel in. In bulk condition, *DIM* equals three; while in narrow the silica pore, molecules movement is restricted by the pore slit-shape geometry and thus, *DIM* equals two.

Typical results present MSD for a homogeneous fluid as a function of time and its relation to the self-diffusion coefficient D_s resemble **Figure 2-4** below.

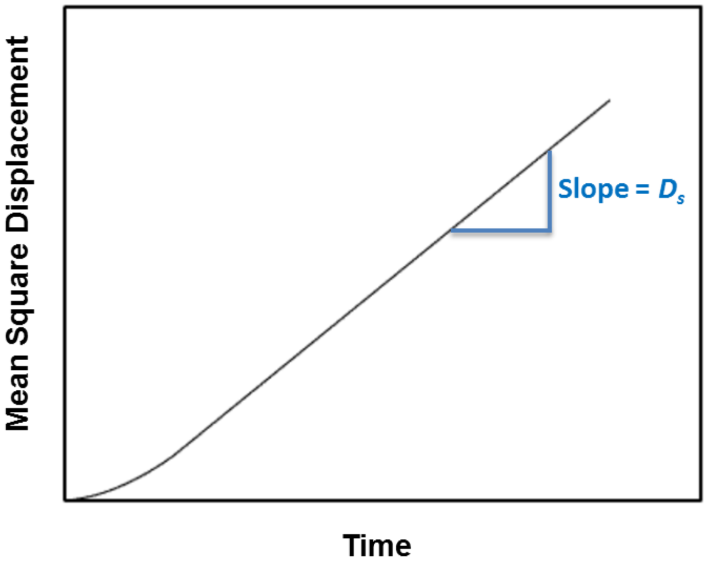

Figure 2-4 Mean square displacement.

2.4.2. Diffusion Activation Energy, E_a

In narrow confinement, the fluid diffusion, which is dominated by steric effects and solid-fluid interactions,[48] can be described as an activated process using the Arrhenius formalism

$$D(0) = D_f e^{\left(\frac{-E_a}{RT}\right)} \tag{2.31}$$

In the above equation, $D(0)$ is the self-diffusion coefficient at infinite dilution, D_f is the pre-factor, and E_a is the activation energy. For a small range of temperature, D_f can be considered constant and thus, plotting $\ln D(0)$ against $1/T$ should yield a straight line whose slope is $\frac{-E_a}{R}$.

2.4.3. Residence Autocorrelation Function, C_R

The residence autocorrelation function, $C_R(t)$, is used to quantify how long a molecule remains in contact with the solid surface and is quantified as

$$C_R(t) = \frac{\langle COM_i(t) COM_i(0)\rangle}{\langle COM_i(0) COM_i(0)\rangle} \tag{2.32}$$

where the angular brackets indicate ensemble averages, and COM_i(t) and COM_i(0) indicate the position of the centre of mass of molecule *i* at the interface at time (t) and time (0), respectively. At $t = 0$, $COM_i(t=0)$ equals 1 if molecule i belongs to the layer of interest (i.e., the first adsoprtion layer identified by the first peak near the substrate of the fluid density profile) and it remains 1 as long as that molecule remains in that layer, and becomes 0 when molecule i leaves that layer. As time progresses, $COM_i(t)$ equals 0 even if the molecule returns to the considered layer. Hence, $C_R(t)$ measures, on average, the time an adsorbed molecule spends at the interfacial layer. The slower $C_R(t)$ decays from 1 to 0, the longer fluid molecules stay in the adsorbed state. Typical results present the $C_R(t)$ as a function of time is shown in **Figure 2-5**.

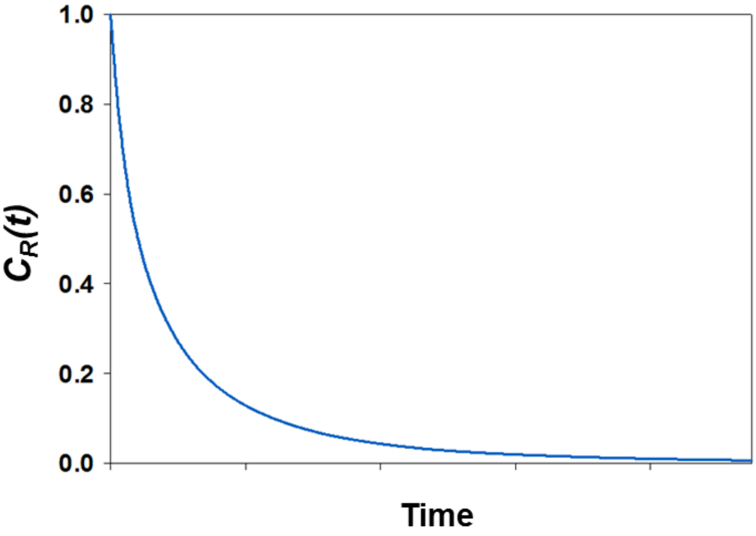

Figure 2-5 Residence autocorrelation function.

2.4.4. Radial Distribution Functions, *g(r)*

The radial distribution functions (RDFs), $g(\boldsymbol{r})$, is an important structural characteristic which describes the way atoms or molecular COMs radially pack around each other and is quantified as

$$g(\boldsymbol{r}) = \frac{1}{\rho}\langle\sum_{i\neq 0}^{N}\delta(\boldsymbol{r}-\boldsymbol{r}_i)\rangle \qquad (2.33)$$

where the angular brackets indicate ensemble averages, ρ is the average number density of particles, $\langle\sum_{i\neq 0}^{N}\delta(\boldsymbol{r}-\boldsymbol{r}_i)\rangle = \frac{dN(r)}{d^3r}$ is the average number of atoms or molecular COMs found in the volume d^3r around the position $\boldsymbol{r}$. Typical $g(\boldsymbol{r})$ for a homogenous liquid or gas as function of distance from a reference particle is shown in **Figure 2-6**.

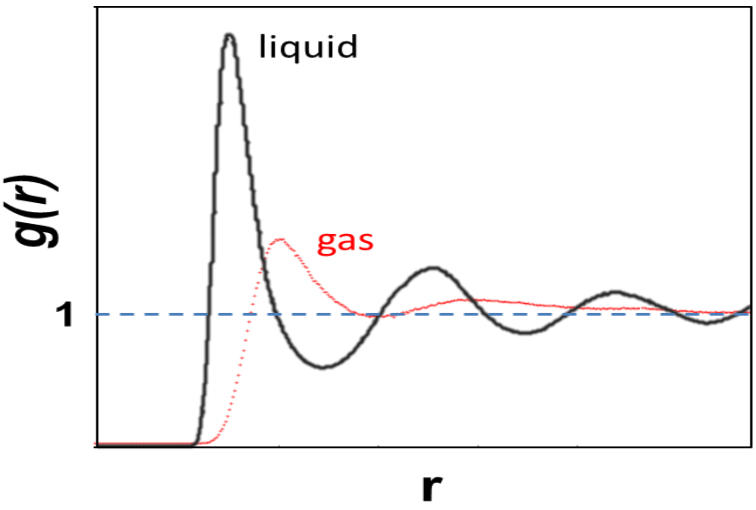

Figure 2-6 Radial distribution function of liquid versus gas.

Chapter 3. Confinement of Pure Propane

The material presented in this chapter was published in **2015** in volume *121*, pages 292-299 of the *Chemical Engineering Science* journal.

3.1. ABSTRACT

Extensive MD simulations were conducted for bulk propane in contact with fully protonated slit-shaped silica nanopores. The effective pore width was of either 0.8 or 2.7 nm. The temperature was set at 343, 368, and 373K. Each individual simulation yields the density of confined fluid as a function of the bulk pressure. For a given temperature, adsorption isotherms were estimated by repeating the simulations at various bulk pressures. The results qualitatively agree with available experimental data; namely, at fixed temperature the excess sorption is found to show a maximum near the pressure at which the pores fill; at fixed pressure the excess adsorption is found to decrease as the temperature increases and as the pore width expands. At equilibrium, pronounced layering was observed for propane near the pore surface, especially in the narrower pore and at the highest densities considered. The propane molecules at contact with silica tend to lay with their CH_3-CH_3 vector parallel to the pore surface. The mean square displacement as a function of time was used to quantify the self-diffusion coefficient of confined propane as a function of temperature, pressure and pore width. These results will be useful for enhancing the interpretation of experimental data.

In Appendix section, MD simulations were conducted for pure propane in contact with slit-shaped silica mesopores of 20 nm in width at T = 337 and 365K and P = 8 and 58 bar. Simulated results were then compared directly with experimental quasielastic neutron scattering (QENS) data for pure propane diffusion within silica aerogel at the same operating conditions.

3.2. INTRODUCTION

Nano-confinement has long been known to alter both thermodynamic and kinetic properties of the fluids within. Although methane is the most abundant component of natural gas, higher molecular weight hydrocarbons, such as ethane and propane, are much more economically attractive in the current economic landscape.[49] This work focuses on propane. Understanding the molecular features related to propane adsorption and diffusion in narrow silica-based pores might be useful for quantifying the molecular phenomena that occur in industrial processes such as catalytic conversions, and also during natural gas production following hydraulic fracturing. Several sub-surface phenomena, including hydrocarbon migration, could be better understood and predicted once the adsorption and diffusion of hydrocarbons in narrow pores are elucidated.[50]

The focus here is on adsorption isotherms for propane in narrow slit-shaped silica pores, for which experimental data are available. Grande and Rodrigues[51] measured propane adsorption in silica gel (narrow and wide pore with average pore diameter of 4.4 and 12 nm, respectively). Up to 100 kPa ≈ 10 bar, their results are consistent with type I isotherms.[52-53] In 2012, Gruszkiewicz et al.[6] used the vibrating tube densimeter to measure propane adsorption isotherms in hydrophobic silica aerogels with average pore size between 7 and 9 nm (although it is possible that the materials used had pores of size as large as 15 nm). Their results were interpreted as a function of the excess adsorption. Rother et al.[7] used small angle neutron scattering, SANS, to study experimentally the adsorption of deuterated propane at super-critical temperatures in silica aerogels with 96% porosity and specific surface area of ~700 m^2/g.

Often complementary to experiment, classical density functional theory (DFT) and molecular simulations are employed to predict the adsorption isotherms of fluids in model porous materials. Monson recently provided an overview on how classical DFT can be used to predict fluid adsorption/desorption hysteresis in mesopores.[54] This technique has been proven to be an efficient and accurate method in investigating the structure and thermodynamics of confined fluids, the density distribution during adsorption/desorption process, and also in extracting the pore size distribution from experimental adsorption isotherms.[55-56] In some cases, molecular simulations can enhance theoretical predictions.[57-58] A method often used to simulate adsorption isotherms is the grand canonical Monte Carlo (GCMC) algorithm.[59] Examples include water adsorption in carbons[60-64] and in silica pores[65] and simple fluids adsorption in various adsorbents.[66-74] In order to study the transport and structural properties of bulk and confined fluids in addition to adsorption isotherms, fewer studies have employed MD simulations.[75-77] Feng et al.,[78] for example, investigated the properties of some alkanes, including propane, over a wide range of temperature at high pressures in the bulk phase.

In this section, equilibrium MD simulations are used to study propane adsorption isotherms in slit-shaped silica pores. The results are used to qualitatively interpret the experimental adsorption isotherms reported by Gruszkiewicz et al.[6] and to support part of the insights obtained using SANS by Rother et al.[7] This section report details concerning structural (i.e., density profiles and molecular orientation) and dynamic properties (i.e., self-diffusion coefficients and residence time at contact with the pore surface) of confined propane. Consideration is made for thermodynamic conditions at which bulk propane is sub-, near-, and super-critical.

In the next section, the simulation methodology is introduced and the force fields implemented are explained. Then, the results are discussed and finally, the implications of the study are explained.

3.3. SIMULATION METHODOLOGY

Equilibrium MD simulations were carried out to compute adsorption isotherms, density profiles, molecular orientation, mean square displacements, and residence autocorrelation functions for propane in fully protonated silica slit-shaped pores. The simulations were conducted at 343, 368, and 373K, which are below, near, and above the propane bulk critical temperature, respectively. Note that the experimental critical temperature for propane (369.8K)[79] differs from that predicted by simulations (~368K)[80] when the TraPPE-UA force field is used.

Two pore widths were considered. The corresponding simulation box sizes were of 18.4×9.95×4.86 and 18.4×9.95×6.86 nm^3, respectively. The slit pore was located in the middle of the simulation box, perpendicular to the Z direction (i.e., parallel to the X-Y plane). The non-bridging oxygen atoms present on the two pore surfaces were fully protonated with a total of 960 H atoms. The solid substrate bears no net charge. Note that in **Figure 3-1** the simulation box size along the X direction is larger than the solid substrate. This is done to allow the formation of an equilibrated bulk fluid phase.

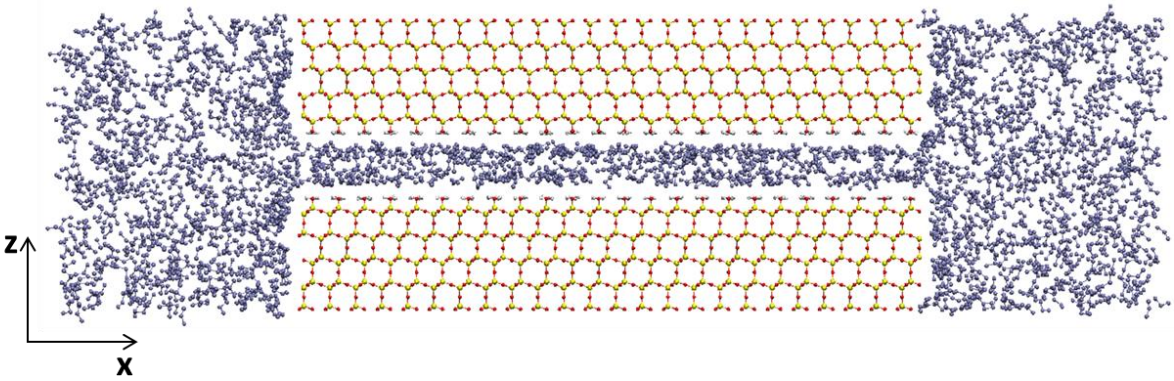

Figure 3-1 Schematic representation of the simulation box used for simulating adsorption isotherms. Purple spheres are CH_2 and CH_3 groups in n-butane, cyan is C in carbon dioxide, red is O, white is H, and yellow is Si.

Figure 3-1 presents the side view of an equilibrated system containing 2000 propane molecules with a slit-shaped silica pore of 0.8 nm at *T* = 368K. All simulations were carried out within orthorhombic simulation boxes of constant size (X = 18.4 nm, Y = 9.95 nm and Z = 4.86 nm for the narrow pore and Z = 6.86 nm for the wider pore), containing a constant number of molecules at fixed temperature (i.e., the NVT ensemble). Because periodic boundary conditions were applied in all directions, the systems considered are composed of infinite solid silica slabs along the Y direction, and separated along the Z direction by the slit-shaped pore. Along the X direction the silica substrate is ~10.4 nm in length, and the pore has two pore entrances. To quantify the adsorption isotherms only the propane molecules that were at least 3 nm away from the pore entrances are considered. The pore entrance effect which was taken into consideration is the change in propane density from the entrance to the pore to the center of the pore. **Figure 3-2** below is an example for propane density profile along X direction for the entire simulated system at 373K and 3.5 MPa, with the pore starting from 4 nm and ending at 14.4 nm. It appears that there are depletions in the density of confined propane from approximately 4.6-7 nm and 11-13.4 nm. Hence, only the ~4-nm wide region near the center of the pores along the X direction the propane density is constant and adsorption isotherms were analysed based on the the average density from approximately 7-11 nm.

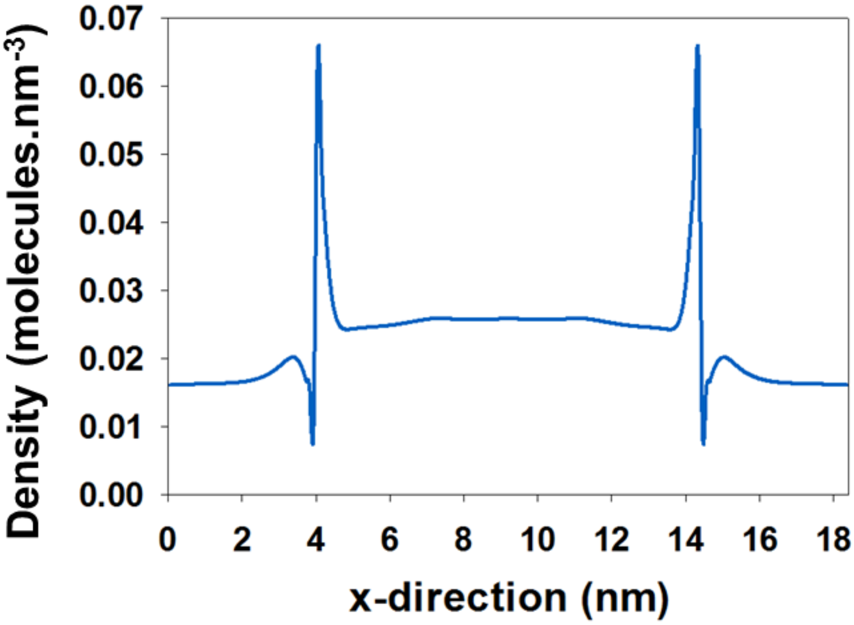

Figure 3-2 Density profile in the unit of molecules.nm^{-3} along X direction for the whole simulated box for system at 373K and 3.5 MPa.

The simulations were initiated with increasing numbers of propane molecules arranged outside the pore. As the simulations progress, some of the propane spontaneously fill the space around and between the silica slabs. Densities of bulk and confined fluids were calculated at different simulation times. Energy profiles (total energy versus time) and temperature profiles (temperature versus time) were also computed (not shown for brevity). Equilibrium was considered achieved when (1) the propane densities reached constant values (+/- 5%); and (2) both energy and temperature variations remained within 10% of their respective averaged values. Equilibration was achieved after 12 ns of simulation time for all systems investigated.

To determine the bulk propane density, only the simulation box volume outside of the pore (along the X direction) was considered. The propane density was calculated from silica pore entrance (located at X=4 nm in **Figure 3-3**) into the ‘bulk’ fluid (towards X=0 nm in **Figure 3-3**). For each simulated system, accumulation of propane near the solid was observed, while the propane density approached an approximately constant value far from the solid. This constant density (from X=0 to X~2.5 nm in **Figure 3-3**) was considered as the equilibrium bulk density, ρ_b, for each system.

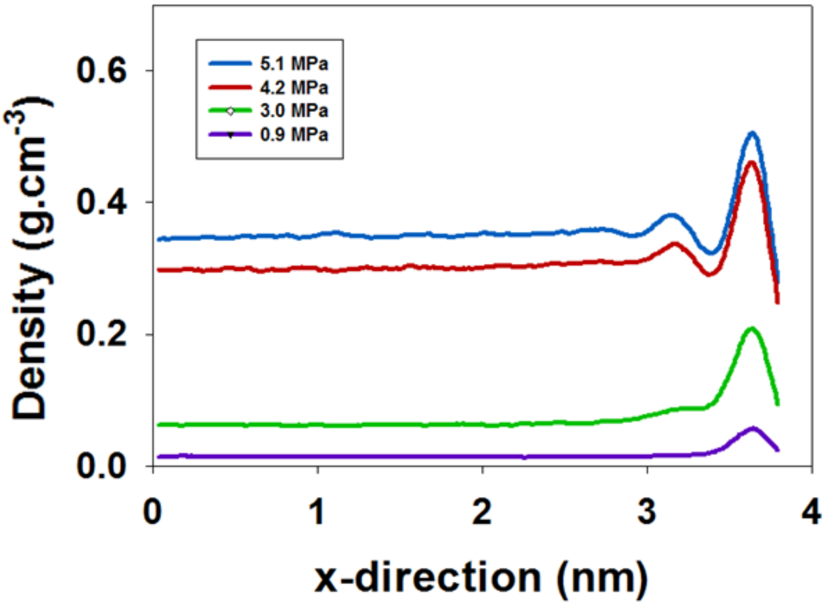

Figure 3-3 Density profiles of propane along the X direction of the simulation box, outside of the pore. The solid is located at X=4 nm in this figure. The simulations shown here were conducted for the pore of width 2.7 nm at 368K. Different curves represent results at different numbers of propane molecules, which result in different bulk pressures, as summarized in the caption.

The simulations yield the total amount of adsorbate molecules contained within the pore, n_{abs}. The excess amount adsorbed, n_{ex}, can be calculated as

$$n_{ex} = n_{abs} - V_p \rho_b \tag{3.1}$$

In equation (3.1), V_p is the effective pore volume and ρ_b is the propane density in the bulk. Estimating V_p requires to reduce the nominal pore width H (the distance between the centers of the solid atoms across the pore surface, which corresponds to 1 and 3 nm in the two pores considered here) to obtain the effective pore width, H' [81-82]

$$H' = H - 2z_0 + \sigma_{ff} \tag{3.2}$$

In equation (3.2), σ_{ff} is the averaged Lennard-Jones parameter of ethyl and methyl groups in propane, ~0.385 nm, and z_0 equals the distance at which the interaction potential between solid silica and a methyl group equals zero, ~0.292 nm and 0.323 nm for the 1 and 3 nm wide pores, respectively. The resultant H' are 0.801 and 2.739 nm (indicated as effective pore widths of 0.8 and 2.7 nm in the text). The effective pore volumes within which propane adsorbed were of ~32 and 109 nm^3, respectively.

From the bulk density ρ_b at a given T (see **Figure 3-3**), the corresponding bulk pressure was extracted by referring to the experimental isothermal properties of fluid systems from the National Institute of Standards and Technology (NIST) database.[79] For each bulk pressure estimated, the simulations described in **Figure 3-1** allowed the determination of the density of propane molecules confined within the slit-shaped pore, and therefore adsorption isotherms could be constructed.

Quantifying the dynamic properties of confined propane requires a change in the system configuration. The region outside the pores was removed, and because of periodic boundary conditions the slit-shaped pores became effectively infinite along both X and Y directions. The dimensions of the simulation boxes are 10.4×9.95×4.86 and 10.4×9.95×6.86 nm^3 for the two pores. A number of propane molecules, corresponding to a desired bulk pressure value, were arranged inside the pore to initiate the simulations. It was found that only ~8 ns were necessary for the systems to reach equilibrium (constant system energy and constant density distribution inside the pore).

All simulations were performed in the canonical ensemble (NVT) using GROMACS version 4.5.5.[4-5] Although each simulation was conducted at constant number of molecules N, several simulations were conducted for the same pore width at increasing number of propane molecules and constant temperature, T. The systems contain from 70 to 5000 propane molecules. Each simulation was run for 15×10^6 steps with a time step of 0.001 ps, corresponding to a total of 15 ns. Thermodynamic properties of adsorbed propane were analyzed during the last 3 ns of the simulations, while dynamical properties were analyzed during the last 1 ns of the corresponding simulations.

3.4. RESULTS AND DISCUSSION

Figure 3-4 show the experimental data reported by Gruszkiewicz et al.[6] for the adsorption isotherms for propane in silica aerogels, panel (a), and the corresponding excess adsorption data, panel (b). These experimental results were obtained at 343, 368, and 370K. These data will be used for qualitative comparison against the simulation results discussed below.

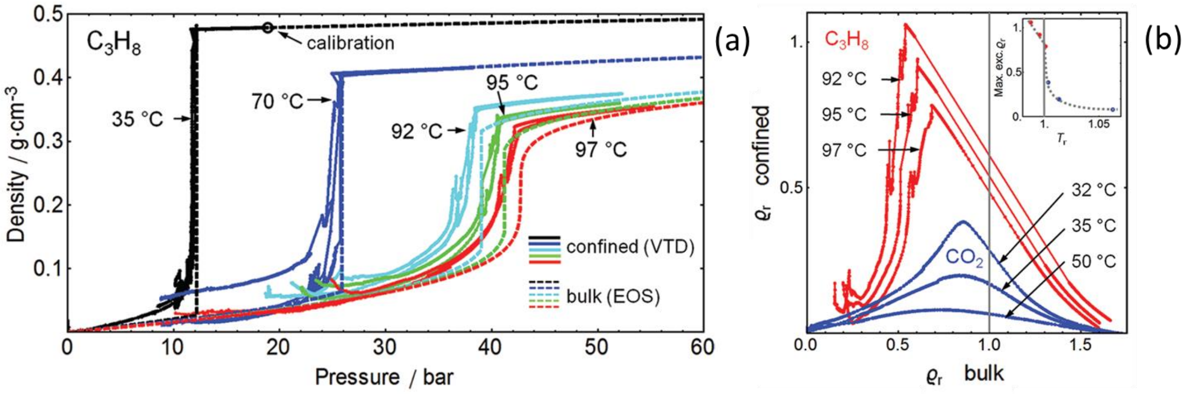

Figure 3-4 Experimental adsorption isotherms (a) and reduced excess density of propane confined in silica aerogel (b) from Gruszkiewiczet et al.[6]

3.4.1. Simulated Adsorption Isotherms

In **Figure 3-5**, panel (a) the simulated adsorption isotherms for propane in the slit-shaped silica pore of width 0.8 nm are reported. The pressure range considered for all simulations is from 0 to 6 MPa. Three isotherms were obtained at 343, 368, and 373K. In qualitative agreement with the experiments of **Figure 3-4**, the simulation results show that the confined densities (dots) are always higher than the bulk densities (lines). The excess adsorptions and the excess reduced confined density obtained from simulations are shown in panels (b) and (c), respectively. Reduced densities are estimated as ρ/ρ_c, where ρ_c=0.22 g/cm^3 for C_3H_8. The excess adsorption data show clear maxima. At low pressures, both confined and bulk propane are at low density, and the excess adsorption is low. At high pressures, both confined and bulk propane densities are high, and the excess adsorption is low. Although sometimes both experimental[6-7] and simulated[83-84] results can show negative excess adsorption at high pressures, this is not the case for our simulations. Do et al.[84] suggested that an overestimation as small as 2% of accessible volume can result in negative excess sorption. At intermediate pressures, the density of both confined and bulk propane increases. In the bulk this increase is a consequence of the gas-to-liquid transition, when *T* is below the critical temperature. In the pore this increase is a consequence of pore filling (either primary, i.e., continuous, or due to capillary condensation, depending on the pore width).[85] When, as in the systems considered here, pore filling occurs at pressures lower than those at which the gas-to-liquid transition occurs in the bulk, the excess adsorption shows a maximum. Because at super-critical conditions the transition from low density to high density bulk propane is gradual, the maximum in excess adsorption is narrower and steeper as the temperature is further below the bulk critical temperature, and it becomes gradual as *T* increases.

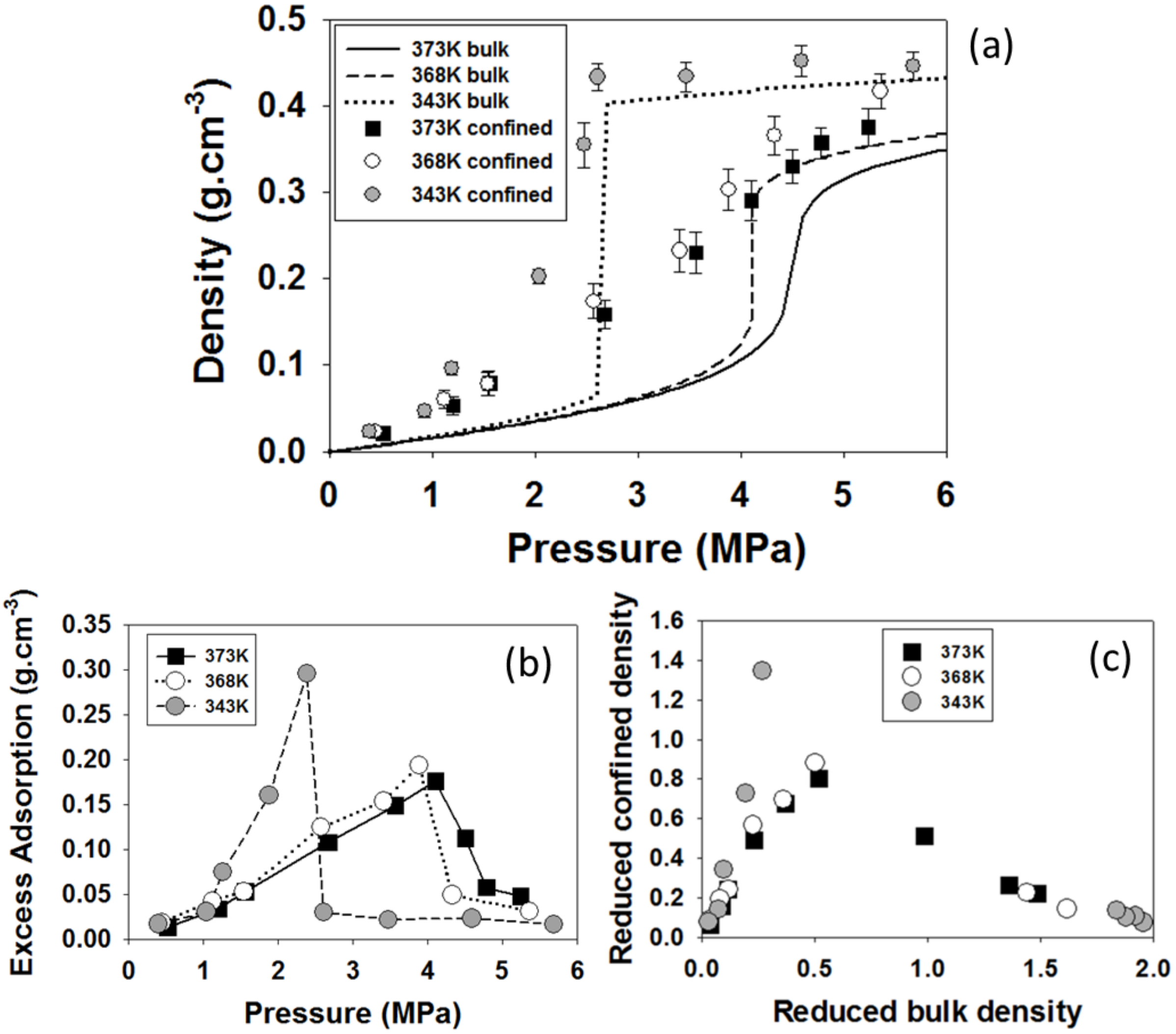

Figure 3-5 (a) Simulated densities of propane confined in the 0.8 nm silica pore (dots) and bulk (lines) propane density; (b) simulated excess adsorption as a function of bulk P; and (c) simulated excess adsorption in reduced terms. Different symbols are for results obtained at 343, 368 and 373K. Isotherms are calculated in the pressure range from 0 to 6 MPa. The lines in panel (b) are guides to the eyes.

In **Figure 3-6** panel (a), the simulated adsorption isotherms for propane at 368K for pores of width 0.8 nm and 2.7 nm are compared. At low pressures the results exhibit higher density for the propane confined in the narrower pore, as expected. In panel (b), the same data are shown in terms of the excess adsorption. These results show a maximum at intermediate pressures for both pores. As expected based on the discussion above, the maximum is more pronounced for the narrower pore, and the maximum in the wider pore is only slightly shifted to pressures lower than the gas-liquid transition in the bulk.

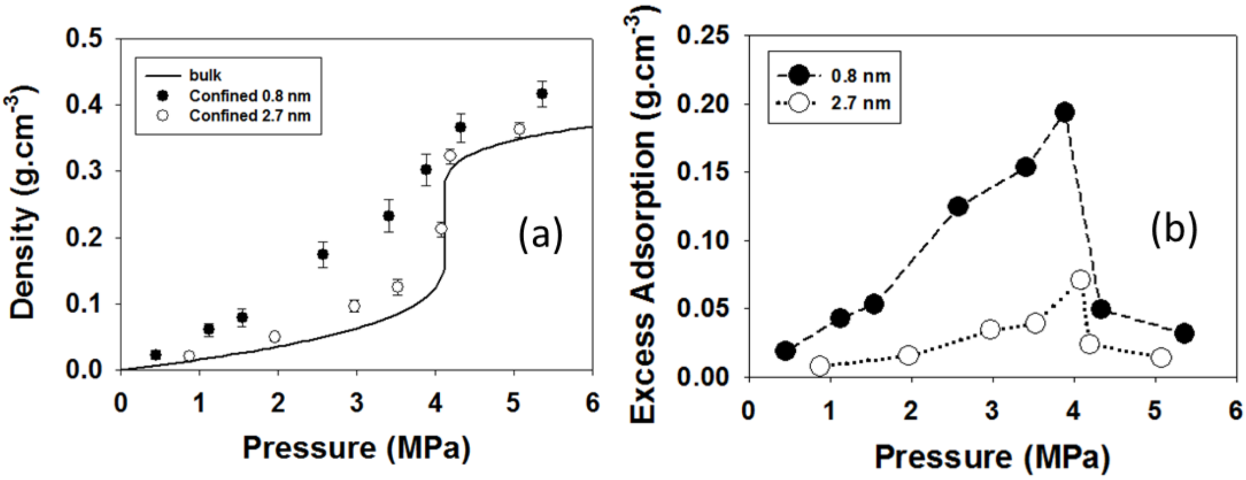

Figure 3-6 (a) Simulated adsorption isotherms of confined propane and (b) the corresponding excess adsorption in 0.8 nm and 2.7 nm silica pores at 368K. For comparison, panel (a) reports the density for bulk propane at 368 K (line). The lines in panel (b) are guides to the eye.

Although the simulation results for both adsorption isotherms and excess sorption are in qualitative agreement with experimental data,[6-7] some differences are observed. Quantitative agreement between simulations and experiments cannot be expected, as in the simulations the pores are of width 0.8 and 2.7 nm, while the experimental materials have pores of size in the range ~7-9 nm, or perhaps even larger. Additionally, the experimental pores are cylindrical while a slit-shape pore model is considered here. Based on the results in **Figure 3-6**, the difference in pore sizes leads to the expectation that the excess adsorption maxima should be more pronounced in our simulated than in the experimental data. However, this is not the case. In fact, the results for the 0.8 nm pore are comparable to those obtained from experiments. Several physical reasons might be responsible for this discrepancy. The porous materials considered in this work have their non-bridging oxygen atoms fully protonated (hence they are expected to be 'hydrophilic'),[25] while the experimental materials were described as 'hydrophobic'. However, because propane does not bear any partial charges, this difference should not lead to important consequences. The geometry of the pores differs in the two sets of data, as the pores are slit-shaped in our simulations, and highly fractal cylinders in the experimental material. The pore size distribution, typical of experimental adsorbents, will affect the data, and the pore geometry will have a strong effect on the structural and dynamical properties of the confined fluids. Because, as shown below, the simulations suggest that the excess adsorption is predominantly a surface effect, it is possible that the nature of the surfaces used in simulations and experiments is responsible for some of the differences between simulated and experimental observations. The experiments were conducted in materials with broad range of pore sizes. Thus, it is possible that the large amount of propane within the wider pores did not allow the complete characterization of those propane molecules confined within the narrower pores present in the sample, which would be more comparable to the ones simulated here.

3.4.2. Molecular Structure of Confined Propane

The simulation snapshot in **Figure 3-1** suggests that propane molecules confined in the silica pores form layers near the solid surfaces. To quantify such possibility, atomic density profiles along the direction perpendicular to the pore surface were computed. Representative results obtained for the 0.8 and 2.7 nm pores are shown in **Figure 3-7**, where distinction was made between the density of CH_3–panels (a) and (c), and CH_2–panels (b) and (d), groups of propane.

The results in **Figure 3-7** were obtained at 368K at increasing bulk pressure. For each curve in panel (a) and (b), where propane is confined in 0.8 nm pore, there are two distinct peaks with equal heights close to the two silica surfaces (symmetric with respect to the pore center). The peaks are less pronounced as the pressure decreases, as expected. The intensities of the methyl peaks are double those of the ethyl peaks in all cases, as the molar ratio for methyl to ethyl is 2:1. The fact that methyl and ethyl groups are centered at the same positions suggests that the plane containing the propane molecules is parallel to the surfaces.

Panel (c) and (d) of **Figure 3-7** show the atomic density profiles obtained for propane confined within the 2.7 nm wide silica pores at 368K. Layering is still observed, although to a much lesser extent than that observed in the 0.8 nm pore. At high pressures (4.2 and 5.1 MPa), multiple density peaks are visible, suggesting multilayer adsorption, with a rather constant propane density near the pore center. The propane density in this region corresponds, approximately, to the bulk densities at any given pressure. The fact that a part of the pore volume is occupied by propane with density similar to that of bulk propane explains the lower excess adsorption amount observed for this pore, compared to results obtained for the 0.8 nm pore at similar thermodynamic conditions (see **Figure 3-6**). The density profiles shown in **Figure 3-7** are in qualitative agreement with the interpretation of SANS data, provided by Rother et al.[7] who suggested that an adsorbed phase of thickness 1-2 molecules exists near the silica aerogels.

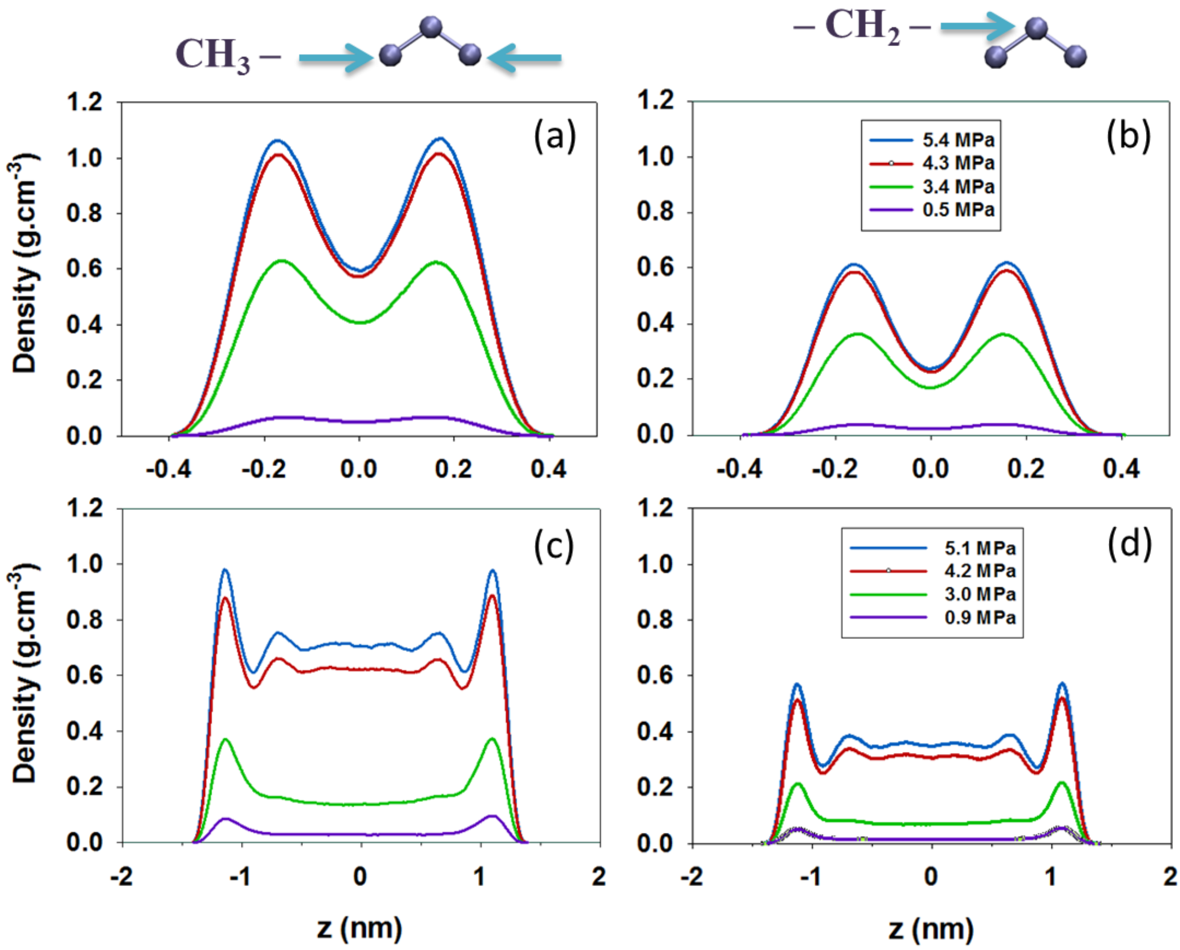

Figure 3-7 Atomic density profiles of methyl (left) and ethyl (right) pseudo-atoms of propane confined in 0.8 (top) and 2.7 (bottom) nm silica pores at 368K. Z is the direction perpendicular to the pore surface and Z=0 corresponds to the pore center. Different lines represent results at different bulk pressures.

The density profiles suggest that propane molecules in the first adsorbed layers have the tendency of laying with their molecular planes, and also their CH_3-CH_3 vectors, parallel to the surface. Such observation can be quantified by analyzing the simulation trajectories. The propane molecules within the first adsorbed layer were defined as those found within a layer 4 Å thick coincident with the density peaks near the surfaces, as identified by **Figure 3-7**. The angle formed between the CH_3-CH_3 vector of the adsorbed molecules and the vector normal to the pore surface was calculated. When the angle is either 0° or 180°, the CH_3-CH_3 vector is perpendicular to the surface, when it is 90°, the propane lays parallel to the surface.

The probability density function for the orientation angle is shown in **Figure 3-8** for propane in the 0.8 nm pore at 368K and 3.4 MPa, panel (a), and in the 2.7 nm pore at 368K and 3.5 MPa, panel (b). In both cases, the results show that propane molecules within the first adsorbed layers on both pores are never perpendicular to the pore surface, and they have a strong preference for laying parallel to the pore surface.

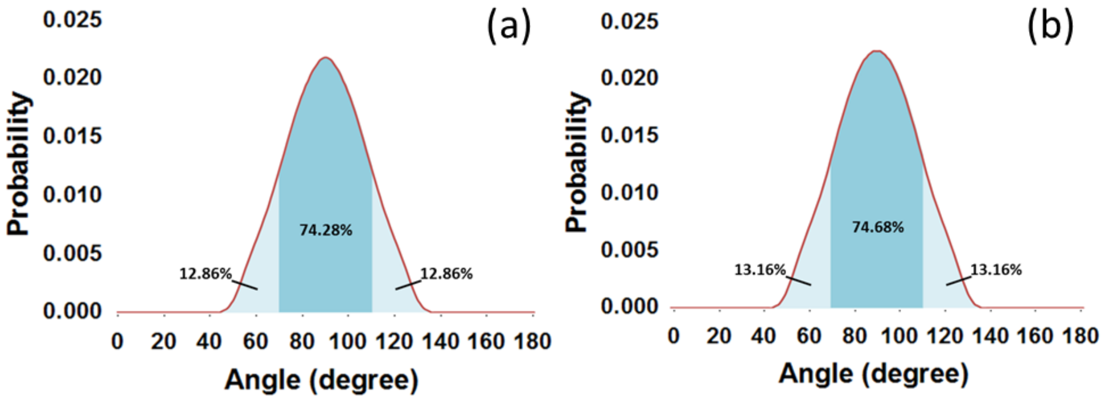

Figure 3-8 Probability density function for the orientation of propane molecules adsorbed within the first layer in (a) 0.8 nm silica pore at 368K and 3.4 MPa; and in (b) 2.7 nm pore at 368K and 3.5 MPa.

3.4.3. Dynamical Properties for Confined Propane

As the Z component of the diffusion of propane in the slit-shaped silica pores considered is negligible, the planar self-diffusion coefficient D_s is obtained by calculating ¼ the slope of the propane MSD along the X and Y directions at long observation times. Calculated propane self-diffusion coefficients are presented in **Table 3.1**. Note that for these simulations fixed amounts of propane molecules were simulated in a slit-shaped pore periodic along X and Y dimensions. The amount of propane introduced reproduced the expected amount adsorbed at pressures 1, 3, and 5 MPa (see **Figure 3-5** panel (a) and **Figure 3-6** panel (a)).

Table 3.1 In-plane self-diffusion coefficients estimated for propane confined in silica pore at various temperatures, pressures and pore sizes

Propane Planar Self-Diffusion Coefficient (10^{-4} cm^2/s)				
Pore size (nm)	**Temperature (K)**	**Pressure (MPa)**		
		1	**3**	**5**
0.8	343	7.2 ± 0.35	1.52 ± 0.05	1.50 ± 0.05
	368	9.1 ± 0.45	4.1 ± 0.1	2.10 ± 0.05
	373	10.0 ± 0.4	4.5 ± 0.1	2.30 ± 0.05
2.8	368	26.9 ± 1.4	12.1 ± 0.2	3.3 ± 0.1

In the range of investigated thermodynamic conditions, the slowest self-diffusion coefficient for confined propane was observed at the lowest temperature, 343K, highest pressure, 5 MPa, and smaller pore width, 0.8 nm. D_s increases as temperature and/or pore size increase, and as pressure decreases. These results are expected. In some cases increasing the bulk pressure has little effect on D_s. For example, at 343K, D_s obtained in the 0.8 nm wide pore is similar at 3 and 5 MPa. This occurs because the density of confined propane does not change substantially as P changes in this interval. The results for D_s of confined propane here are at first sight at odds with the results reported in the **Appendix** (in which pure propane is confined within 20 nm silica pore at T = 337 and 365K and P = 8 and 58 bar) and with experimental data reported by Wang et al.[86] for octane and decane diffusivity in microporous BPL activated carbons. At low adsorbate loadings, the adsorbate diffusivity appears to increase with pressure. The interpretation for this observation is as follows. At very low loadings, adsorbate molecules are strongly adsorbed on high-energy adsorption sites, and consequently diffuse slowly. As the amount adsorbed increases, the high-energy adsorption sites are all occupied, and adsorption occurs also on the low-energy adsorption sites. As a consequence, the adsorbate diffusion increases. This behavior is not observed in the current simulations. Possible reasons can be explained as follow. Firstly, the slit-shape silica pore simulated in this chapter has width (and correspondingly, volume) of either ~7 to 20 times smaller than the one studied in the **Appendix**. Therefore, the non-adsorbed propane in the small pore has limited space to travel (i.e., diffusion is hindered by steric effect) and D_s is directly proportional to the system pressure. Contradictorily, when the pore expands, a non-adsorbed molecule can diffuse faster and more freely with less chance to collide with its neighbours. In this case D_s is inversely proportional to the system pressure at low loading as explained above. Secondly, the adsorption of propane on the silica surfaces (hydrophobic-hydrophilic interaction) is rather mild in comparison to the adsorption of octane and decane on activated carbons (hydrophobic-hydrophobic interactions). A recent analysis of the relation between structure and dynamics of simple fluids confined in cylindrical pores has been provided by Krekelberg et al.[87] The simulation results for this system, in which no preferential adsorption sites exist for the simple fluid, are in qualitative agreement with those presented in **Table 3.1**.

For comparison, the three-dimensional D_s for propane in bulk systems at temperature and density comparable to the one for the confined fluids was calculated. In general, the results for bulk D_s is larger at low densities, and it becomes comparable, in some cases lower than D_s under confinement at high densities. Mittal et al.[88] quantified the relation between self-diffusion coefficient and density for bulk vs. confined hard spheres. The results were explained in terms of the excess entropy of the fluid molecules, with larger excess entropy leading to larger D_s. It is possible that, at large density, layering near the surfaces enhances the propane excess entropy, and hence D_s.

To quantify how long propane molecules remain in contact with the silica surfaces, the residence autocorrelation functions, $C_R(t)$, were computed for propane molecules within the first adsorption layer within the 2.7 nm pore. The algorithm is described in **Chapter 2**. The position of the CH_2 group of propane is considered as the position of one molecule. The faster C_R decays from 1 to 0, the shorter fluid molecules stay in the adsorbed layer. In **Figure 3-9**, results obtained at various conditions are reported. These results do not show large variations as a function of T and P. However, the data suggest that propane molecules stay longer at contact with the solid substrate at low T and low P. As T increases at P = 3 MPa, as expected,[89] C_R decreases faster. At 368K, C_R decreases faster as P increases. These data suggest that exchanges between propane molecules in the center of the pore and those adsorbed on the surface are facilitated by high propane density in the pore and by high T.

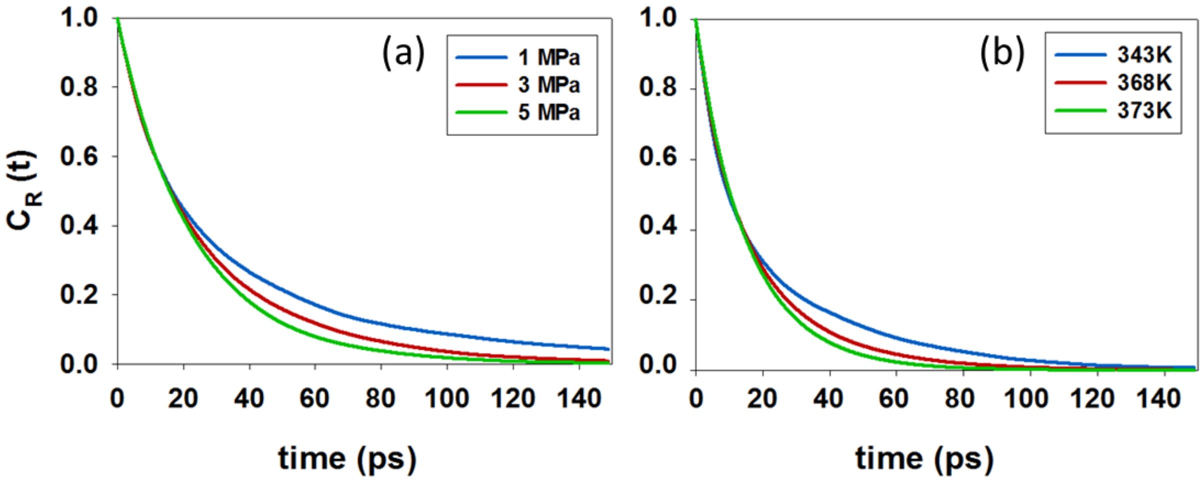

Figure 3-9 Residence autocorrelation function $C_R(t)$, for propane within the first adsorbed layer within the 2.7 nm silica pore as a function of (a) pressure at 368K, and (b) temperature at 3 MPa.

3.5. CONCLUSIONS

Molecular dynamics simulations were employed to study structural and dynamic properties of pure propane in slit-shaped fully protonated silica pores at 343, 368, and 373K. Adsorption isotherms were calculated at varying bulk pressures from 0 to 6 MPa in pores of effective width 0.8 and 2.7 nm. To facilitate comparison with experiments, the results were analyzed in terms of excess adsorption. Despite significant differences between the simulated and experimental systems, reasonable, yet not complete, qualitative agreement was obtained. Some possible reasons have been proposed to explain the discrepancies between simulated and experimental results. Experimental data is complemented by investigating the structure of propane molecules adsorbed in the pores and by quantifying some of their transport properties. The highest in-plane self-diffusion coefficients are obtained at high temperature, because of higher molecular mobility, and low pressure, because no high-energy adsorption sites are available for propane within the pores considered in our simulations. The results presented here will be useful to advance applications in the oil and gas, chemical, environmental, and automotive industries.

Chapter 4. Confinement of Long Chain Alkane and Carbon Dioxide Mixtures

The material presented in this chapter was published in **2015** in volume *119*, pages 15274-15284 of the *The Journal of Physical Chemistry C* journal (section 4.2) and volume *121*, pages 1-8 of the *Molecular Simulation* journal (section 4.3).

4.1. ABSTRACT

This chapter presents the structural (i.e., density profiles, molecular orientation, and preferential adsorption sites) and dynamic properties (i.e., self-diffusion coefficients, trajectories, and residence times of confined fluids at contact with the solid surface) for mixtures containing long chain alkane (either n-butane or n-octane) and CO_2 confined in silica pores of different morphologies (slit-shaped or trench). Silica is chosen because quartz is an abundant sub-surface material. β-cristobalite was used to compare the new results to those obtained for several fluids under confinement.[25-26, 28] In the first section, investigation on the effect of mixture density and composition on adsorption and diffusion of the confined CO_2/n-butane mixture was carried out. In contrast, the effect of increasing CO_2 loading at constant n-octane loading is studied in the second part of this chapter. Temperatures below, between, and above the critical temperatures of CO_2 and n-butane were considered while a fixed temperature of 300 K was used to study CO_2 and n-octane mixture. MD simulations are chosen in the present investigation for their ability to provide extensive insights regarding effective fluid-solids interactions, structural and dynamic properties of all components of interest.

4.2. N-BUTANE AND CO_2

4.2.1. INTRODUCTION

International attention on curbing anthropogenic CO_2 emissions has recently increased dramatically.[90-92] Among other technologies, CO_2 capture and storage (CCS) is considered one of the most attractive alternatives.[9] Some pilot CCS projects have been initiated. In Sleipner (west Norway) 1 million metric tons of CO_2 have been injected annually, since 1996, into sedimentary basins.[93] Recently, CO_2 has also been injected into basaltic formations, because their high content of Ca, Mg, and Fe suggests the possibility of achieving

CO_2 mineralization.[16-18] CO_2 sequestration combined with enhanced coal bed methane recovery has also been extensively studied,[94-95,96,97] and CO_2 injection is often used in tertiary enhanced oil recovery in depleted petroleum reservoirs.[98] Lately, CO_2 has also been used in fracturing fluids for shale gas stimulation.[99-100] Not only CO_2 can be captured and stored within the shale formation, recent results suggest that in some cases CO_2 can create better fractured networks compared to water.[101] Should CO_2 exhibit higher affinity to the rock formations than hydrocarbons, it could help increase production. Understanding the relation between competitive adsorption and transport of CO_2 and hydrocarbons in rock formations is considered crucial to optimize both CO_2 storage capacity[19] and natural gas production.

Much is known about structure and dynamics of carbon dioxide and methane confined in activated carbons,[11] carbon nanotubes (CNTs),[12] and zeolites.[13-15] The transport of CO_2 through silica has been studied using experiments[102-103] and simulations.[102, 104-105] Experimental and simulation results confirm the preferential adsorption of CO_2 from binary CO_2/CH_4 mixtures. High CO_2 adsorption selectivity was observed in CNTs.[12] An extensive review on CO_2 and methane storage in hybrid porous solids, crystallized porous materials including MOFs, and porous coordination polymers was compiled by Ferey et al.,[106] who summarized structural, spectroscopic, thermodynamics experiments as well as molecular simulation results. Because of the intrinsic limitations of experiments, thermodynamic models, and simulations, holistic approaches inclusive of all such contributions are needed to completely understand complex phenomena such as those just discussed. As opposed to the extensive literature on pure CO_2 and CH_4 and on their binary mixtures, few results are available for mixtures of CO_2 and higher molecular weight hydrocarbons such as butane and octane in microporous confinement.

In **Chapter 3**, extensive MD simulations were conducted to study propane adsorption, structure and diffusion in slit-shaped silica pores at sub-, near-, and super-critical conditions.[107] The results were qualitatively consistent with the experimental adsorption isotherms reported by Gruszkiewicz et al.,[6] and the SANS data reported by Rother et al.[7] In the next section, MD simulations study for the structure and dynamics of CO_2-octane mixtures confined within slit-shaped silica pores will be presented. The results here show structural (i.e., density profiles, molecular orientation, and preferential adsorption sites) and dynamic properties (i.e., self-diffusion coefficients and residence times at contact with the solid surface) for mixtures containing n-butane and CO_2 confined in slit-shaped silica pores. β-cristobalite silica was used to compare the new results to those our group has obtained for several fluids under confinement. This section investigates the effect of mixture density and composition on adsorption and diffusion of the confined fluids. Temperatures below, between, and above the critical temperatures of CO_2 and n-butane are considered. MD simulations are chosen in the present investigation for their ability to provide extensive insights regarding effective fluid-solids interactions, structural and dynamic properties of all components of interest.

4.2.2. SIMULATION METHODOLOGY

Extensive MD simulations for the binary mixtures of CO_2/n-C_4H_{10} confined within slit-shaped silica pores were performed. The pore width is 2 nm and the corresponding simulation box dimensions are 10.48×10.08×5.34 nm^3. In pores as narrow as the one chosen for the present study interfacial interactions are expected to dictate the confined fluid behaviour. Note that transport of fluid through pore throats of this width, and perhaps narrower, is expected to control the permeability in shale rocks.[108] The effective pore volume in our model system was estimated to be approximately 204.83 nm^3. Because of periodic boundary conditions, the systems considered are composed by silica slabs that are infinitely long along the X and Y directions, and separated along the Z direction by the slit-shaped pore.

The experimental critical temperatures of CO_2 and C_4H_{10} are 304.13K and 425.125K, respectively.[24] To investigate the properties of the mixtures as the temperature changes from sub- to super-critical, 3 temperatures were chosen: 290K (below the critical T of both fluids), 343K and 430K (above the critical T of both fluids). Different densities of the confined mixtures (100, 300 and 500 total molecules) and different mixture compositions (CO_2:n-C_4H_{10}=1:9, 5:5 and 9:1) were considered. **Figure 4-1** represents the pore with 250 CO_2 and 250 n-butane molecules.

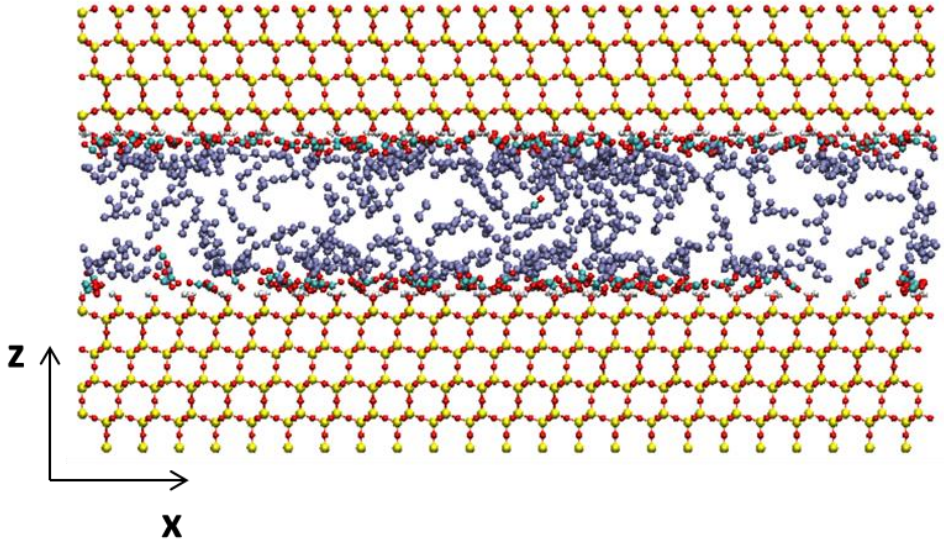

Figure 4-1 Simulation snapshot representing a simulation box containing 250 CO_2 and 250 n-C_4H_{10} molecules in the 2 nm silica pore at 343K. The solid silica slabs are continuous along both X and Y directions. No bulk region exists. Purple spheres are CH_2 and CH_3 groups in n-butane, cyan is C in carbon dioxide, red is O, white is H, and yellow is Si.

As it has been shown in **Chapter 2**, the diffusion of fluid can be described as an activated process using the Arrhenius formalism and plotting $\ln D(0)$ as a function of $1/T$ will yield a straight line whose slope is $\frac{-E_a}{R}$. To estimate the effect of CO_2 on the activation energy of butane diffusion, and in particular the role of electrostatic interactions between CO_2 and the solid substrate on E_a, equation (2.31) is applied to fit results obtained for n-butane (1) at infinite dilution in CO_2 (the system contained 500 CO_2 and 2 C_4H_{10} molecules); (2) at infinite dilution in a model fluid obtained by setting all partial charges of CO_2 to zero (while not changing the CO_2 Lennard-Jones parameters; i.e., pseudo-CO_2); and (3) at vanishing density (only 2 butane molecules with no other fluid present).

MD simulations were conducted for 100 ns of simulation time for all systems investigated. Equilibration was considered achieved after ~50-80 ns, depending on the system loading, when the system temperature, total energy and density profiles fluctuate around constant values (+/- 15%). Data analysis was carried out over the last 10 ns of each simulation. All results were calculated considering the COMs of the fluid molecules.

4.2.3. RESULTS AND DISCUSSIONS

4.2.3.1. Structural Properties

4.2.3.1.1. *Molecular Density Profiles*

Molecular density profiles along the direction perpendicular to the pore surface were calculated for all simulated systems. Representative density profiles for single-component systems of both species at increasing loadings (50, 300 and 500 molecules within the simulated system) at 430K are presented in **Figure 4-2**. The results show that CO_2 adsorbs more closely to the pore walls even at this relatively high temperature compared to butane, presumably because of preferential interactions with the surface groups. Simulation snapshots for the corresponding systems are provided in **Figure 4-2** for visualization purposes.

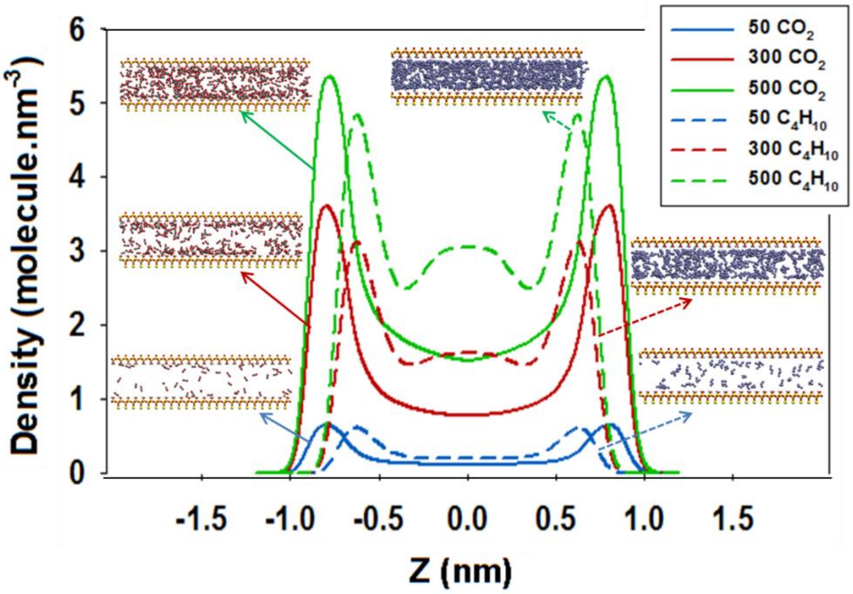

Figure 4-2 Molecular density profiles for carbon dioxide (solid lines) and n-butane (dashed lines) with corresponding simulation snapshot for pure component systems with 50, 300 and 500 molecules at 430K. Z is the direction perpendicular to the pore surface and Z=0 corresponds to the pore center. The color code is the same as that used in **Figure 4-1**. Only 2 inner atomic layers of the pore surfaces are shown for clarity. Note that the results presented in this figure are for single-component systems.

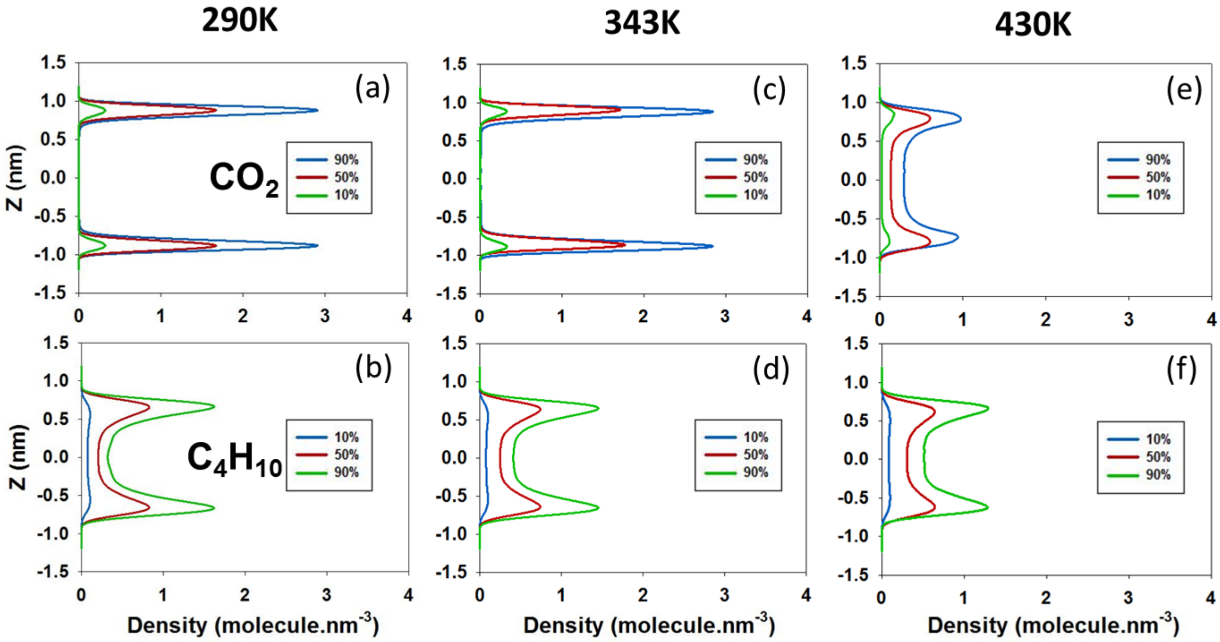

Figure 4-3 Molecular density profiles for carbon dioxide (top panels) and n-butane (bottom panels) in mixture containing a total of 100 molecules at 290, 343, and 430K. Z is the direction perpendicular to the pore surface and Z=0 corresponds to the pore center. Different lines represent results at different compositions. Blue, red and green lines represent mixtures with CO_2:n-C_4H_{10} molecular ratios of 9:1, 5:5 and 1:9, respectively.

Results obtained at different temperatures and mixture compositions are shown in **Figure 4-3**, **4-4** and **4-5** where CO_2 (top panels) and n-C_4H_{10} (bottom panels) profiles are computed separately. **Figure 4-3**, **4-4** and **4-5** are for systems with a total of 100, 300 and 500 fluid molecules, respectively, at different CO_2 versus n-C_4H_{10} composition.

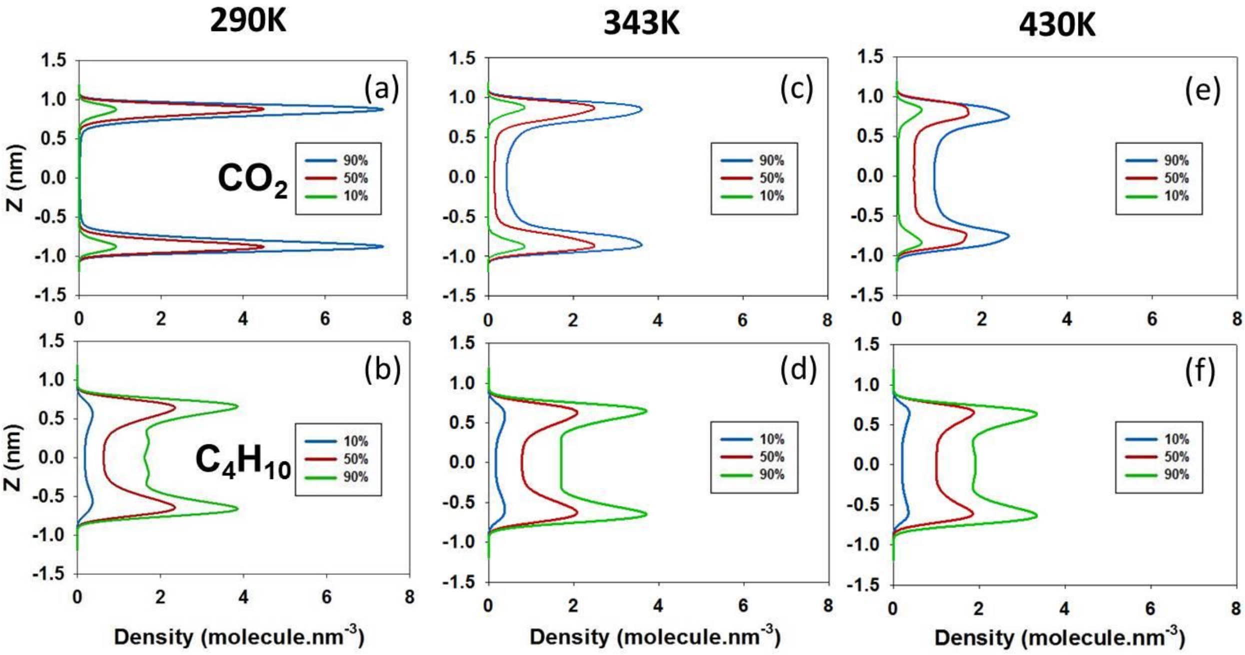

Figure 4-4 Same as **Figure 4-3** for mixture containing a total of 300 molecules.

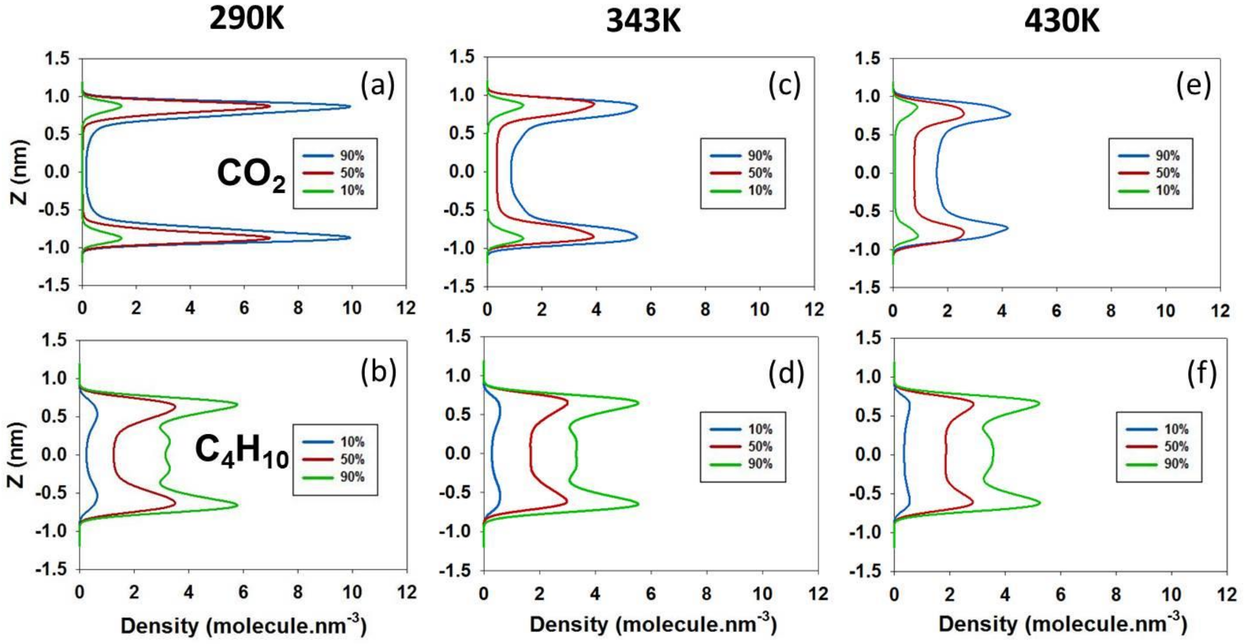

Figure 4-5 Same as Figure 4-3 for mixture containing a total of 500 molecules.

The results in each pair of *vertical* panels in **Figure 4-3, 4-4** and **4-5** were obtained at constant temperature and density, but different compositions. The molecular ratios CO_2:n-C_4H_{10} investigated were 9:1, 5:5 and 1:9 (blue, red and green lines, respectively). The molecular density profiles are shown as a function of the distance from the pore center (Z=0). For each curve, there are two distinct peaks (symmetric with respect to the pore center) that are localized near the pore surface. These are due to the adsorption of either CO_2 or butane on the pore walls. At high densities (i.e., 500 molecules) multiple peaks are observed in the density profiles obtained for butane, especially when the mixture composition is 90% C_4H_{10}, at the lowest temperature considered, suggesting the formation of a multi-layered structure. On the contrary, no CO_2 multilayer was observed at any condition considered. The results also show that the location of CO_2 peaks does not depend on T, and that this location is always close to the pore surfaces. The fact that the CO_2 density peaks are always closer to the pore walls than the butane density peaks indicates preferential CO_2 adsorption on the protonated silica surfaces, presumably because of the polar interactions between CO_2 and the surface –OH groups. The CO_2 peaks are higher and narrower at lower T, because of reduced thermal motion.[109] Note that while at low CO_2 concentration no CO_2 is found, statistically, near the pore center, butane molecules are always found near the pore center even at the lower butane concentrations considered here, suggesting that CO_2-pore attractions are stronger than butane-pore ones. As T and concentration rise, CO_2 can also be found near the pore center. The strong association between CO_2 and the pore surface revealed by the presented simulations is qualitatively consistent with recent experimental results reported by Rother et al. for CO_2 in porous silica aerogels.[110] The results discussed so far are qualitatively consistent with those obtained for CO_2-octane systems confined in a silica pore similar to the one considered here (see section **4.3**), in which case it was found that adding small amounts of CO_2 could displace the location of the octane density peaks further away from the surface compared to the results obtained for the pure hydrocarbon.

4.2.3.1.2. *Planar Density Distributions: Localization of Preferential Adsorption Sites*

To document the molecular structure of the adsorbed CO_2 layer and to identify the preferential adsorption sites on the silica substrates, in-plane density distributions are calculated. The calculations were performed for the oxygen atoms of those CO_2 molecules found within the first adsorption layers (see **Figure 4-3, 4-4** and **4-5**) parallel to the pore surface and of 5 Å in thickness. Similar calculations were performed for the COM of those n-butane molecules found within the first adsorption layer of thickness 3.8 Å as identified by the density profiles shown in **Figure 4-3, 4-4** and **4-5**. These types of calculations provide greater detail on the structure of the first hydration layer and/or of the first solvation layer on various substrates.[27, 29] Panels (b) and (c) of **Figure 4-6**, respectively, present the results obtained in this work. Both data sets are obtained for systems in which either CO_2 (panel b) or butane (panel c) are the main component within the fluid system. The results show that it is highly probable to find the oxygen atoms of adsorbed CO_2 molecules near the surface –OH groups of the solid silica substrate. This is expected, as CO_2 molecules can form hydrogen bonds with the –OH groups. According to the newest definition by IUPAC, a hydrogen bond is "an attractive interaction between a hydrogen atom from a molecule or a molecular fragment X–H in which X is more electronegative than H, and an atom or a group of atoms in the same or a different molecule, in which there is evidence of bond formation".[111] Note that evidence for a hydrogen bond between the oxygen atoms in CO_2 and water molecules has been provided by Sato et al. using a combination of ab initio molecular orbital theory and statistical mechanics theory of molecular liquids, which explains why CO_2 is more soluble in water compared to CO.[112] The results obtained for butane show that these molecules accumulate along the hexagonal edges of the atomic structure of the solid substrate, suggesting that non-specific dispersive interactions are responsible for the formation of the first adsorbed layer of butane near the flat solid surface reported in the density profiles discussed in **Figure 4-2** to **4-5** above. The planar density profiles for butane in **Figure 4-6** are a little smeared because the COM of the molecule is considered rather than the individual atoms.

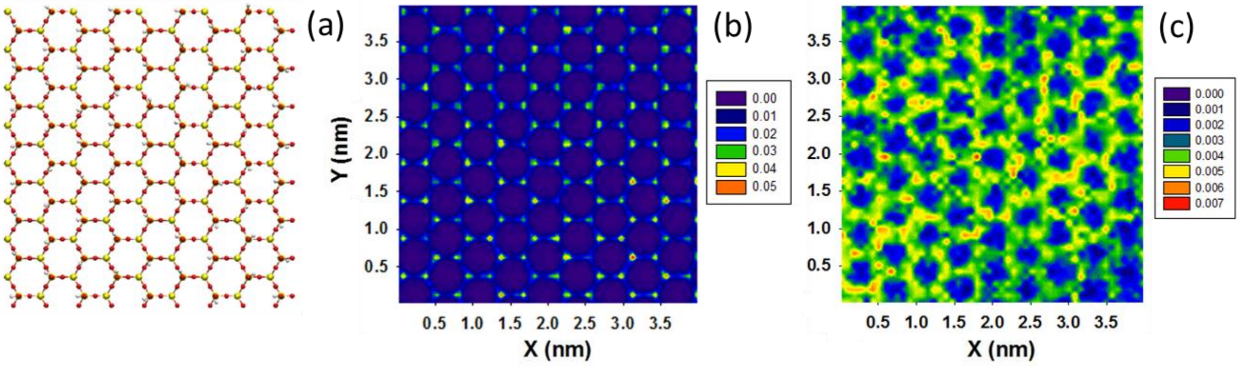

Figure 4-6 (a) OH-terminated silica surfaces. Only the upper 2 atomic layers are shown for clarity. (b) Planar density distribution of O atoms of CO_2 molecules within the first adsorption layer when 500 molecules, 90% CO_2, are simulated at 290K. (c) Planar density distribution of the COM of n-butane within the first adsorption layer for a system composed of 500 molecules (90% butane) at 290K. Densities are expressed in number of atoms.nm^{-3} or molecules.nm^{-3}. Note that the densities in panels (b) and (c) are of different orders of magnitude.

4.2.3.1.3. *Orientation of Adsorbed CO_2*

Figure 4-7 reports the preferential orientation of adsorbed carbon dioxide molecules. The molecules considered are those within the first adsorbed layer, as discussed in the prior section. The probability distribution of the angle θ formed between the CO_2 backbone and the surface normal is quantified. When θ is 0° or 180°, the CO_2 molecule is perpendicular to the surface; when θ is 90°, CO_2 lays parallel to the surface. See **Figure 4-7** panel (a) for an illustration. The results obtained for the system comprised of 150 CO_2 and 150 n-butane molecules at 343K is shown in panel (b). The results show that CO_2 molecules within the first adsorbed layer preferentially orient at an angle θ of ~80°. While the preferential orientation angle of ~80° with the surface normal is observed in all systems considered, the local minimum in the orientation observed at ~90° is less pronounced when the simulation temperature decreases, and when the CO_2 loading decreases. As the substrate –OH and CO_2 molecules can form hydrogen bonds, the most energetically favorable configuration is expected to be the one where –OH and O–C–O lay on a straight line. Because the silanol Si–O–H group has an angle of ~109.5°, θ was thought to be ~70.5°. The fact that θ is ~9.5° larger indicates that each adsorbed CO_2 molecule tends to interact simultaneously with more than 1 surface –OH at a time. This becomes slightly more pronounced when T and CO_2 loading are lowered. This result is consistent with results obtained from the simulation of n-octane–CO_2 mixtures confined in silica pores (see section **4.3**). In that contribution, investigation is made for systems at increasing CO_2 loadings. In conclusion, on average, when the amount of CO_2 present is sufficient to saturate the pore surface considered one CO_2 molecule occupies two surface –OH groups.

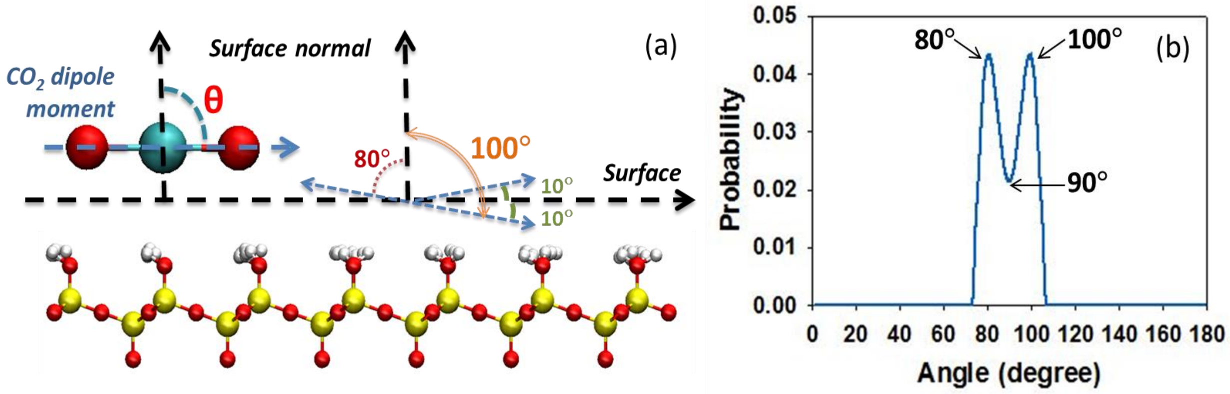

Figure 4-7 (a) Schematic for the orientation of one adsorbed carbon dioxide molecule. The color scheme for the solid substrate and CO_2 model is the same as that of Figure 1; (b) Probability density distribution for the angle θ for CO_2 molecules adsorbed within the first layer adsorbed of 5 Å thickness in silica pore. The results are obtained for the system composed of 150 CO_2 and 150 n-butane at 343K.

4.2.3.2. Dynamical Properties

4.2.3.2.1. *Diffusivity – Pure substances*

Single-component self-diffusion coefficients of (1) CO_2 at 290, 343 and 430K and (2) n-butane at 430K are calculated and presented in **Figure 4-8**. Results obtained for pure CO_2 at different temperatures show a maximum in D_s as loading increases from a near-zero loading. The maximum is narrower, steeper and shifted to lower loadings as T increases. CO_2 self-diffusion results match the type IV behavior as classified by Karger and Pfeifer.[113] CO_2 diffusion results are in good qualitative agreement with those reported by Sholl,[114] who represented an adsorbent using a lattice with heterogeneous adsorption sites and fluid species characterized by different adsorption energies (i.e., very strong attractive sites for specie 1 and no energetic preferences for specie 2). Results presented in **Figure 4-8** for CO_2 are consistent with those obtained for the fluid specie that is strongly adsorbed on preferential sites available on the lattice: at low loadings, most particles of this fluid are trapped near the correspondent adsorption sites, and diffusion is dominated by slow hopping events between strong adsorption sites. At moderate loadings, those molecules that are not trapped can diffuse rapidly and the overall diffusivity increases. At high loadings, the diffusion coefficient decreases because of steric hindrance. The results show that at 430K the self-diffusion coefficient of pure CO_2 displays a maximum at intermediate loadings while that of pure C_4H_{10} monotonically decreases with increasing loading (panel b). The results for butane are also consistent with those presented by Sholl,[114] when the fluid is not strongly attracted to lattice sites, in which case the self-diffusion coefficient monotonically decreases as loading increases. At 430K, D_s of CO_2 is higher than that of C_4H_{10} except at very low loadings. Visualizations of sequences of simulation snapshots suggest that CO_2 diffusion occurs predominantly along the surface, while butane moves across the pore volume, which is in agreement with the density profiles shown above. It is possible that the self-diffusion coefficient of CO_2 is faster than that of butane because the former molecule is smaller and slender than the latter. Babarao and Jiang investigated CO_2 and CH_4 transport across nano-porous materials with pore sizes in the range of ~7–9 Å; their results show that steric hindrance causes a decrease in self-diffusion coefficient as loading increases for both substances.[48]

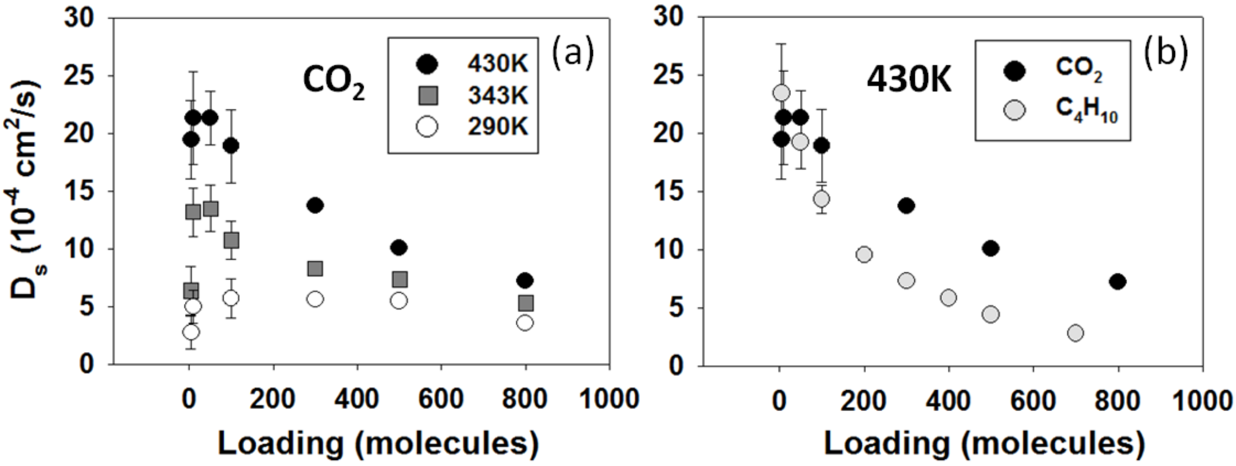

Figure 4-8 Single-component self-diffusion coefficients as a function of loading for (a) CO_2 at different temperatures and (b) CO_2 and C_4H_{10} at 430K. Error bars are estimated as one standard deviation from the average. At high loadings, symbols are larger than error bars.

4.2.3.2.2. *Diffusivity – Mixtures*

Calculated CO_2 and n-C_4H_{10} self-diffusion coefficients at different mixture densities and compositions are presented in **Table 4.1** and **4.2**. In general, the mobility of both fluids increases with increasing *T* and decreasing mixture density (lower total number of molecules) because higher *T* increases the kinetic energy of the molecules, while lower density reduces molecular collisions and steric hindrance. When binary mixtures are considered, the results show that D_s for CO_2 increases as its concentration increases, at a given total pore loading, with maximum D_s observed for 100% CO_2. A similar observation was reported by Wang et al.[86] in their experimental study for the diffusion of various alkanes in microporous BPL activated carbon. These results are explained as follows: at low loadings, adsorbate molecules are strongly adsorbed on high-energy adsorption sites, which results in low diffusion coefficients. As the amount adsorbed increases, the high-energy adsorption sites are saturated, and the diffusion statistically increases because adsorbate molecules have more mobility. Note that while CO_2 is preferentially adsorbed on the surface –OH groups in this work model adsorbent, alkanes are strongly adsorbed on activated carbons. Observations similar to those reported herein were obtained also for our systems comprising of n-octane and CO_2 (see section **4.3**), but not for systems comprised of only propane, because in the latter case no high-energy adsorption sites are available for propane on the fully protonated silica surfaces.[107] The increased mobility of CO_2 upon increasing its concentration at constant pore loading is consistent with results reported by Snurr and Karger[115] for methane and tetraflouromethane mixtures in silicalite. By performing both MD simulations and NMR experiments, at the total loading for 12 molecules per unit cell, the diffusivities of both fluids were found to increase with increasing amount of CH_4, which is the lighter and more mobile component. At constant loading (number of molecules), the results show that the self-diffusion coefficient for butane decreases as the amount of CO_2 decreases. This could be due to steric hindrance (butane is larger than CO_2), and to changes in the activation energy of butane diffusion due to CO_2 (discussed below). The decrease of the activation energy due to CO_2, is consistent with observations reported by Vidoni.[116] This latter study experimentally measured the competitive diffusion of CH_4 with either He or CO_2 in DD3R crystals using the zero length column method. The results showed reduced activation energy for diffusion of CH_4-CO_2 compared to CH_4-He due to the competitive adsorption of carbon dioxide on the pore surfaces. Similarly, CO_2 has been found to decrease the activation energy of ethane in controlled pore glass using gravimetric adsorption and quasi-elastic neutron scattering (QENS) measurements.[117]

Table 4.1 In-plane self-diffusion coefficients estimated for CO_2

CO_2 Calculated Diffusion Coefficient (10^{-4} cm^2/s)				
Total number of molecules	Composition (CO_2:C_4H_{10})	290K	343K	430K
100	Pure CO_2	*5.7 ± 1*	*11 ± 2*	*19 ± 3*
	9:1	3.5 ± 1	8.5 ± 1	15 ± 2
	5:5	1.5 ± 0.3	3.7 ± 2	12 ± 3
	1:9	1.1 ± 0.2	2.5 ± 1	6.6 ± 1
	Bulk CO_2	43 ± 6 (vapor, 1.68 MPa)	57 ± 6 (vapor, 2.06 MPa)	65 ± 7.5 (vapor, 2.7 MPa)
300	Pure CO_2	*5.6 ± 2*	*8.3 ± 0.2*	*14 ± 0.1*
	9:1	3.5 ± 0.3	5.8 ± 0.4	12 ± 0.4
	5:5	1.3 ± 0	2.8 ± 0.4	7.4 ± 1
	1:9	1.2 ± 0.2	2.7 ± 0.2	4.8 ± 2
	Bulk CO_2	16 ± 3.7 (vapor, 4.04 MPa)	18.6 ± 5 (vapor, 5.39 MPa)	22 ± 1.6 (s.c.,[α] 7.46 MPa)
500	Pure CO_2	*5.5 ± 2*	*7.4 ± 0.3*	*10 ± 0.3*
	9:1	3.3 ± 0.3	5 ± 0.4	8.7 ± 1
	5:5	1.4 ± 0.1	2.5 ± 0.4	5.5 ± 2
	1:9	0.7 ± 0	2 ± 0.1	4.1 ± 1
	Bulk CO_2	9 ± 0.7 (vapor, 5.30 MPa)	10 ± 1.6 (s.c.,[α] 7.88 MPa)	12.6 ± 1 (s.c.,[α] 11.74 MPa)

[α] super critical

Table 4.2 In-plane self-diffusion coefficients estimated for C_4H_{10}

C_4H_{10} Calculated Diffusion Coefficient (10^{-4} cm^2/s)				
Total number of molecules	Composition (CO_2:C_4H_{10})	290K	343K	430K
100	9:1	13 ± 2	21 ± 4.3	22 ± 0.7
	5:5	9.4 ± 1	16 ± 2	18 ± 2
	1:9	7.9 ± 0.5	10 ± 1	13 ± 1
	Pure butane	*6.9 ± 0.6*	*9.8 ± 0.7*	*13 ± 1*
	Bulk butane	14 ± 3 (VLE,$^{\alpha}$ 0.19 MPa)	17.5 ± 5 (VLE,$^{\alpha}$ 0.8 MPa)	26.4 ± 6 (vapor, 2.16 MPa)
300	9:1	10 ± 0.5	14 ± 1.5	14 ± 0.6
	5:5	5.9 ± 1	8.4 ± 0.5	9.4 ± 1
	1:9	4 ± 0.3	6 ± 1.3	8 ± 1
	Pure butane	*3.5 ± 0.2*	*5.3 ± 0.2*	*7.3 ± 0.2*
	Bulk butane	2.5 ± 0.5 (VLE,$^{\alpha}$ 0.19 MPa)	5 ± 1 (VLE,$^{\alpha}$ 0.8 MPa)	7.6 ± 0.6 (s.c.,$^{\beta}$ 3.84 MPa)
500	9:1	6.4 ± 0.4	8.5 ± 0.4	8.6 ± 0.8
	5:5	3.9 ± 0.3	5.3 ± 0.4	7.2 ± 0.5
	1:9	2.5 ± 0.1	3.8 ± 0.1	4.7 ± 0.1
	Pure butane	*2.3 ± 0.1*	*3.5 ± 0*	*4.4 ± 0.1*
	Bulk butane	1.6 ± 0.4 (VLE,$^{\alpha}$ 0.19 MPa)	3 ± 0.5 (VLE,$^{\alpha}$ 0.8 MPa)	4.9 ± 0.3 (s.c.,$^{\beta}$ 4.1 MPa)

$^{\alpha}$ vapor-liquid equilibrium

$^{\beta}$ super critical

For comparison, properties of the corresponding pure, bulk substances at the same T and ρ conditions are also provided in **Table 4.1** and **4.2**. The bulk fluids' equilibrium states and their pressures were taken from the NIST database,[24] while the self-diffusion coefficients were computed via NVT simulations for 5 ns. In all cases, bulk D_s increases with T and decreases with ρ, as expected. All simulated values are in good agreement with various numbers reported via simulations and experiments.[78, 118-119] Note that bulk carbon dioxide always diffuses faster than the confined molecules, and the differences are most pronounced at the lowest ρ and highest T computed. At low density, most confined CO_2 molecules are adsorbed on the pore surfaces, resulting in slow mobility. As the density increases, more confined CO_2 are free to diffuse, making the average D_s increase. In the case of n-butane, the same phenomenon is observed at low density and high temperature. At moderate to high ρ and low T, the bulk butane molecules appear to diffuse slower compared to the pure, confined ones. Possible explanation is as followed. At low pressure, there are more interactions between the fluid-solid compared to fluid-fluid ones. Thus, the bulk butane diffuses faster than those in confinement. At high pressure, it is possible that layering near the surfaces enhances the propane excess entropy,[120] and hence D_s. Recall that $\Delta s^{id} = \Delta s - \Delta s^{ex}$ with the change in ideal entropy Δs^{id} quantifies how density profile modifies the ideal gas entropy and the excess quantity Δs^{ex} measures the entropic change as a function of interparticle interaction. The formation of layering at the fluid-solid interfaces decreases both the ideal gas entropy ($\Delta s^{id} < 0$) and system entropy ($\Delta s < 0$). However, these entropic penalties are partially compensated by an increase in s^{ex}.[120] The idea of larger excess entropy leading to larger D_s was proposed by Mittal et al.[88] during their investigation on the relation between self-diffusion coefficient and density for bulk versus confined hard spheres. Similar observation was obtained in **Chapter 3** for pure propane confined in slit silica pore.[107]

To assess the activation energy for C_4H_{10} diffusion in the pores considered here, **Figure 4-9** reports the natural logarithm of C_4H_{10} self-diffusion coefficients at infinite dilution, $lnD(0)$, as a function of the inverse temperature (T=290, 343, 430, 500 and 700K). By fitting equation (2.31) to the data, E_a is extracted. The results shown in **Figure 4-9** are for three systems: two mixtures, each consisting of 2 butane and either 500 CO_2 or 500 pseudo CO_2 molecules, and pure butane at very low loading (empty circles). The simulations for butane at infinite dilution in the two mixtures are conducted to quantify the effect of electrostatic pore-CO_2 interactions on the butane diffusion. The pseudo CO_2 molecules bear no partial charges, although they are described by the Lennard-Jones parameters used to simulate CO_2

molecules. No preferential adsorption of pseudo CO_2 molecules to the solid substrates will occur, while steric effects will be similar for both mixtures. While the self-diffusion coefficients estimated for pure butane are the highest at high temperatures, the calculated E_a for the pure butane at low loadings is 6.5 kJ/mol, while the activation energies for butane at infinite dilution in CO_2 and in the pseudo CO_2 systems are 3.4 and 5.7 kJ/mol, respectively. These results confirm that the electrostatic interactions between CO_2 and the pore surfaces, which cause preferential adsorption due to hydrogen bonds, is responsible for the enhanced hydrocarbon mobility observed in our simulations. While the pseudo CO_2 molecules also lower the activation energy compared to the system of pure butane at low loadings, pore crowding increases steric hindrance.

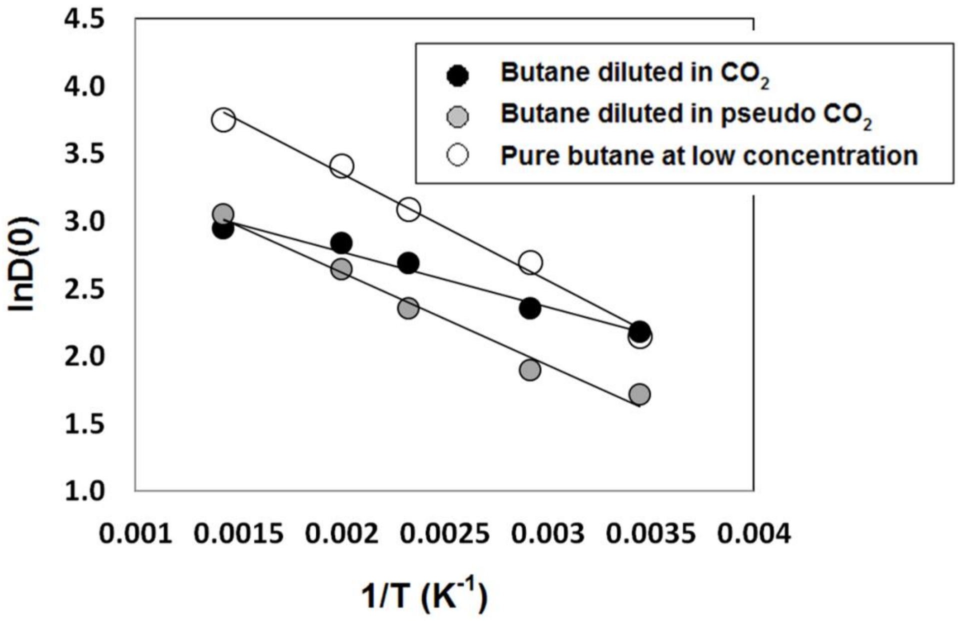

Figure 4-9 Arrhenius plot for the self-diffusion coefficient of n-C_4H_{10} confined in the silica pore at low concentration (empty circles), at infinite dilution in CO_2 molecules (black circles), and at infinite dilution in pseudo CO_2 molecules (gray circles). Symbols are calculated from simulations. Lines are the Arrhenius fits to the simulation data.

4.2.3.2.3. *Residence Time near Pore Surfaces*

The residence autocorrelation functions, $C_R(t)$, were computed to quantify how long CO_2 and butane molecules remain in contact with the silica surfaces. The algorithm is described in **Chapter 2**. The COMs for both CO_2 and butane were considered to identify the position of one molecule. Only those molecules within the first adsorbed layers were considered. The faster C_R decays from 1 to 0, the faster the molecules leave the adsorbed layer. In **Figure 4-10** panel (a) the results obtained for CO_2 are reported at different CO_2:C_4H_{10} molar ratios when a total of 100 molecules was present within the pore and T=290K. The results show that the higher mole fraction of CO_2, the shorter it remains in the adsorbed layer, possibly due to faster exchanges between the adsorbed molecules and those near the pore center. At the lowest temperature and lowest concentration of CO_2 investigated (290K, 10 CO_2 molecules), C_R(t) plateaus after 300 ps, suggesting that some of the adsorbed CO_2 molecules do not desorb within the simulation timeframe. The correspondent results obtained for butane are shown in **Figure 4-10** panel (b). In this case all the curves overlap for all mixture compositions, suggesting that butane molecules exchange between adsorbed and not-adsorbed states with the same frequency, irrespective of the amount of CO_2 present. This is probably due to the lack of strong attractions between butane and the pore surface. These results suggest that the decrease in activation energy for the n-butane diffusion is not related to the residence time of butane near the adsorbing surface. To support this observation it is worth pointing out that the density profiles obtained for n-butane in the direction perpendicular to the pore surface (**Figure 4-2** to **4-6**) always show peaks at the same distances from the surface, irrespective of the amount of CO_2 present within the system.

In **Figure 4-11**, the residence autocorrelation functions of CO_2 molecules are reported as a function of the total loading (top panels) and temperature (bottom panels) for *equimolar* binary mixtures. Because high temperature favors thermal motion and increased occurrence of fluid collisions that push the adsorbed molecules away from the interface, the residence autocorrelation function decreases faster with increasing temperature and/or density. At 430K, above the critical temperatures for both substances in the mixture, C_R(t) curves overlap for all mixture compositions. The overlapping C_R(t) results at 290K and 343K in panel (a) in **Figure 4-11** and the similarity of CO_2 density profiles in panel (a) and (c) of **Figure 4-3** suggest that at relatively low temperature and low fluids density, T and concentration have negligible effects on the adsorption of CO_2 on the pore wall, conditions at which pore-fluid interactions play the dominant role.

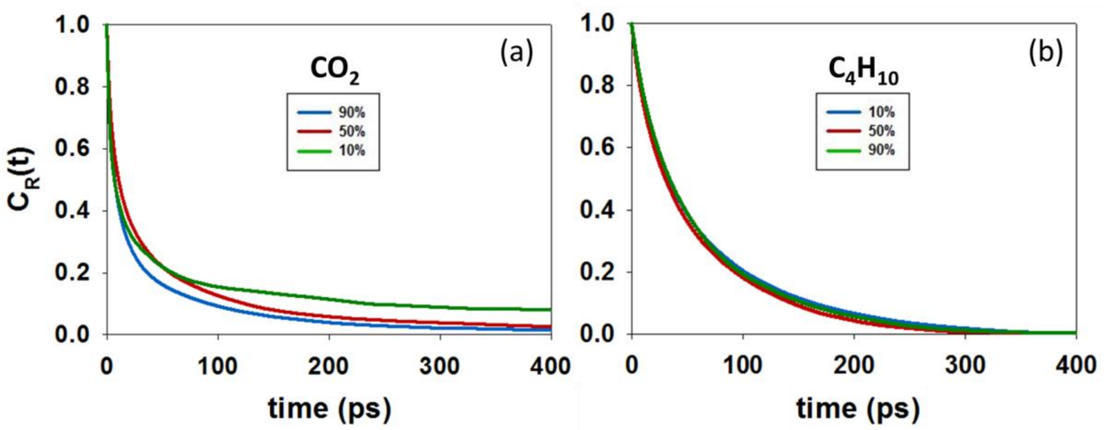

Figure 4-10 Representative residence autocorrelation functions, C_R(t), for (a) CO_2 and (b) n-butane within the first adsorbed layers on the silica pore as a function of CO_2:C_4H_{10} molar ratio. Results are shown for the simulations conducted at 290K with 100 total molecules.

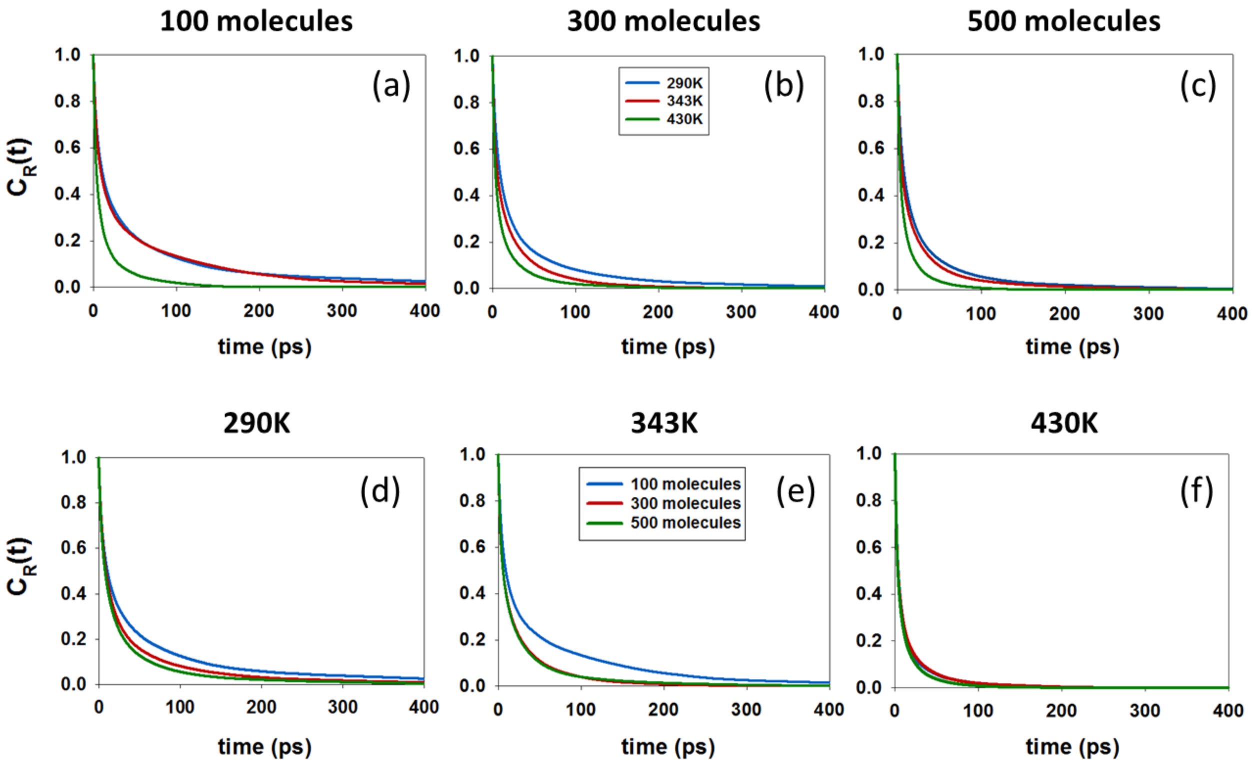

Figure 4-11 Residence autocorrelation functions, C_R(t), for CO_2 within the first adsorbed layer as a function of the total number of molecules in mixture (top panels) and of temperature (bottom panels). In all cases the CO_2:C_4H_{10} molar ratio is 1:1.

The correlations times, τ, are equal to the decay constants obtained by fitting the C_R(t) curves with different exponential decays functions. For butane, each RCF curve can be fitted with a single exponential decays function, representing a single motion mechanism. On the other hand, CO_2 decay faster at initial times τ_1 (i.e., ballistic diffusion) and then becomes much slower at higher time scale (i.e., Brownian diffusion), τ_2. Therefore, RCFs for CO_2 are best fit with a sum of two exponential decays functions. The values obtained for various τ of different system loading at 430K (**Figure 4-10**) are shown in **Table 4.3**.

Table 4.3 Correlations times of CO_2 and C_4H_{10} at different system loading at 430K

Calculated Correlations Times (ps)			
Composition (CO_2:C_4H_{10})	τ_1-carbon dioxide	τ_2-carbon dioxide	τ-n-butane
9:1	0.010	0.125	0.014
5:5	0.008	0.086	0.015
1:9	0.003	0.095	0.016

4.2.4. CONCLUSIONS

Detailed molecular dynamics simulations were performed for systems consisting of pure carbon dioxide, pure n-butane, and their mixtures confined in fully protonated slit-shaped silica nanopores of width 2 nm. A range of temperature (from sub- to super-critical), mixture densities and components ratios was considered. The results show that CO_2 tends to interact with more than one –OH group on the substrate and that it preferentially adsorbs on the pore surface. CO_2 self-diffusion coefficients depend on pore loadings following the type IV behavior in the classification proposed by Karger and Pfeifer.[113] This is a consequence of the existence of high-energy adsorption sites (the surface –OH groups) that can strongly attract the CO_2. The self-diffusion coefficient of pure butane decreases as loading increases as a result of steric hindrance (type I behavior in the classification of Karger and Pfeifer). When mixtures are considered, at the same temperature and total molecular loading, carbon dioxide enhances the self-diffusion coefficient of n-butane by decreasing its diffusion activation energy. The results are corroborated by analysis of the average residence time of the various molecules at contact with the pore surfaces, density profiles in the direction perpendicular to the solid substrate, and parallel to the solid surface. The results can be useful for designing separation devices, and perhaps planning CO_2 capture and storage strategies while optimizing natural gas production.

4.3. N-OCTANE AND CO_2

4.3.1. INTRODUCTION

In the previous section, MD simulations were performed to study the structure and dynamics of CO_2-butane mixtures confined within slit-shaped silica pores.[121] Preferential adsorption of carbon dioxide near the –OH groups on the surface was observed, where the adsorbed CO_2 molecules tend to interact simultaneously with more than one –OH group. Analysis of the simulation results suggests that the preferential CO_2 adsorption to the pore walls weakens the adsorption of n-butane, lowers the activation energy for n-butane diffusivity, and consequently enhances n-butane mobility. Building on these foundations and as an effort to complete our understanding about the system, in this section, investigation on the effect of increasing CO_2 loading and the pore morphology to the mobility of all confined species was made.

In the next section, detailed information about the simulation models and methodology is provided. Next, results are presented and analyzed. Lastly, the conclusions are summarized.

4.3.2. SIMULATION METHODOLOGY

Extensive MD simulations for binary mixtures of CO_2/n-C_8H_{18} confined within slit-shaped silica pores β–cristobalite (1 1 1), whose surface non-bridging oxygen atoms were fully protonated. Approximately, 1 n-octane molecule is 12.8 Å in length and 1 carbon dioxide is 5.4 Å. A slit-shaped pore of width slightly larger than these dimensions were chosen to be simulated, which is 1.9 nm (determined by the distance between the planes determined by the oxygen atoms of the hydroxyl groups across the pore volume), so that the results will differ substantially compared to those attainable in bulk systems because of surface effects. The simulation box was of size 10.48×10.08×5.19 nm^3. The effective pore volume was estimated in ~200.15 nm^3.[107, 122] Periodic boundary conditions were applied in all directions. Because of periodic boundary conditions, the systems considered are composed by silica slabs that are infinitely long along the X and Y directions, and separated along the Z direction by the slit-shaped pore.

The diffusivity of the fluids within the pore is considered as a 2-dimensional translation along the X and Y directions, because the movement along the Z direction is constrained by the confining pore surfaces. Planar self-diffusion coefficient D_s was computed by calculating the MSD. To investigate the effect of CO_2 increasing loading on the mobility of different confined fluids, a total of 7 different systems were simulated whose details can be found in **Table 4.4**. As the molecular density increases, the pressure in the pore is also expected to increase. No attempt was made to compute the pressure representative of the various systems. No bulk was present. All simulations were conducted at 300K, near the critical temperature for CO_2. A schematic representation of a simulated system with 448 carbon dioxide and 282 octane is shown in **Figure 4-12**.

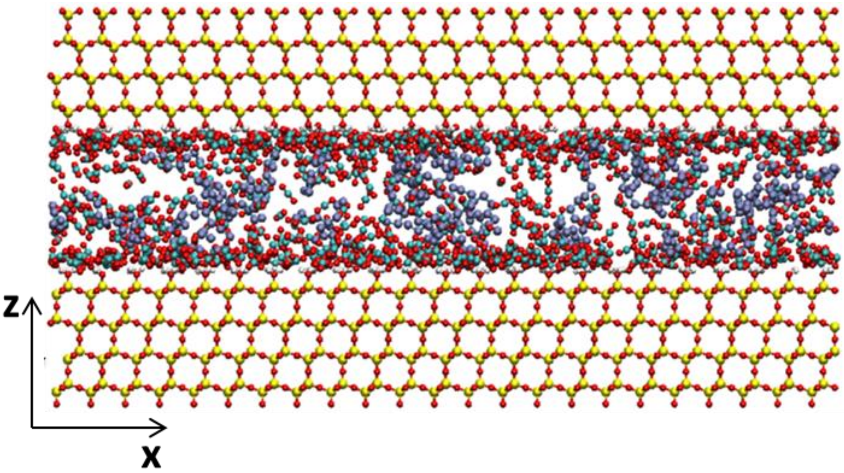

Figure 4-12 Schematic representation of a simulated system. The solid silica slabs are continuous along both X and Y directions, and separated along Z direction. No bulk region exists. The color code is the same as that used in **Figure 4-1**.

Table 4.4 In-plane self-diffusion coefficients calculated for n-octane and CO_2 at 300K within the silica pore of width 1.9 nm considered in this study

Calculated Diffusion Coefficient (10^{-9} m^2/s)			
N-Octane Molecules	Carbon Dioxide Molecules	$D_{\text{s-n-octane}}$	$D_{\text{s-carbon dioxide}}$
282	–	5.7 ± 0.2	–
	225	10 ± 1	1.4 ± 0.5
	448	11.5 ± 0.5	2.7 ± 0.5
	675	11 ± 1	3.8 ± 0.5
	900	10 ± 0.5	5.2 ± 0.6
	1100	7 ± 0.5	5.8 ± 0.4
400	–	4.5 ± 0.8	–

To investigate the effect of the pore morphology to the confined species, an additional simulation was conducted in which the morphology of the pore was modified by inserting two step edges (hence creating a structured pore with a trench on its surface), shown in **Figure 4-13**, while the total pore volume was kept approximately constant at ~200.15 nm^3. The resultant pore is referred to as structured in the remainder of the text. The number of surface –OH groups and their surface densities are the same in the two pore models (pristine and structured). The fluid simulated was composed of 282 n-octane and 900 CO_2 molecules.

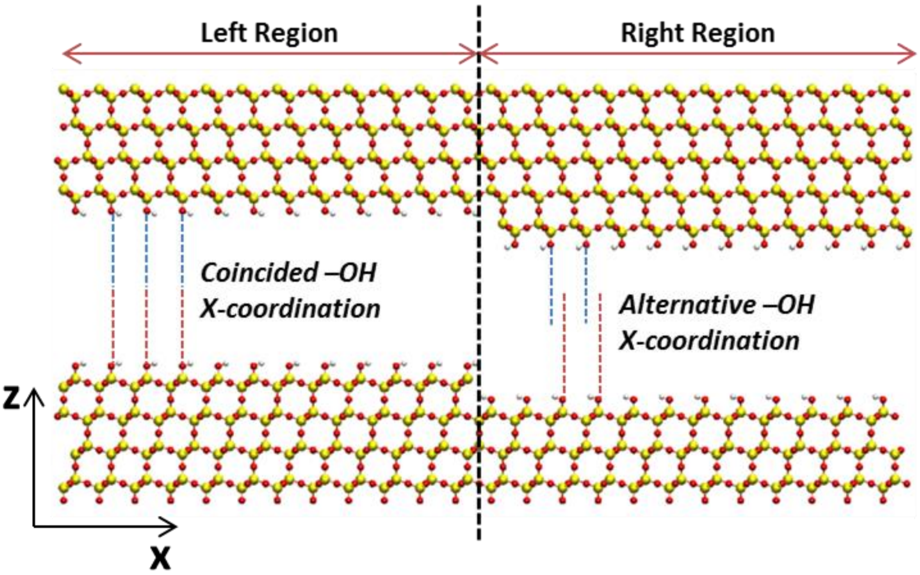

Figure 4-13 Snapshot representing the structured pore with two step-edges yielding a wide trench (when PBC are considered). The color scheme for the solid substrate is the same as that of **Figure 4-1**.

MD Simulations were conducted for 100 ns of simulation time for all systems investigated. The simulation time for each system was in the range 40–150 ns, depending on loading. Data analysis was carried out over the last 10 ns of each simulation. All results were calculated considering the COM of the fluid molecules.

4.3.3. RESULTS AND DISCUSSION

4.3.3.1. Effect of Increasing CO_2 Loading on

4.3.3.1.1. *Molecular Density Profiles*

The density profiles in the direction perpendicular to the pore surface are shown in **Figure 4-14**. For every curve, there are two distinct peaks with equal heights (symmetric with respect to the pore centre). Panel (a) shows n-octane atomic density profiles in all simulated systems.

The results indicate that the locations of the peaks are shifted closer to the pore centre as the number of CO_2 increases. For pure n-octane there are multiple peaks, which suggest the presence of multiple layers of fluid within the pore. Panels (b)–(f) show the density profiles of both fluids. CO_2 shows density peaks closer to the pore walls compared to n-octane, indicating stronger silica surface–CO_2 attractions. Visualization of the simulation snapshot in panel (g) confirms the strong association between CO_2 molecules and the –OH groups on the surfaces. This is expected, as CO_2 molecules can form hydrogen bonds with the –OH groups.[111-112] Note that as its concentration rises, CO_2 can also be found near the pore centre, contradictory with the results obtained on butane and CO_2 mixture. However, since the total loadings are higher in this study, such observation is within expectation. The strong association between CO_2 and the pore surface is consistent with recent results reported by Rother et al. for CO_2 in porous silica aerogel.[110]

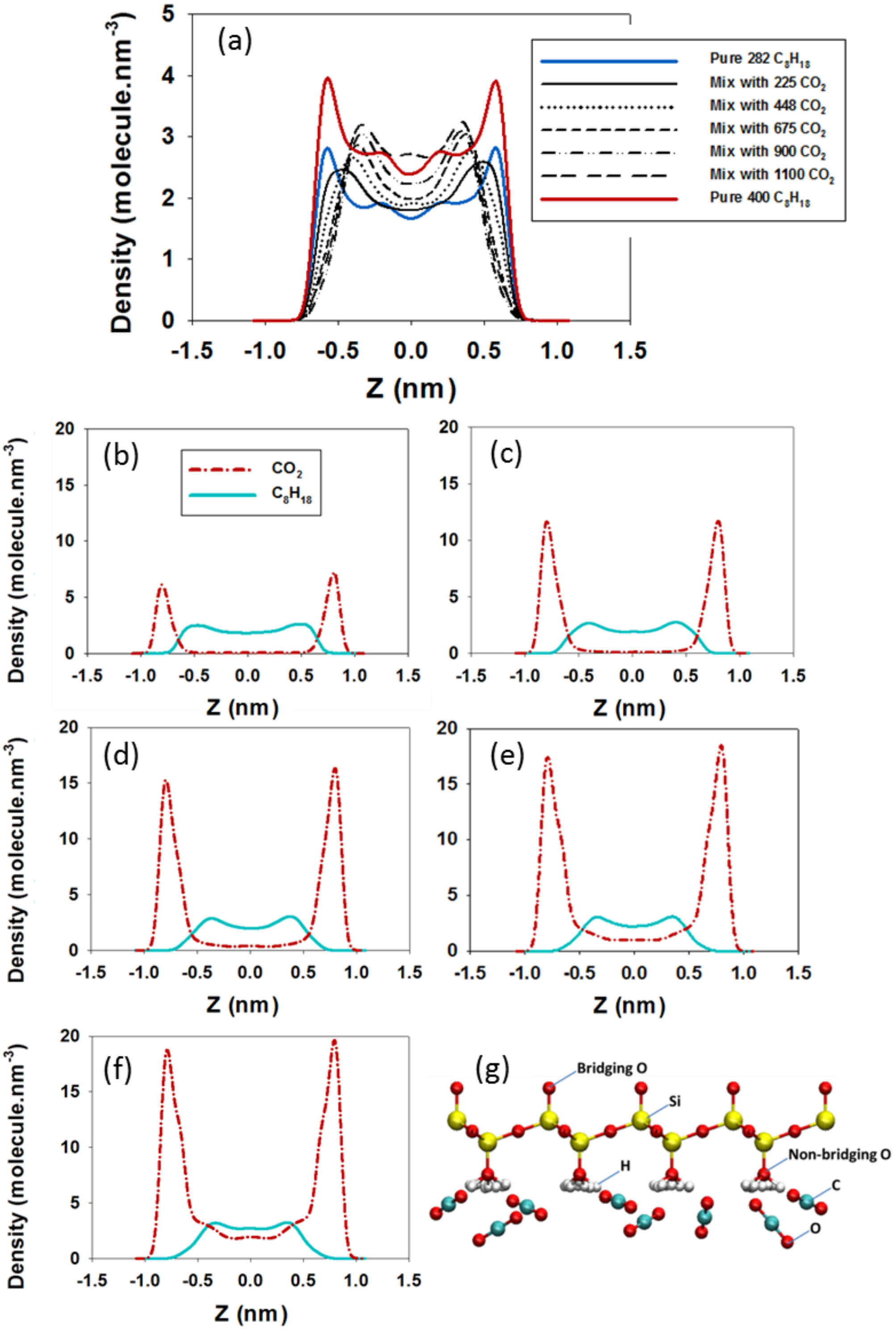

Figure 4-14 (a) N-octane atomic density profiles in all simulated systems; (b), (c), (d), (e) and (f) are the atomic density profiles obtained for systems composed of 282 n-octane and 225, 448, 675, 900 or 1100 CO_2 molecules at 300K, respectively. Z is measured along the direction perpendicular to the pore surface, with Z=0 corresponding to the pore centre; (g) Simulation snapshot for selected CO_2 molecules at the interface. Only a few atomic surface silica and hydroxyl groups are shown for clarity.

4.3.3.1.2. *Orientation of Adsorbed N-octane*

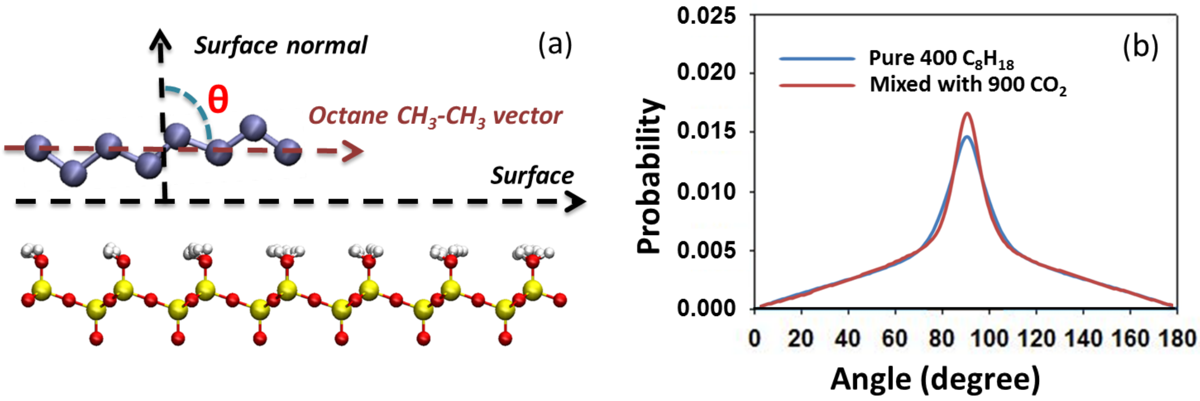

Figure 4-15 (a) Schematic for the orientation of one adsorbed carbon dioxide molecule. The color scheme for the solid substrate and n-octane model is the same as that of **Figure 4-1**; (b) Probability density distribution for the angle θ for n-octane molecules adsorbed within the first layer adsorbed silica pore in the systems composed of 400 pure n-octane (blue line) and of 900 CO_2 and 282 n-octane (red line).

Figure 4-15 reports the preferential orientation of adsorbed n-octane molecules. The molecules considered are those within the first adsorbed layer as identified by the density profiles shown in **Figure 4-14**. The probability distribution of the angle θ formed between the octane CH_3-CH_3 vector and the surface normal was quantified. When θ is 0° or 180°, the molecule is perpendicular to the surface; when θ is 90°, octane lays parallel to the surface. See **Figure 4-15** panel (a) for an illustration. The results obtained for the systems comprised of 400 pure n-octane (blue line) and of 900 CO_2 and 282 n-octane (red line) are shown in panel (b) of the same figure. Data for other binary mixtures are not shown for brevity. The results show that octane molecules within the first adsorbed layer preferentially orient parallel to the pore surface. This orientation allows maximum diffusion rate of hydrocarbon and its probability is increased with the presence of carbon dioxide and with increasing system pressure, as expected. The same set of calculations was conducted for CO_2 in the previous section. The results show that (1) CO_2 molecules within the first adsorbed layer preferentially orient at an angle θ of ~80° as a result of the hydrogen bonding made with the pore surface, and that (2) each adsorbed CO_2 molecule tends to interact simultaneously with more than 1 surface –OH at a time.

4.3.3.1.3. *Diffusivities*

The results for the self-diffusion coefficients for both CO_2 and n-octane are summarized in **Table 4.4**. In general, a non-monotonic change in n-octane diffusivity as a function of CO_2 loading is observed. At low to medium loadings, n-octane diffusivity increases with CO_2 loading. Based on the density profiles, this increase is associated with the displacement of n-octane from the pore surfaces due to the preferential adsorption of CO_2. These observations are qualitatively consistent with those recently reported for CO_2-butane mixtures confined in a silica pore similar to the one considered here (see section **4.2**). Those results, obtained at different temperatures, showed a clear reduction in the activation energy for hydrocarbon diffusion due to the presence of CO_2. The results presented herein are consistent with experimental data reported by Vidoni,[116] who reported a reduction in the experimentally measured activation energy for CH_4 diffusion in DD3R materials due to the co-adsorption of CO_2. At high CO_2 loadings results in **Table 4.4** show a drop in n-octane self-diffusion coefficient, likely because of pore crowding (i.e., more frequent molecular collisions).

One system consisting of 400 n-octane molecules and no CO_2 was simulated to confirm that n-octane enhanced diffusivity is due to CO_2. Indeed, the results show that the n-octane self-diffusion coefficient decreases as its density increases, confirming that CO_2 is essential for enhancing the diffusion of n-octane within the systems considered here. To further confirm this conclusion, an additional simulation is conducted for which the pore size was reduced by 4.8 Å so that the removed pore volume approximately equals the volume occupied by 1100 CO_2 in the mixture. The reduced pore size was estimated by the shift in distance for octane density profile peaks with and without 1100 CO_2 molecules (see **Figure 4-14** panel (a)). 282 pure n-octane molecules were simulated for 40 ns and the calculated n-octane self-diffusion coefficient was 5.2×10^{-9} m^2/s, which was lower than any values obtained for 282 n-octane in the presence of CO_2 (see **Table 4.4**).

In contrast to the results obtained for n-octane, the results show that the self-diffusion coefficient for CO_2 monotonically increases with its loading. This is qualitatively consistent with experimental data reported by Wang et al.[86] for octane and decane in microporous BPL activated carbons, and it is due to the presence of high-energy adsorption sites. In the systems studied here, CO_2 molecules preferentially adsorb on the surface –OH groups. It was expected that the averaged self-diffusion coefficient for CO_2 remains low until all the available preferential adsorption sites are occupied. While this expectation is met qualitatively, the details vary. Analysis of the simulation snapshots suggests that the pore surfaces are saturated by adsorbed CO_2 when the number of molecules present is between 448 and 675. As the simulation cell contains a total of 960 –OH groups on the 2 pore walls, the results suggest that, on average, one CO_2 molecule adsorbs on 2 –OH groups. The results shown in **Table 4.4** suggest that the diffusivity of CO_2 increases even before the two surfaces are saturated.

By analysing the trajectories of representative CO_2 molecules (shown in **Figure 4-16** below) the mechanism responsible for this observation can be can assessed. When only 225 CO_2 molecules are present (**Figure 4-16** panel (a)), the trajectories show little mobility along the X-Y plane, and rarely the CO_2 molecules desorb from the silica surfaces. The situation begins to differ when 448 molecules are present (**Figure 4-16** panel (b)). Although the CO_2 molecules still do not desorb from the silica surface, a noticeable amount of small density fluctuations are observed near the surface, possibly caused by a competition between different CO_2 molecules to adsorb on the –OH groups. These fluctuations allow the CO_2 molecules to escape the attractive wells near the surface, and the molecular diffusion along the X-Y pane increases. The behaviour just described persists when the number of CO_2 molecules increases to 675 (**Figure 4-16** panel (c)), but exhibits an additional event wherein, occasionally, the CO_2 molecules desorb from one silica surface and travel across the pore to adsorb on the other surface. While the CO_2 molecules are near the pore centre, they can travel far along the X-Y plane, leading to enhanced self-diffusion coefficients. As more CO_2 molecules are present, the likelihood of desorption also increases (**Figure 4-16** panel (d)). Should the density of CO_2 simulated within the pore of **Figure 4-12** be increased beyond the range considered herein, it is expected that its self-diffusion coefficient will reach a maximum and then decrease (due to steric hindrance).

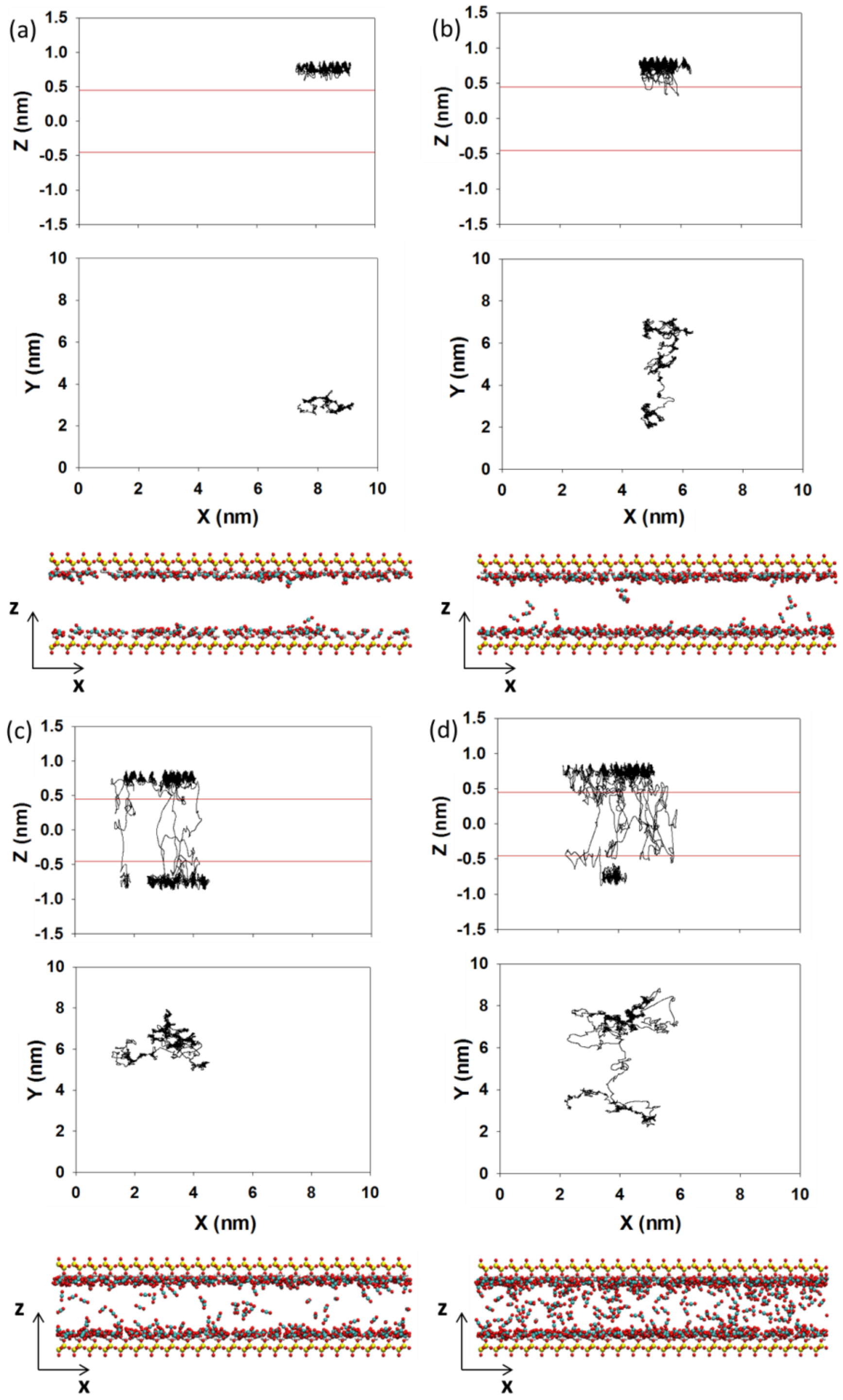

Figure 4-16 Trajectories and simulation snapshots for mixtures composed of 282 n-octane and (a) 225, (b) 448, (c) 675 or (d) 900 CO_2 molecules at 300K. Z is the direction perpendicular to the pore surface, with Z=0 corresponding to the pore centre. The red lines identify the layer of CO_2 adsorbed on the pore surfaces (they correspond to the minima in the CO_2 density profiles in **Figure 4-14**). The black lines reproduce the trajectories of one CO_2 molecule in each system for 1 ns. All simulation snapshots display CO_2 molecules (octane molecules are not shown for clarity) confined within the silica pore (only the pore surface is shown for clarity). The color scheme for the solid substrate and n-octane model is the same as that of **Figure 4-1**.

4.3.3.2. Effect of Pore Morphology

Figure 4-17, panels (a) and (b), shows the simulation snapshots representing the two pore models with the confined 900 CO_2 molecules at 300K (n-octane is not shown for clarity). Panels (c) and (d) of the same figure show the corresponding CO_2 density profiles along the X-direction. While CO_2 in the pore with flat surfaces (pristine pore) displays a rather uniform molecular distribution along the pore length (**Figure 4-17** panel (c)), it distributes unevenly on the structured pore surface, with somewhat higher molecular density near the steps (**Figure 4-17** panel (d)). It is worth mentioning that CO_2 distributions for the left and right halves of the structured pore are different due to the difference in the –OH groups distribution on the two pore surfaces facing across the pore volume (see **Figure 4-13**). Explicitly, in the left half of the pore, the –OH groups of the top and bottom surfaces are aligned along the X coordinate, while in the right half of the pore this does not occur.

The calculated self-diffusion coefficients obtained during the 80 ns simulations within the structured pore were 6.6×10^{-9} and 4.8×10^{-9} m^2/s for n-octane and CO_2, respectively. These results show that n-octane molecules diffuse faster in this structured pore in the presence of CO_2 than when they are pure in the pristine slit-shaped pore. However, the results also show that CO_2 is not as effective in enhancing n-octane mobility as it is in the pristine slit-shaped pore. In fact, the self-diffusion coefficient for n-octane in a fluid mixture of the same composition decreases by about 35% due to the change in pore morphology. The self-diffusion coefficient obtained for CO_2 slightly decreases compared to data obtained in the pristine pore due to the change in pore geometry, which is due to a slight increase in the pore surface area (which is larger on the structured pore by ~5%), and perhaps due to CO_2 accumulation near the surface edges.

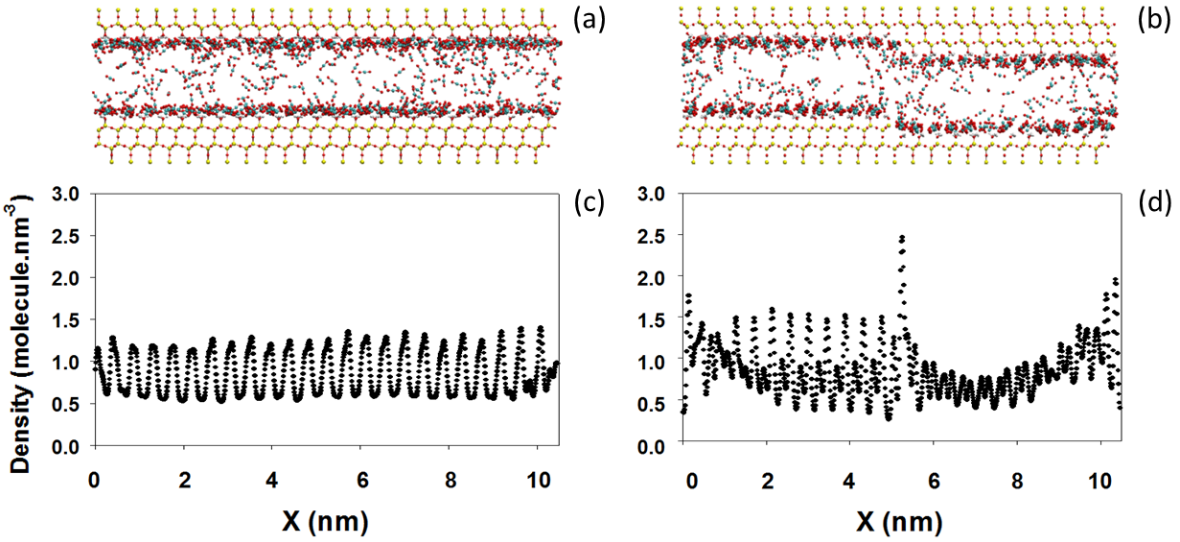

Figure 4-17 (a), (b) Representative simulation snapshots of 900 CO_2 in the pristine and structured pores, respectively, at 300K (the 282 n-octane molecules are not shown for clarity). (c), (d) CO_2 molecular density profiles along the X-direction of the two pore models. The colour code is the same as that used in **Figure 4-1**.

4.3.4. CONCLUSIONS

Extensive equilibrium molecular dynamics simulations for pure n-octane confined within a slit-shaped silica pore of width 1.9 nm were conducted. The simulations were considered at 300K for a fixed amount of n-octane and increasing number of CO_2 molecules. The results show that CO_2 preferentially adsorbs on the silica surface, displacing n-octane towards the pore centre. The n-octane molecules have a preferential parallel orientation with respect to the pore surface and this orientation is enhanced with the presence of CO_2. The capacity for CO_2 is of approximately 1 CO_2 molecule every two –OH groups on our surfaces. When CO_2 loading exceeds this value, CO_2 can be found near the pore center. The results show that self-diffusion coefficient for n-octane increases as CO_2 is added to the system, but eventually reaches a maximum and then decreases because of steric hindrance. Sample simulations conducted with higher loading of n-octane and no CO_2 present, as well as test simulations conduced for pure n-octane in narrower pores confirm that the results just discussed are due to the preferential adsorption of CO_2 on the pore surfaces, which in this way acts as an effective molecular lubricant for n-octane. Within the conditions considered (up to 1100 CO_2 molecules), the results show that the self-diffusion coefficient for CO_2 increases monotonically with its loading. Although this is consistent with the presence of preferential adsorption sites on the pore surface, analysis of the simulation trajectories suggests that even at loadings lower than full CO_2 adsorption capacity can lead to density fluctuations near the pore surfaces, which lead to higher self-diffusion coefficients.

Although the simulations presented here are only conducted for slit-shaped silica pores of one width with a model hydrocarbon chain at one temperature, the results help to complete the understanding about the molecular phenomena related to adsorption and transport of CO_2–hydrocarbon mixtures in sub-surface environments, in addition to those found in the previous sections. Additional test simulations, conducted for a pore of equal volume to the slit-shaped pore considered above, but with step edges present on the surface, suggest that the pore morphology, and in particular the presence of edges, has a strong effect on the fluid behaviour under confinement.

Chapter 5. Confinement Effects on the Hydrogenation of Carbon Dioxide

The material presented in this chapter is ready for submission to the *Proceedings of the National Academy of Sciences* journal.

5.1. ABSTRACT

An important scientific debate focuses on the possibility of abiotic synthesis of hydrocarbons. While on-site measurements near hydrothermal vents support this possibility, laboratory tests have provided data that are in some cases contradicting. Classic thermodynamic arguments suggest that the equilibrium of the Sabatier reaction is shifted to the production of carbon dioxide from methane, while abiotic methane synthesis would require the opposite. However, confinement effects are known to alter thermodynamic equilibria. This manuscript explores whether CO_2 methanation is favoured in the presence of pores, shows that thermodynamic equilibrium can be shifted towards methane production, suggesting perhaps that abiotic hydrocarbon synthesis near hydrothermal vents is possible. This section reports reactive ensemble Monte Carlo (RxMC) simulations for the carbon dioxide methanation reaction. Comparison was made between the predicted equilibrium composition in the bulk gaseous phase and that expected in the presence of confinement, which was provided by slit-shaped pores carved out of silica. In the bulk phase excellent agreement with classic thermodynamic expectations was obtained. The results in the presence of confinement show strong dependency of the reaction equilibrium conversions, X_{CO_2}, and equilibrium constants, K_p, on pore size, pore chemistry, and pore morphology. Conditions that facilitate preferential adsorption of water on the pore walls (e.g., small pore width, high hydrophobicity of pore surface, and rough pore surface) yield an increase in K_p, with the possibility of shifting significantly the equilibrium composition of the reactive system with respect to bulk observations. These results could, perhaps, provide insights on the long controversial debate on the possibility of abiotic organic synthesis in hydrothermal vents.

5.2. LITERATURE RE-EVALUATION

A thorough review on “abiotic synthesis of organic compounds in deep-sea hydrothermal environments” by McCollom and Seewald[123] has been recently provided, giving great details on various Fischer-Tropsch-type synthesis (FTT) laboratory experiments under hydrothermal conditions. All the experiments mentioned were performed within a range of temperatures from 100 to 400°C. This T range is commonly chosen because calculations by Shock and colleagues[124-125] suggest that fayalite-magnetite-quartz (FMQ) and pyrite-pyrrhotite-magnetite (PPM) minerals are able to maintain buffers that condition the chemical reaction

$$CO_2 + 4H_2 \leftrightarrow CH_4 + 2H_2O \tag{5.1}$$

towards the production of methane. The results of such thermodynamic calculations are summarized in **Figure 5-1**, reproduced from the literature.

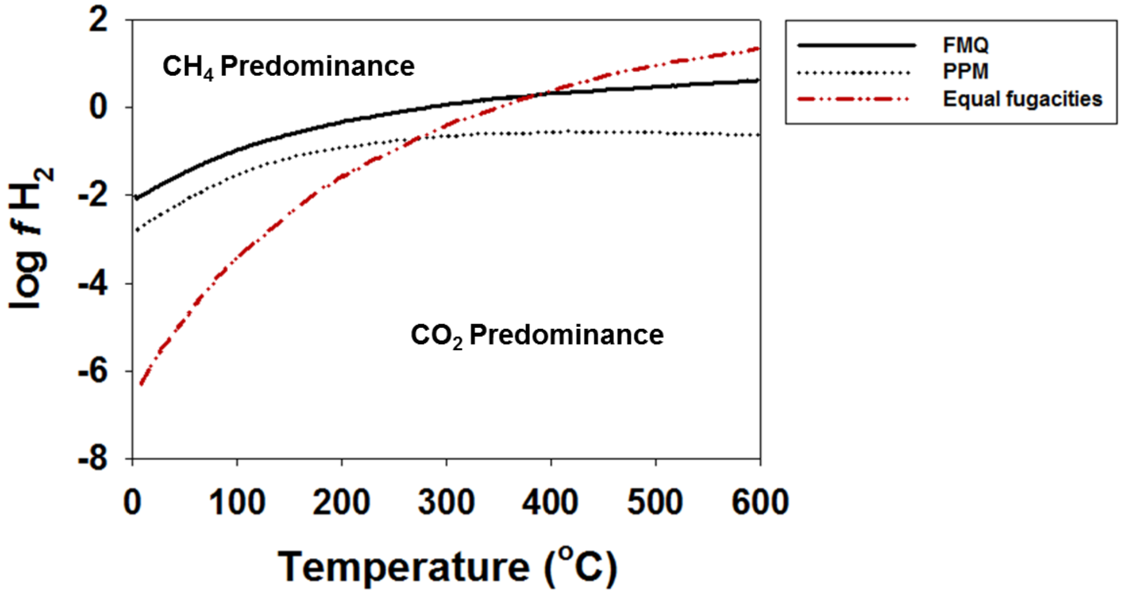

Figure 5-1 Plots of logfH_2 versus temperature calculated for Reaction (5.1) at different mineral buffered oxidation states.[125] The dashed line reflects equal CO_2 and CH_4 fugacities. FMQ and PPM stand for fayalite-magnetite-quartz and pyrite-pyrrhotite-magnetite minerals, respectively. The figure is reproduced from Ref. [125] pg. 351.

To obtain the data shown in **Figure 5-1**, a few basic steps are described by Shock and colleagues:

5.2.1. The Fugacity of Hydrogen Is Set By Mineral Buffer Assemblages

On page 349, Shock (Ref. [125]) explains that the mineral oxidation states of FMQ and PPM by buffer assemblages in hydrothermal systems are due to the following equilibrium reactions

$$\underset{\text{Fayalite}}{3Fe_2SiO_4} + 2H_2O \leftrightarrow \underset{\text{Magnetite}}{2Fe_3O_4} + \underset{\text{Quartz}}{3SiO_2} + 2H_2 \tag{5.2}$$

$$2FeS + \frac{4}{3}H_2O \leftrightarrow FeS_2 + \frac{1}{3}Fe_3O_4 + \frac{4}{3}H_2 \quad (5.3)$$

Pyrrhotite Pyrite Magnetite

Shock stated that "fugacities of hydrogen set by the FMQ and PPM assemblages were calculated with data and equations from Helgeson et al. (1978)".[125] Upon reviewing the source cited,[126] it was found that:

1. There was no data on PPM assemblage;
2. There was no data for H_2; data for the fugacity of oxygen were reported for FMQ, Ref. [126], pg. 181.

Shock explains[125] that the values for the fugacity of H_2 can be calculated using the fugacity of oxygen by empirically fitting experimental data such as those reported by Chou.[127] The data could actually not be found in this reference, but an article by the same author and published in the same year was found.[128] In this article, Chou reported the fugacity of oxygen as maintained by various mineral buffer assemblages; the experiments were conducted using the hydrogen-fugacity sensor technique. Once the fugacity of oxygen is known, that for hydrogen can calculated by using the following equations[128]

$$H_2 + \frac{1}{2}O_2 \leftrightarrow H_2O \quad (5.4)$$

$$(K_w)_T = \frac{fH_2O}{fH_2.fO_2{}^{1/2}} \quad (5.5)$$

To apply these equations, Chou, pg. 4, used data for H_2O fugacity taken from Burnham, Holloway, and Davis (1969) and $(Kw)_T$ values from Robie and Waldbaum (1968).[128]

It is concluded that the fugacity of hydrogen is correct as shown in **Figure 5-1**; however, no confirmation the source for the data regarding PPM can be drawn.

5.2.2. Hydrogen-Fugacity at Conditions for Which the CO_2 Fugacity Equals That of CH_4

By assuming unit activity for water and rearranging the logarithmic form of the law of mass action for Reaction (5.1), it can be shown that (Shock, pg. 93)[124]

$$\log fH_2 = \frac{1}{4}\log\left(\frac{fCH_4}{fCO_2}\right) - \frac{1}{4}\log K \qquad (5.6)$$

It is now possible to solve equation (5.6) when values for the thermodynamic equilibrium constant K are known.

In their original work, Shock and colleagues used the program SUPCRT92 to estimate the constant K. From the value of $\log K = -6.17$ at 600°C and 500 bars reported (which is equivalent to $\log fH_2 = 1.54$ as obtained from **Figure 5-1**) it was estimated that they have employed $K = 6.76\times10^{-7}$ in their calculations (Shock, pg. 94).[124]

The K value can, however, be calculated from classic thermodynamics. The true, dimensionless thermodynamic equilibrium constant K is defined as

$$K = \exp\left(-\frac{\Delta G_{rxn}}{RT}\right) = \prod a_i{}^{v_i} = \prod\left(\frac{f_i}{f_i^o}\right)^{v_i} \qquad (5.7)$$

where ΔG_{rxn} is the reaction Gibbs energy; R is the gas constant; a_i is activity, v_i is the stoichiometry and f_i and f_i^o are the fugacity and fugacity at reference state, respectively, of specie i. Alternatively, K can be obtained by fitting experimental data such as those reported by Swickrath and Anderson.[129] At atmospheric conditions (25°C and 1 bar), the K values obtained using these procedures are 0.84[130] and 0.75,[129] respectively.

Figure 5-2 reproduces **Figure 5-1**, where the conditions at which the fugacity of CO_2 equals that of CH_4 using the estimates for K at 1 bar are re-calculated.

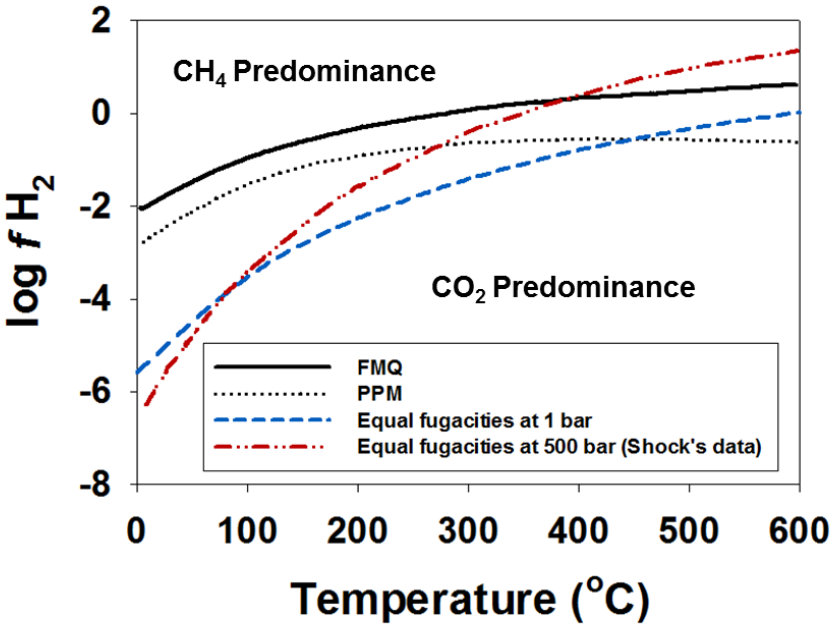

Figure 5-2 Reconstruction of **Figure 5-1** with estimated *K* at 1 bar, obtained from experimental data[129] and classic thermodynamic calculations.[130]

5.3. INTRODUCTION

The discovery of submarine hydrothermal vent systems some forty years ago gave rise to a whole new field of exciting research for both biologists and chemists, which has shaken the core hypotheses of the origin of life.[131-132] The abnormally high concentrations of organic compounds, predominantly methane, measured directly at the vents (black smokers) suggest abiotic organic synthesis, which pointed to the very ultimate question: is it possible that life has emerged from seafloor or subsea floor hydrothermal systems?[133-135] It is within this context that significant effort has been made to investigate the possibility of abiotic hydrocarbon production at hydrothermal conditions. As the industrial Fischer-Tropsch process involves the production of hydrocarbons by CO hydrogenation, it has become common to refer to those possible chemical routes to model abiotic organic formation from various carbon sources as Fisher-Tropsch type (FTT) reactions.[123, 133] Within this general FTT formalism, aqueous CO_2 could be reduced by excess mineral-buffer H_2:

$$CO_2 + [(2 + m/2n)H_2] \rightarrow (1/n)C_nH_m + 2H_2O \qquad (5.8)$$

High hydrogen concentrations could result from water-ferrous silicate interactions, known as serpentinization processes,[136] including, e.g., the serpentinization of olivine, the predominant mineral of ultrafamic rocks:

$$6[(Mg_{1.5}Fe_{0.5})SiO_4] + 7H_2O \rightarrow 3[Mg_3Si_2O_5(OH)_4] + Fe_3O_4 + H_2 \tag{5.9}$$

Olivine Serpentine Magnetite

Serpentinization reactions occurs in the temperature range from 300-400°C, and are highly exothermic.[137-138] It has been estimated that ~660 MJ of thermal energy are released when 300 litres of water alter 1 cubic meter of rock via serpentinization.[138] In the absence of heat dissipation mechanisms, this heat can raise the rock temperature by ~260°C.[138]

Berndt and co-workers[20] were among the first to attempt experimental studies of abiotic hydrocarbon synthesis at conditions representative of deep-sea hydrothermal environments. Using a flexible-cell system, an aqueous bicarbonate-carrying solution and olivine samples were allowed to react at 300°C and 500 bar. After 69 days, H_2 concentration reached 158 mmol/kg and CH_4 concentration was recorded at 82 μmol/kg. Higher-molecular-weight hydrocarbons were also observed. It was concluded that the organic compounds were the products of dissolved CO_2 reduction. Five years later, McCollom and Seewald[21] repeated the experiments, but replaced the carbon source with $H^{13}CO_3^-$, which allowed them to trace the source of carbon in organic matter. Their results indicated that only a small fraction of methane produced contained the ^{13}C from the carbon source. It was concluded that the majority of CH_4, as well as all C_2H_6 and C_3H_8, were generated from thermal decomposition of background organic compounds, which could be present in the mineral at the beginning of the experiments. Similar conclusions were reached in subsequent experiments[139] using different ^{13}C-labelled carbon sources at 175-260°C and 350 bar. On the other hand, Proskurowski et al.[136] recently demonstrated the reduction of CO_2 to CH_4 at the Lost City Hydrothermal Field by measuring stable and radiocarbon isotopes. It was concluded that the distinct "inverse" isotopic trend ($\delta^{13}C_1 > \delta^{13}C_2 > \delta^{13}C_3 > \ldots$) supports the possibility of abiotic organic synthesis rather than thermal decomposition and/or biogenic processes. In particular, radiocarbon data supported the possibility that the carbon source was mantle-derived.[136] This outcome was further supported by stable carbon isotope results described by Shilobreeva et al., who examined different carbon species associated with samples taken from a ridge axis and concluded that CO_2 degassed from magmatic reservoirs is the main source of organic carbon addition to the crust during the alteration process.[140]

It is worth mentioning that in all of the experiments just summarized, only a small fraction of dissolved carbon source was converted to methane (~0.5% CO_2 conversion), despite Reaction (5.8) being strongly favored by thermodynamics (low temperature and high reactant concentrations) and long reacting times, i.e., 1000-2000 hours,[139, 141] indicating large kinetic barriers. The experiments above were conducted by placing the reactants (aqueous carbon sources and substrates) in closed vessels, in which the reactions could occur in both bulk (aqueous solutions) and confined (mineral pores) phases. No attempt could be made to analyse the composition of the system within the pores. In submarine hydrothermal vents systems, however, seawater flows through networks of interconnected fractures to the ocean mantle. The fluids are heated by hot magna chambers and re-emerge onto the sea floor to form the vents. The high concentration of organic matter measured at the vents could therefore be the results from possible biogenic and/or abiotic synthesis throughout the ocean crust, i.e., confined within naturally occurring pores. To understand whether abiotic synthesis is possible, one would need to directly sample the system composition in the pores. This is the goal of the present work, in which MC molecular simulations are employed to quantify the potential effect of pore confinement on the equilibrium conversion expected for CO_2 methanation.

Confinement is known to alter thermodynamic and transport properties of fluids.[142] For example, previous studies documented, using MD simulations, the adsorption, structure, and diffusion of water,[143-145] aqueous electrolytes,[146-147] pure hydrocarbons (**Chapter 3**),[107] and mixtures of hydrocarbons and other substances(e.g., **Chapter 4**)[121, 148-150] in slit-shaped pores at various conditions. Results from **Chaper 4** showed, e.g., that CO_2 preferential adsorption to the pore surface can compete with the adsorption of hydrocarbons, lower the activation energy for diffusion, and enhance hydrocarbon mobility. Similarly, water can preferentially adsorb on silica-based pore surfaces.

Building on these results, the work in this section seeks to explore whether the preferential adsorption of either CO_2 or H_2O on the pore surface can affect the equilibrium conversion of CO_2 methanation. The system considered here is meant to represent a nano-porous matrix at contact with a natural micro-fracture. Water, hydrogen, carbon dioxide and methane are free to exchange between the nano-pores and the micro-fracture and to react within the various environments. The micro-fracture is large enough to provide a ‘bulk’ system, in which classic thermodynamics holds. It has been reported previously that confinement in nano-pores can reduce the activation energy of various chemical reactions,[151] increase the reaction rate,[152] and enhance reaction yields.[153-156] **Figure 5-3** reports a schematic for the hypothetical scenario explored in this section. This scenario is consistent with the conceptual model of a hydrothermal vent discussed by Ingebritsen et al.[157] In summary, seawater flowing into the rock promotes the serpentinization reaction, which alters the rock, could increase the local temperature,[138] and, most importantly, generates hydrogen. As suggested by Shilobreeva et al.,[140] and by Proskurowski et al.,[136] volatile-bearing fluids derived from magmas sourced from the mantle could contain carbon, e.g., CO_2, which comes into contact with this H_2, giving rise to the possible formation of CH_4. While classic thermodynamics arguments support the fact that CO_2 is the favourable product, compared to CH_4, an equilibrium is established between the microfractures and the micropores, which leads to a partition of all the species in the two environments. The scope of this chapter is to investigate whether it is possible that confinement shifts the equilibrium of CO_2 methanation reactions towards the production of methane. Because of computing-power limitations, only one nano-pore is simulated explicitly here, and the molecules can exchange with the bulk (i.e., the microfracture) within the Monte Carlo formalism described below.

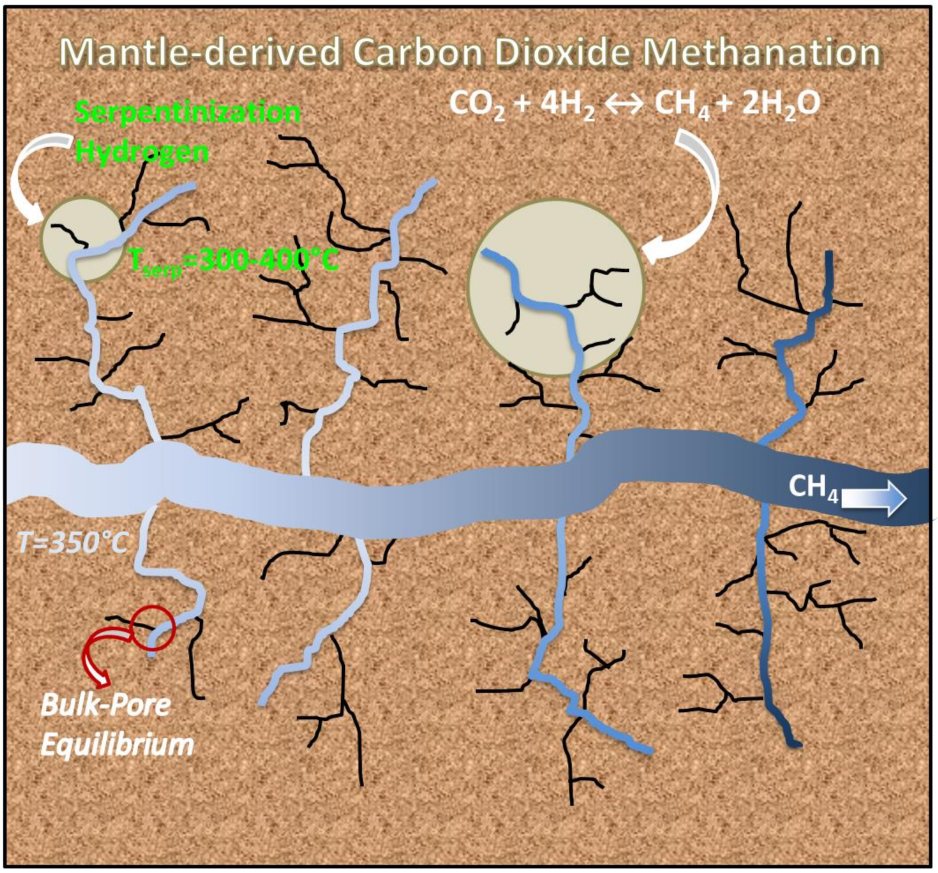

Figure 5-3 Schematic for the possible carbon dioxide methanation process considered in this work. The location is in the oceanic crust, where mantle-derived melt, risen to shallower depths, impacts the basaltic/gabbroic ocean crust driving seawater circulation along natural fractures and microfractures, where serpentinization reactions could take place. The H_2 produced could then come in contact with carbon dioxide from the mantle.

While the interest on the effect of confinement on chemical reaction equilibrium spans multiple disciplines and has enormous practical implications for the chemical industry, experimental measurements are highly challenging, if not impossible, because of the difficulty encountered in monitoring directly the confined spaces, especially at extreme conditions (i.e., high temperature and high pressure). Theoretical approaches can in these circumstances provide the probe of choice. Such approaches include variational perturbation theory,[158] integral equations,[159-161] and molecular simulations, which can provide electron- and/or atomistic-level insights. Implementing ab initio[162] and force-field methods[163-165] it is possible to use simulations to study the breaking and formation of chemical bonds. This section adopted the reaction ensemble Monte Carlo (RxMC) approach,[22-23, 166] whose underlying idea is that equilibrium conversion depends solely on thermodynamics. Smith and Triska[23] and Johnson et al.[22] independently developed the RxMC method, which has been widely and successfully used to investigate bulk-phase reactions,[23, 167] reactions at high temperature[168-169] and high pressure,[170-171] nanoconfined reactions,[153, 155, 172] and even reactions at interfaces.[154, 173-174]

The remainder of the chapter is structured as follows: in the next section the reaction mechanism, the details of the simulation models and the RxMC methodology are discussed. Next, the results are presented and analysed. Then elaboration is made on the possible implications of the results regarding the abiogenic synthesis of methane. Finally, the main conclusions are summarised.

5.4. SIMULATION DETAILS

5.4.1. Reaction Mechanism

Among the family of FTT reactions summarised by Reaction (5.8), this work consider here the methanation of carbon dioxide via the Sabatier reaction.[175-176] RxMC technique does not allow the investigation of CO_2 methanation that could occur microbially by methanogens via methanogenesis.[177] The Sabatier reaction is expressed as:

$$CO_2 + 4H_2 \leftrightarrow CH_4 + 2H_2O \qquad (5.1)$$

The abiotic reduction of carbon dioxide to methane is thermodynamically favourable at low temperature, high pressure, and high hydrogen fugacity. The reaction is reversible and highly exothermic (ΔH = -165 kJ/mol CO_2 at 25°C and 1.01 bar).[178] However, the double carbon-oxygen bonds of the stable CO_2 molecule induce large kinetic barriers that in some cases prevent the reaction from reaching its expected conversion.[179] The use of catalysts is often essential to carry out the reaction, especially at low temperatures.

Park and McFarland proposed the CO_2 methanation as a series of reactions:[180]

$$CO_2 + H_2 + 3H_2 \leftrightarrow H_2O + CO + 3H_2 \leftrightarrow H_2O + CH_4 + H_2O \qquad (5.10)$$

Gao et al. investigated the equilibrium bulk product fraction of Reaction (5.10) at 1.01 bar in the T range 200-800°C using the Gibbs free energy minimization method.[130] The results show that from 200 to ~300°C, little CO is present in the system and the conversion to CH_4 is ~100%. From ~300 to ~500°C, the amount of CO remains negligible; however, because CO_2 methanation is strongly exothermic, the production of CH_4 is hindered in this T range.

While the majority of existing experimental and/or theoretical studies dedicated to the above reactions for industrial uses focus on optimizing the catalysts, this work is concerned here only with the equilibrium conversion. As such, the choice of catalyst, the transient states and kinetics effects are not considered. For the sake of simplicity, this section focuses on the direct hydrogenation of CO_2 (no CO intermediate) [Reaction (5.1)] at moderate pressures in the range of temperatures 200-700°C. The pressure-temperature conditions chosen for the present study provide ideal scenarios for proof-of-principle studies: at low temperatures and high pressures the equilibrium conversion of Reaction (5.1) is expected to favour CH_4 production, hence confinement is likely to have little effect. Temperatures above 500°C are more representative of deeper ocean crustal conditions than of hydrothermal vents, where temperatures are near 350°C. The model considered here is consistent with the conceptual model of a hydrothermal vent discussed by Ingebritsen et al.[157] However, as mentioned above, the serpentinization reaction is highly exothermic, and could lead to local T increases. High temperatures and moderate pressures are chosen here because they facilitate the completion of the calculations, compared to moderate temperatures and high pressures, which would be more realistic. Because high temperatures promote desorption of fluids from nano-pores, confinement effects are more pronounced at low temperatures. Because high pressures are expected to shift the equilibrium of Reaction (5.1) towards the production of CH_4, considering pressures at least one order of magnitude lower than those expected in realistic scenarios allows us to test more reliably the effect of confinement on the equilibrium conversion of Reaction (5.1).

5.4.2. Specifications for the Sabatier Reaction

Turner et al.[155-156] reported the details concerning the RxMC approach combined with the Gibbs ensemble MC algorithm (GEMC). The RxMC approach is designed to determine the equilibrium conditions (by minimizing Gibbs energy at constant temperature and pressure), regardless of the reaction rate and mechanism. To implement the method it is necessary to quantify the probabilities of the forward, P_f, and reverse, P_r, direction reactions, which, for Reaction (5.1), are:

$$P_f = \min\left\{1, \left(\frac{q_{CH_4} q_{H_2O}{}^2}{q_{CO_2} q_{H_2}{}^4}\right) \left[\frac{(N_{CO_2})(N_{H_2})(N_{H_2}-1)(N_{H_2}-2)(N_{H_2}-3)}{(N_{CH_4}+1)(N_{H_2O}+1)(N_{H_2O}+2)}\right] exp\left(-\beta \Delta U_f\right)\right\} \qquad (5.11)$$

$$P_r = \min\left\{1, \left(\frac{q_{CO_2} q_{H_2}{}^4}{q_{CH_4} q_{H_2O}{}^2}\right) \left[\frac{(N_{CH_4})(N_{H_2O})(N_{H_2O}-1)}{(N_{CO_2}+1)(N_{H_2}+1)(N_{H_2}+2)(N_{H_2}+3)(N_{H_2}+4)}\right] exp(-\beta \Delta U_r)\right\} \qquad (5.12)$$

In equations (5.11) and (5.12), q_i is the partition function of specie i; ΔU_f and ΔU_r are changes in the system configurational energy for the forward and reverse reactions, respectively; N is the number of molecules and $\beta = 1/(k_BT)$ where k_B is the Boltzmann constant.

Our simulations contain the following trial moves:

(1) Particle displacement/rotation step.
(2) Forward reaction step:
    a. Delete one CO_2 and four H_2 molecules randomly;
    b. Insert one CH_4 and two H_2O molecules with random orientation;
    c. Accept the move with probability P_f.
(3) Reverse reaction step:
    a. Delete one CH_4 and two H_2O molecules randomly;
    b. Insert one CO_2 and four H_2 molecules with random orientation;
    c. Accept the move with probability P_r.
(4) Phase exchange step for a random particle with probability P^t.
(5) Change in bulk volume with probability P^v.

It is crucial that steps (2) and (3) are chosen with equal probability in order to maintain microscopic reversibility within the reacting systems. Steps (1), (2), (3) and (4) are selected 50, 20, 20, and 10% of the time, respectively, following prior implementations of the method.[155] For all simulations, an initial composition of 1000 CO_2 and H_2 molecules was used, with a molar ratio 1:4. While this molar ratio is chosen to better visualise the effect of confinement on the equilibrium of Reaction (5.1), it should be noted that experimental data from representative hydrothermal vents suggest that the CO_2:H_2 molar ratio in those environments can be as high as 10 or more, but in a few cases the ratio can be lower than 1.[123] All systems were allowed to equilibrate for 1×10^6 moves and the averages were analyzed for 2×10^6 moves. Reaction equilibrium was satisfied by the following criteria:

$$\sum_{i=1}^{S} v_i\,\mu_i = 0 \tag{5.13}$$

where v_i and μ_i denote the stoichiometric coefficient and chemical potential of species *i* for the mixture of *S* components, respectively, as calculated during the RxMC algorithm.

5.4.3. Molecular Models

In this work, hydrogen and methane molecules were treated as monoatomic spheres while each water and carbon dioxide molecule had three Lennard-Jones (LJ) sites and three charge sites. Water was simulated using SPC/E model[33] while CO_2 and CH_4 were simulated using the TraPPE-UA force field.[32] LJ interaction parameters for H_2 were taken from Huber and Herzberg.[31] Dispersive and electrostatic interactions were modelled with the 12–6 LJ and Coulombic potentials, respectively. LJ parameters (ε and σ) for non-like components obtained using Lorentz-Berthelot mixing rules [$\varepsilon_{ij} = (\varepsilon_i\varepsilon_j)^{1/2}$, $\sigma_{ij} = (\sigma_i + \sigma_j)/2$].[34] The cut-off distance for both LJ and electrostatic interactions was set at 1.4 nm, following TraPPE-UA prescriptions.[32] Long-range corrections include (1) tail correction method for LJ potential and pressure calculation and (2) Onsager reaction field method for electrostatic interactions. Vibrational frequencies and rotational constants were obtained from literature.[37-39] The dissociation energy D_0, used to calculate the partition function q_i from its ground-state value, can be determined from the heat of formation at 0K. For a specific molecule, the molecular D_0 equals the sum of $\Delta_f H^0$ from all its individual atoms, subtracting $\Delta_f H^0$ of the molecule itself.

5.4.4. Silica Slit-Shape Pore Models

The silica surfaces used in this work were obtained by cutting the β-cristobalite SiO_2 crystal along the (1 1 1) crystallographic face. A detailed description of the solid morphology is provided in **Chapter 2**. While the pore model does not represent the rocks considered in Reaction (5.9), because quartz (made up by SiO_4 tetrahedra structure) is an abundant mineral in earth, the cristobalite crystal with fully protonated non-bridging oxygen atoms can be considered a possible proxy for hydrophilic rock pore surfaces.[30] Note that this work does not focus on the serpentinization reaction; hence it does not simulate olivine. Instead, β-cristobalite is chosen as a possible substrate, abundant in the sub-surface, which could affect the equilibrium of the Sabatier reaction. The CLAYFF force field is used to describe the solid substrate, as discussed elsewhere.[35] Because of periodic boundary conditions, the systems considered are composed by silica slabs that are infinitely long along the X and Y directions, and separated along the Z direction by the slit-shaped pore. In our model the solid substrate bears no net charge, and all the non-bridging O atoms at the pore surface are fully protonated, yielding a density of surface –OH groups equal to 13.6 OH /nm^2.

This proof-of-principle study stems for the hypothesis that preferential pore-fluid interactions affect the equilibrium conversion of Reaction (5.1). To alter pore-fluid interactions one could change the pore width, with smaller pores in general attracting fluid molecules more strongly than wider pores. The pore width is set at 2 nm, which is expected to strongly attract fluid molecules. Alternatively, pore-fluid interactions can be manipulated by changing the pore surface features, e.g., by altering the degree of protonation of the pore surfaces or by manipulating the force field. Some of these manipulations are discussed in the results section. While this chapter does not explore catalytic effects, it should be noted that some olivines contain Ni, Co or Cr, which could act as catalysts to speed up the reaction considered here.

5.5. RESULTS AND DISCUSSION

5.5.1. Bulk Phase

Gao et al.[130] provide extensive information about the equilibrium constant *K* and product fractions as functions of temperature, pressure and CO_2:H_2 input ratio. The results show that, in summary, low *T*, high *P* and high H_2 concentration favour CO_2 methanation. To validate our RxMC simulations, comparison is drawn between the simulated results here to the data presented by Gao et al. **Figure 5-4** reports the equilibrium constant and in **Figure 5-5** the carbon dioxide conversion and mole percentage of all the compounds as functions of temperature. In all simulations, bulk systems are considered with P =1.01 bar and CO_2:H_2 input ratio 1:4.

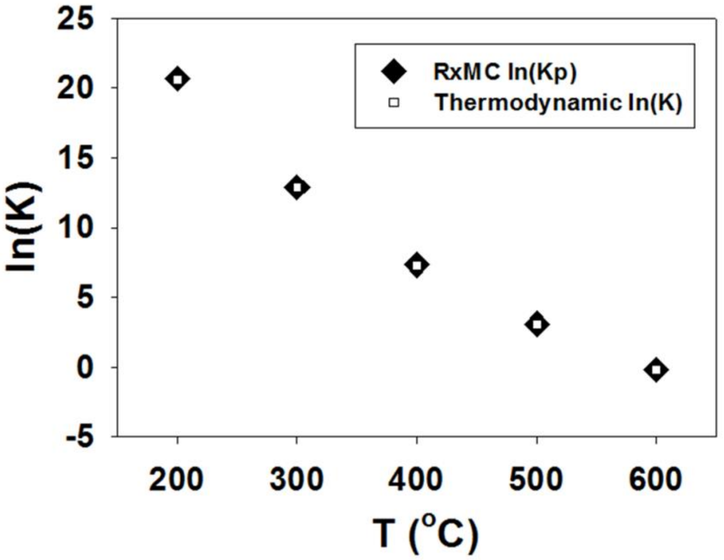

Figure 5-4 Simulated equilibrium constant compared to thermodynamic calculations as a function of temperature for the CO_2 methanation reaction, Reaction (5.1).

Results in **Figure 5-4** demonstrate excellent agreement between the equilibrium constants obtained from classical thermodynamics[181] versus those obtained by simulations implementing the RxMC algorithm. For completeness it should be pointed out that to better match the thermodynamic results the total atomization energy D_0 was slightly adjusted (-150.1 kJ/mol instead of -151.29 kJ/mol[182]). By estimation, varying D_0 by 1.09 kJ/mol changes the equilibrium constant $\ln(K_p)$ by 6.9% for the cases considered in **Figure 5-4**. The conclusions of the present study do not depend on the choice of this parameter, as the value -150.1 kJ/mol was maintained constant for all subsequent simulations discussed in this chapter.

It is important to point out that the *absolute* K is related to K_p by $K = K_p K_\gamma$ with $K_\gamma = \prod_{i=1}^{S} \gamma_i^{v_i}$, where γ_i is the activity coefficient of component i, and the product includes all S components in the system. Because K_γ is not identically equal to unity, there can be a difference of up to 7.3% at 200°C, between absolute K and K_p for the system considered in **Figure 5-4**.

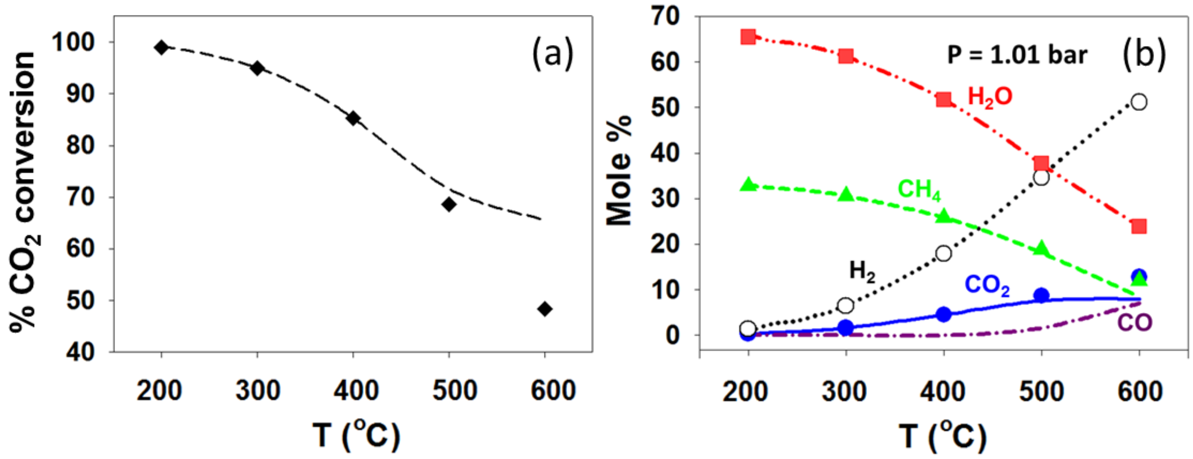

Figure 5-5 (a) Carbon dioxide conversion to CH_4 and (b) mole percentage of all compounds involved in the CO_2 methanation at equilibrium obtained by Gibbs free energy minimization (lines)[130] versus simulations (symbols). The error bars are smaller than the symbols. Note that CO was not simulated, hence only literature results (lines) are shown for this compound.

Panel (a) of **Figure 5-5** compares CO_2 conversion calculated by Gibbs free energy minimization by Gao et al., versus RxMC results calculated here as a function of temperature. Good agreement is obtained at low *T* but the results are markedly different as *T* increases. Panel (b) shows that the molar fractions at equilibrium obtained from the two methods are almost identical: CH_4 production is highly favourable at low *T* but its mole fraction decreases as *T* increases. At high temperature the simulated CO_2 conversion and CH_4 mole fraction predicted by the RxMC method are higher than the values reported by Gao et al.[130] This is a consequence of the fact that Gao et al. considered Reaction (5.10), with the formation of CO intermediate, while this work considers Reaction (5.1), with no CO allowed to form. With the two-step mechanism considered by Gao et al., some of the CO intermediate will react with water to form CO_2 while the remainder reacts with H_2 to form CH_4. At low *T* the production of CO is so low in Reaction (5.10) that the two approaches yield undistinguishable results. Despite such differences, the results shown in **Figure 5-4** and **5-5** suggest that the RxMC approach yields the expected conversions when implemented in the bulk.

To approximate conditions such as those found in deeper oceanic crust below hydrothermal vent environments or in subducting slabs of oceanic crust, this work applies the RxMC formalism to analyse the equilibrium composition of the reactive system in the temperature range 350-700°C at three pressures (10, 30 or 50 bar). While much higher pressures should be considered to emulate systems of oceanic crust relevance, our simulations become problematic at such conditions because the acceptance probability of attempted Monte Carlo moves decreases. However, increasing the pressure is expected to shift the equilibrium of Reaction (5.1) towards the formation of methane, as the number of moles decreases with the formation of products. The lower temperatures considered here are consistent with those expected in hydrothermal vents, and the higher ones are expected to be found near sites where the serpentinization reaction occurs. The results, shown in **Figure 5-6**, confirm that as P increases and as T decreases the CH_4 mole fraction at equilibrium increases. These observations are useful for comparing the results obtained when the reaction occurs in a confined system, which are discussed below.

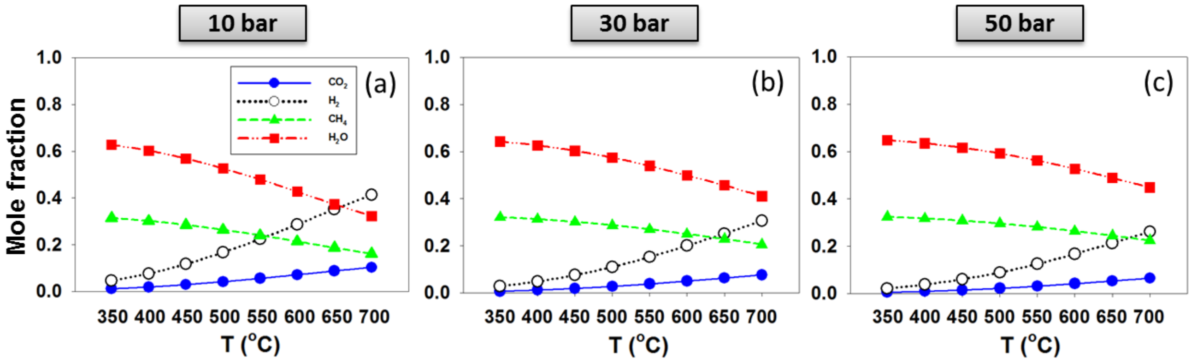

Figure 5-6 Simulated composition for the CO_2 methanation reaction in the bulk phase at (a) 10 bar, (b) 30 bar, and (c) 50 bar. In all cases the initial CO_2:H_2 mole ratio was 1:4.

5.5.2. System in the Presence of Confinement

5.5.2.1. Effects of Temperature, Pressure and initial CO_2:H_2 ratio

This section reports the simulated results when the Sabatier reaction is allowed to occur with the bulk phase is at contact with a narrow pore. Bulk and pore fluids are considered in equilibrium with each other, and as such the fluid molecules can exchange between the two environments. The reaction can occur in either the bulk phase or within the pore. The choice of system conditions has been justified in the Simulation Methodology section. The system parameters are a compromise between computational feasibility, realistic description of the deeper crustal conditions, and the goal of assessing the effect of confinement on the equilibrium transformation of Reaction (5.1). The simulations are conducted at moderate temperatures (350-700°C) and pressures (10, 30 or 50 bar). At these conditions the reaction in the bulk is far from completion and the fluid species can adsorb in the pore. Under these circumstances it is expected that confinement can cause strong effects on the equilibrium conversion of Reaction (5.1). In most simulations, the initial CO_2:H_2 ratio was kept constant at 1:4. These highly reducing compositions are chosen because they provide abundance of hydrogen, allowing us to study the effect of confinement on the equilibrium composition. In a few selected cases (*T* = 350-700°C and *P* = 30 bar), the initial CO_2:H_2 ratio is varied to investigate the effect of this input to the final carbon dioxide conversion.

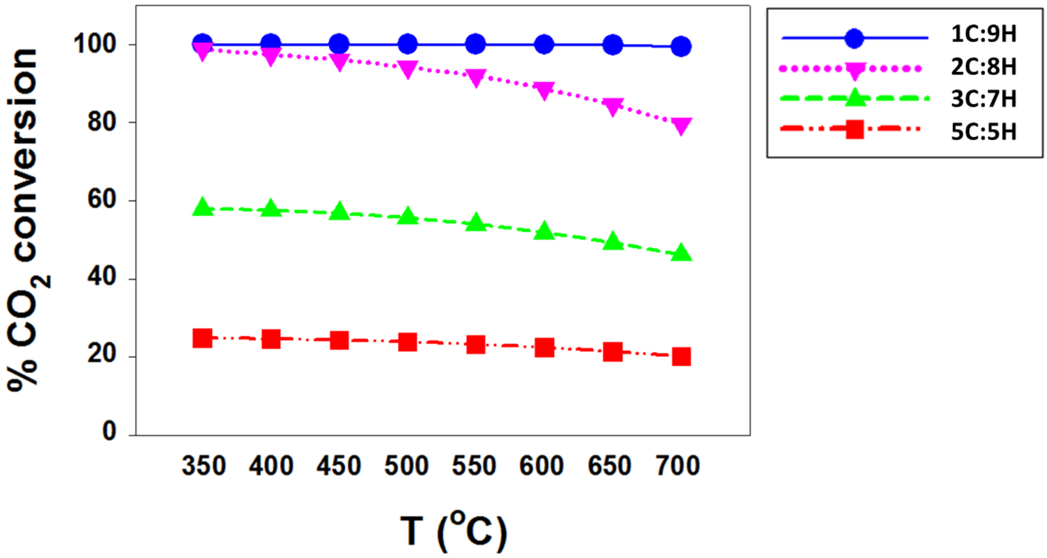

Figure 5-7 Effect of different CO_2:H_2 input ratio on CO_2 methanation.

For all simulations shown in **Figure 5-7**, while the initial CO_2:H_2 ratio was varied, the total number of input molecules was kept constant at 1000 molecules. The result shows that higher H_2 concentration leads to higher CO_2 conversion. At the highest H_2:CO_2 input ratio considered, X_{CO_2} = 99.46% at 700°C and X_{CO_2} reaches 100% at 350°C. Experimental quantification of the composition of dissolved gases in representative hydrothermal vents suggests that the CO_2:H_2 ratio can be as high as 10 or more, but in a few cases the ratio can be lower than 1.[123] Because of the proof-of-principle nature of this work, only the initial molar ratio at 1:4 is considered for the rest of the study. Of course, increasing the amount of hydrogen shifts the reaction towards the production of methane.

Figure 5-8 reports some characterisation data obtained for a system of initial composition 200 CO_2 and 800 H_2 that was allowed to react and reach equilibrium at 650°C and 50 bar. Panel (a) represents a sample snapshot for the slit-pore containing 6 CO_2, 10 H_2, 84 CH_4 and 216 H_2O molecules within the pore volume in equilibrium with a bulk phase (panel c) containing 12 CO_2, 62 H_2, 98 CH_4 and 103 H_2O molecules at 650°C and 50 bar. The bulk region is a cubic box whose size changes. A typical volume at the end of a simulation run is of size 9.4×9.4×9.4 nm^3, simulated within periodic boundary conditions in the 3 directions.

The section below discusses how the equilibrium composition of the system can depend on the relative amount of pore versus bulk volume.

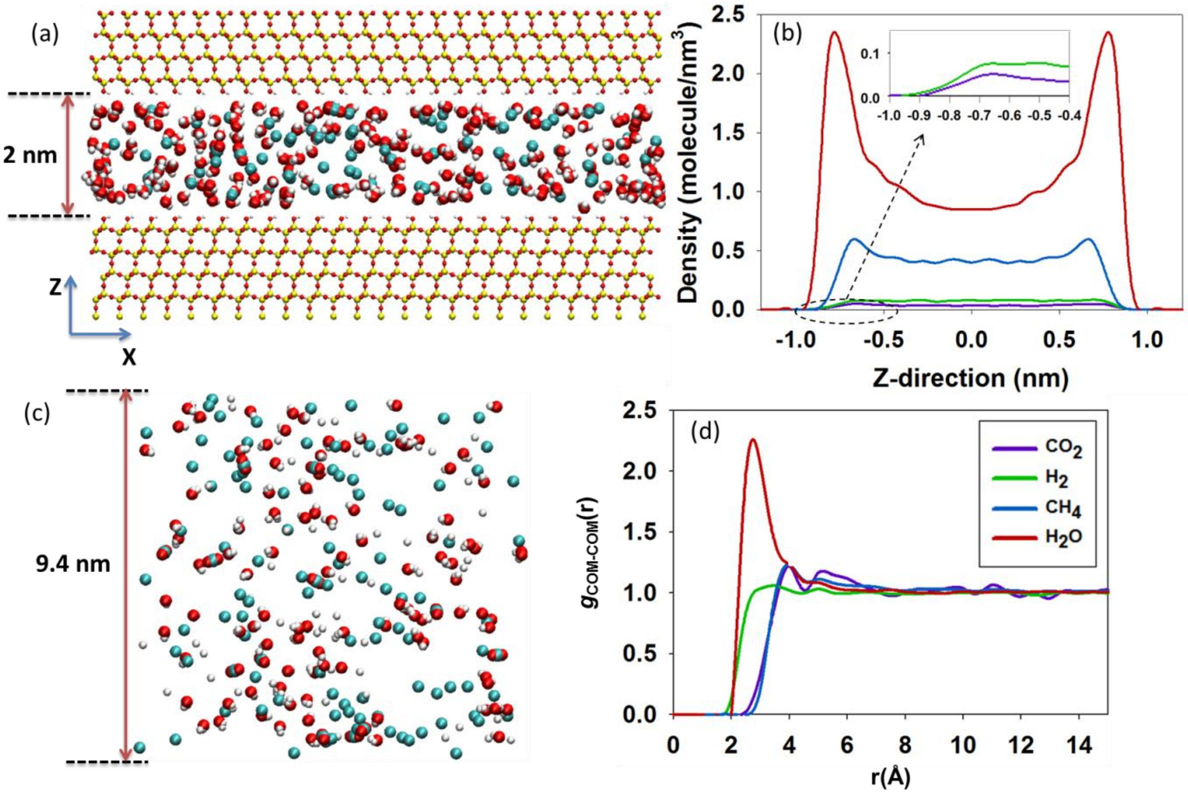

Figure 5-8 (a) Snapshot representing a simulation box containing the 2 nm silica pore at 650°C and 50 bar. The solid silica slabs are continuous along X and Y directions. Cyan spheres are either CH_4 or C in carbon dioxide, red is O, white is either H or H_2, and yellow is Si. (b) Density profiles of CO_2, H_2, CH_4 and H_2O adsorbed within the *confinement*. (c) Snapshot of the cubic bulk simulation box. (d) Radial distribution functions between the centres of mass $g_{COM\text{-}COM}(r)$ for the fluids in the *bulk phase*.

Panel (b) of **Figure 5-8** reproduces the atomic density profiles of molecular COMs as a function of the distance Z perpendicular to the pore surface for the system depicted in panel (a). The reference Z=0 is the centre of the pore. Statistically, only negligible amounts of CO_2 and H_2 adsorb into the pore. In the density profiles obtained for methane and water two distinct peaks are observed, symmetric with respect to the pore centre, and near the pore surfaces. The positions of the water peaks are closer to the pore walls, in comparison to the methane peaks. This confirms that water is strongly adsorbed on the pore surfaces, because of its capability to form hydrogen bonds with the hydroxyl groups on the pore walls. Although CO_2 can also form hydrogen bonds with the surface –OH groups,[111-112] there is too little H_2 and CO_2 available in the pore at reaction equilibrium, in comparison to methane and water, to observe significant peaks. Lastly, panel (d) of **Figure 5-8** shows the COM-COM radial distribution functions (RDFs) of the substances in the bulk phase. Only one distinct peak is observed in each RDF, indicating well-mixed gaseous structures. Note that both simulation snapshots confirm that the various components yield a well-mixed single-phase system, probably consistent with the supercritical conditions expected in sub-surface systems.

Figure 5-9 shows the mole fractions for each component at equilibrium. Note that it is differentiated between the overall mole fraction (middle panels), from the mole fraction in the bulk (left panels) and in the pore (right panels). The overall data are obtained by considering both the fluids in the bulk and those in the pore, i.e., by counting the molecules of H_2O, CH_4, H_2 and CO_2 in the two boxes at equilibrium. From top to bottom, the results are obtained at larger pressures.

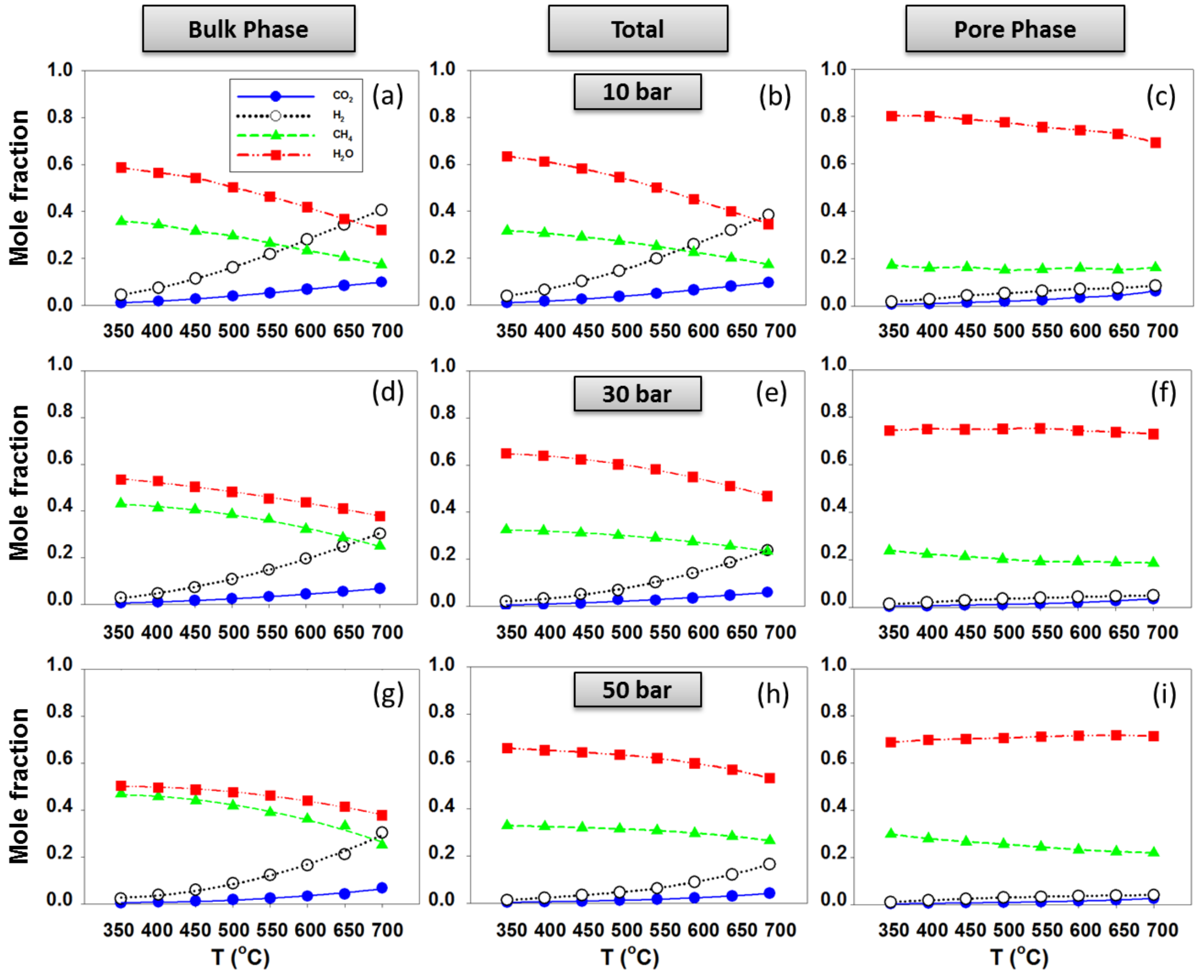

Figure 5-9 Simulated product fraction of CO_2 methanation for the bulk phase (left panels) and pore phase (right panels) in equilibrium with each other at *T* and *P*. The middle panels show the total molecular fraction.

Results from **Figure 5-9** clearly show the pronounced effect of confinement on the reaction yield (bulk system adjacent to nanoporous matrix). While the bulk composition and the system total composition (left and middle panels) have somewhat similar trends with the reaction yields observed for the pure bulk systems discussed above (i.e., see **Figure 5-6**), the pore composition is distinctively different, with water as the dominant substance in all cases. In the confined phase, only negligible amounts of CO_2 and H_2 are detectable, while CH_4 can be adsorbed in a substantial amount.

From the equilibrium mole fractions, the equilibrium constants, K_p can be calculated to quantify the effect of confinement on the equilibrium conversion as a function of T and P. **Figure 5-10** presents K_p for pure bulk phase and confined phase as obtained using the mole fraction values shown from **Figure 5-6** and from the right panels of **Figure 5-9**, respectively. It can be seen that the effect of temperature on the reaction equilibria is much stronger than that of pressure for the range of T and P considered. The results obtained in the bulk are practically indistinguishable. Nonetheless, the composition of the confined system is significantly different compared to the bulk at all pressures and temperatures considered. Our results suggest that the presence of the silica pores effectively reduces the mole fraction of water, a reaction product, from the bulk phase. As a consequence, the equilibrium of Reaction (5.1) in the bulk phase is shifted further to the right, yielding a final CO_2 conversion of the 2-phase system higher than that of the single bulk phase system. These results strengthen the arguments discussed by McDermott et al. regarding possible pathways for abiotic organic synthesis at submarine hydrothermal fields.[183]

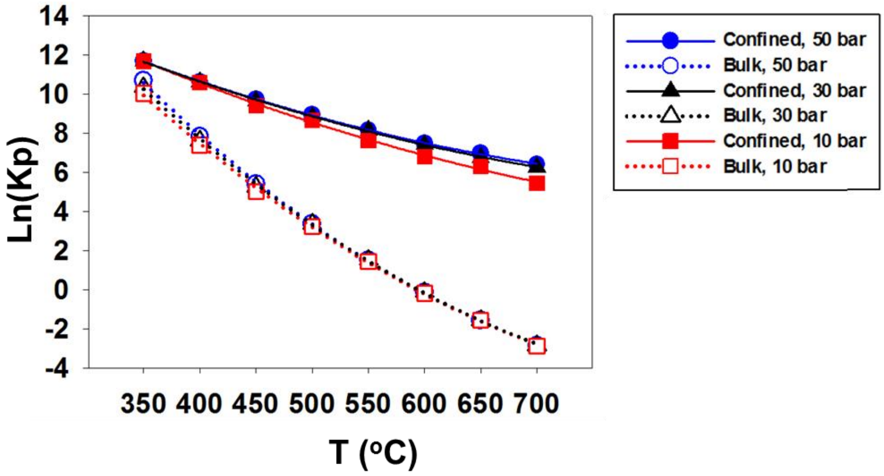

Figure 5-10 Simulated equilibrium constant K_p for pure bulk versus confined phases at P = 10, 30 and 50 bar. Different colours represent different system pressure.

Note that the overall conversion of the chemical reaction can be shifted by changing the amount of pore volume in the host matrix with respect to the bulk volume, as controlling this ratio while maintaining pore width and pore chemistry allows manipulating the amount of water present in the bulk phase. For example, if the pore X and Y dimension increases while the bulk volume remains constant, more water would adsorb in the pore, lowering the water mole fraction in the bulk phase and shifting the equilibrium further towards CH_4 production.

5.5.2.2. Effects of Pore Size, Pore Chemistry and Surface Roughness

In natural systems, fractures usually have a wide range of pore size distribution whereas their surfaces are highly heterogeneous, both in chemical composition and morphological structure. In general, there are more small fractures compared to large ones and they have fractal relation.[184] Because confinement has a large effect on the overall system equilibrium via the adsorption of water, it is expected that varying those factors that control fluid adsorption will result in noticeable changes in the reaction yield. In this section, the effects of the pore size, pore chemistry and surface roughness are quantified.

Figure 5-11 compares the CO_2 conversion, X_{CO_2} (panel a), and K_p in confinement (panel b) for simulations such as those discussed in **Figure 5-9** when the slit-shaped silica pore width is reduced from 2 nm to 1 nm. The reduction of the pore width results in two important outcomes. While the density of confined water increases, the pore volume is reduced by a factor of ~2. Recall that in our RxMC simulations the pore volume remains constant, while the bulk volume fluctuates to maintain the bulk *pressure* constant. Because the *total amount* of adsorbed water in the narrower pore is less than that in the 2 nm pore at higher T (~500-700°C), the corresponding $X_{CO_2\text{-}1nm}$ is lower than $X_{CO_2\text{-}2nm}$ (panel a) in this range. At 300 and 500°C the opposite is observed.

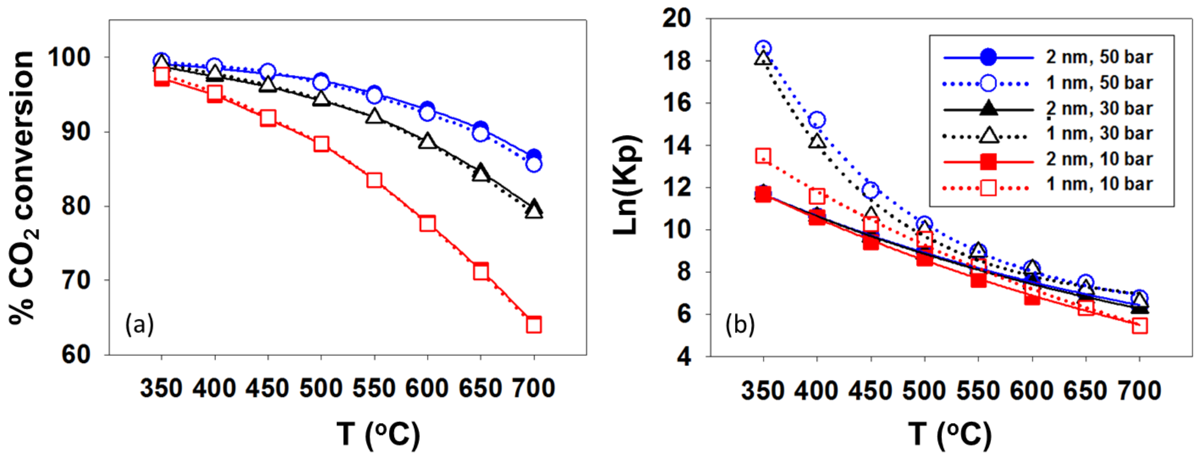

Figure 5-11 (a) Carbon dioxide conversion to CH_4 and (b) confined equilibrium constant for 2-phase reaction in contact with slit-shape silica pores of width 1 nm versus 2 nm.

The effect of pore chemistry was quantified by varying the ‘hydrophilicity’ of the pore surface. Following a prior simulation effort, different amounts of hydrogen atoms were removed from the surface hydroxyl groups, leaving the non-bridging oxygen atoms exposed to the confined solution.[26] Our prior results have shown that reducing by ~50% the number of H atoms on the silica surface yields an increase of ~30% of pure water adsorbed in a pore of width 1.2 nm at ambient conditions; while a complete removal of H atoms from the surface –OH groups results in 40% additional water content. While prior simulations were conducted using MD simulations, our Monte Carlo approach yields consistent results, as shown in **Figure 5-12**, where the number of water molecules adsorbed in the various pores is shown as a function of surface features and of temperature. Panel (b) of **Figure 5-12** shows the effect of water adsorption on CO_2 conversion, which is quite pronounced.

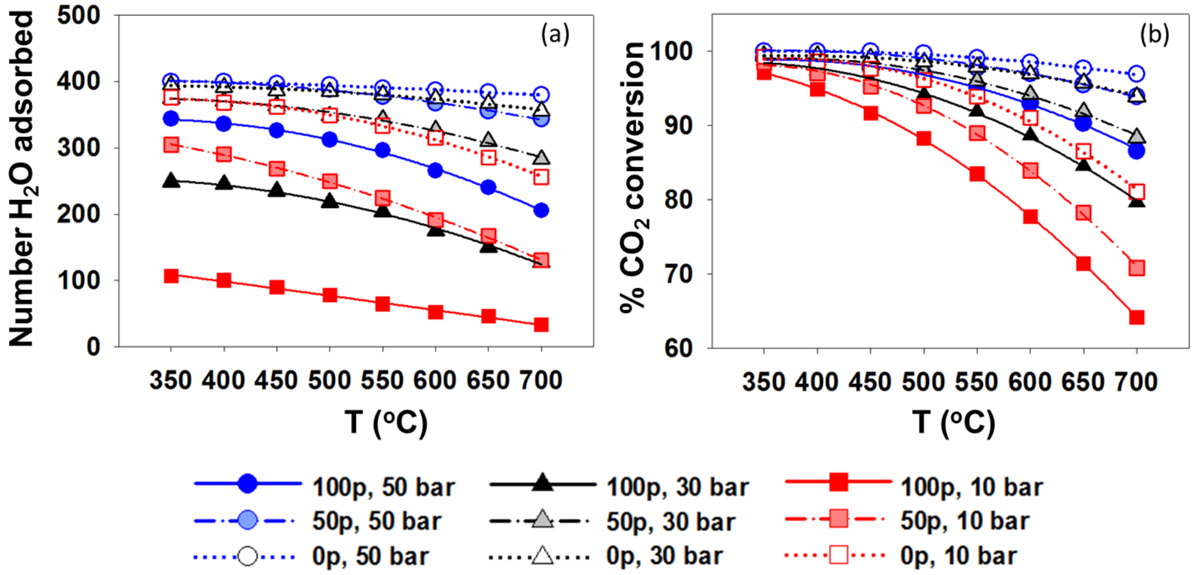

Figure 5-12 (a) Number of water adsorbed in the pore phase and (b) *overall* carbon dioxide conversion for the silica substrates with different degrees of protonation. The fully protonated silica pore surface is denoted as "100p"; surfaces obtained by removing ~50% and 100% of the H atoms form the surface –OH groups are denoted as "50p" and "0p", respectively.

An attempt is also made to *decrease* the pore hydrophilicity by covering the silica surface with a fixed layer of methane. Note that this is an unphysical scenario permitted by the simulation procedure. The resultant material could be considered a carbon-based pore. The procedure implemented in our simulations is described below.

Canonical ensemble MD simulation was run for 3000 methane molecules confined in the silica pore of 2 nm at 500°C. Density profile of methane across the pore width was produced and shown in **Figure 5-13**. Methane molecules that did not belong to the first adsorbed layers were removed. The final configurations had either (1) 1132 methane molecules lying within a distance of D = 3.74 Å (which roughly equals the methane diameter of 3.73 Å)[32] or (2) 420 methane lying within a distance of $D_{½}$ = 1.87 Å away from the silica pore walls (see **Figure 5-13** for illustration). Since methane molecules bear no charge, no charge adjustment are required for the silica pore. Simulated snapshots and contour plots for methane planar densities on top silica surface for the two cases are shown in **Figure 5-14**.

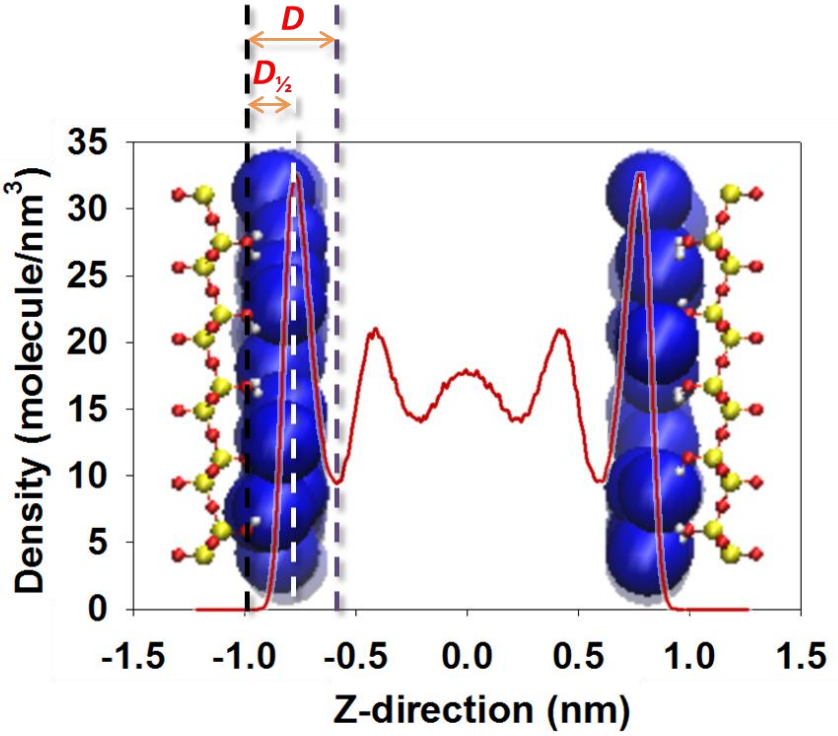

Figure 5-13 Molecular density profile of 3000 methane confined in 2 nm silica pore at 500°C and illustration for the methane molecules chosen for coating purpose. Blue spheres are the adsorbed CH_4, red is O, white is H, and yellow is Si.

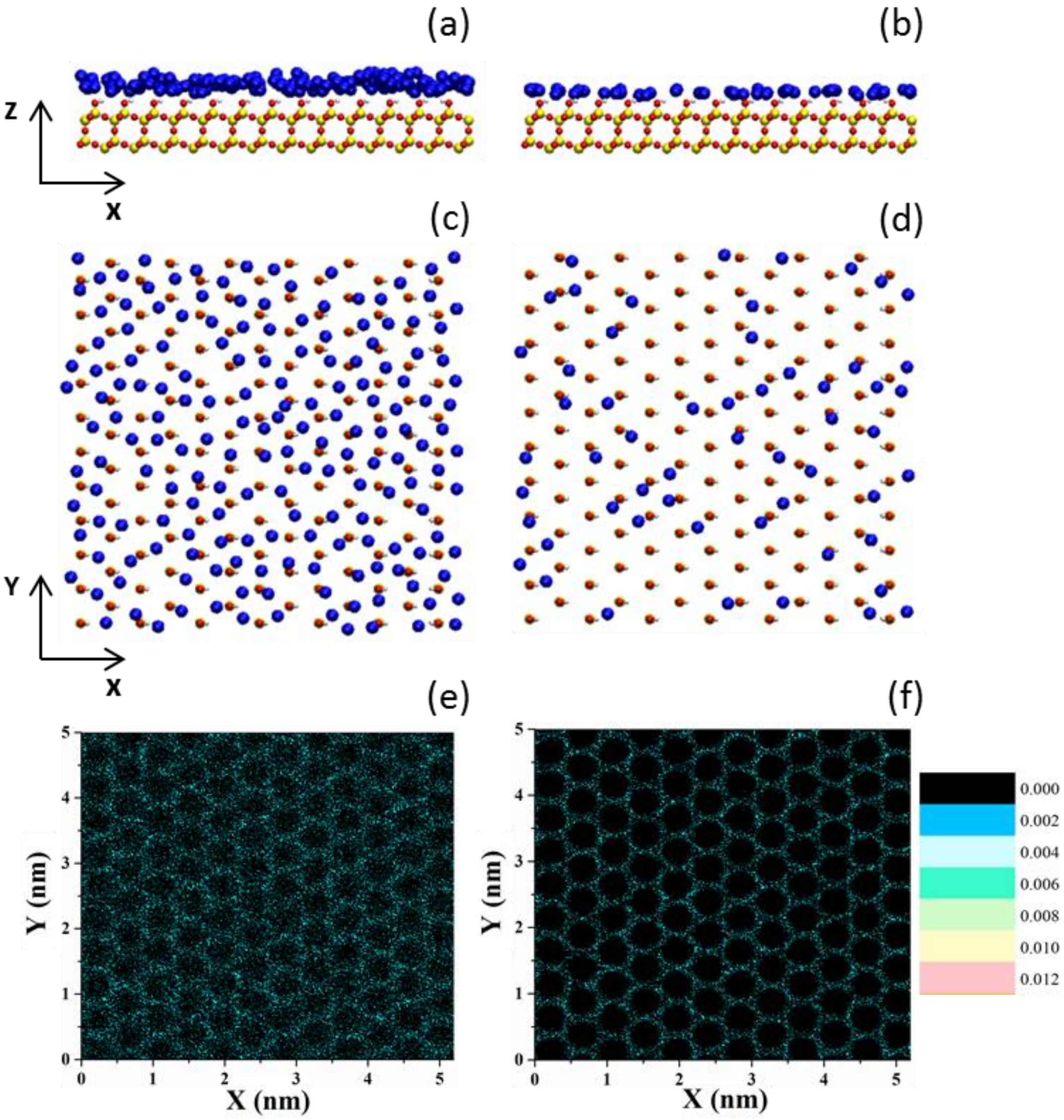

Figure 5-14 (a), (b), (c), (d) Simulated snapshots of the first adsorbed layers of 1132 (left panels) and 420 (right panels) methane molecules on silica surface along different planes, respectively. Only a few layers of silica are shown for clarity. Colour scheme is the same as that of **Figure 5-13**. (e), (f) Corresponding contour plots of methane planar densities along X-Y plane. Densities are expressed in number of molecular COM per 10^{-4}nm^2.

The adsorbed methane layers are treated as fixed during the RxMC simulations and as such they become part of the solid substrate and are not counted when the equilibrium conversions are assessed. The results in term of number of water adsorbed in the pore phase and overall carbon dioxide conversion are shown in panel (a) and (b) of **Figure 5-15**, respectively. As the number of methane placed on the pore surface increases, the number of water molecules adsorbed decreases, hence reducing the reaction yield.

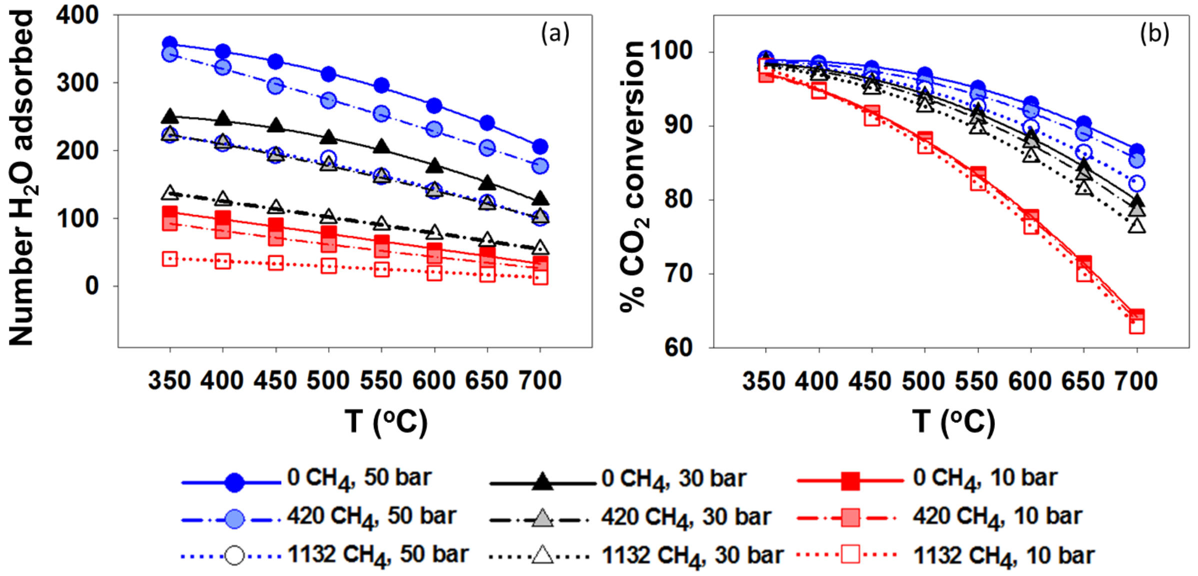

Figure 5-15 (a) Number of water adsorbed in the pore phase and (b) *overall* carbon dioxide conversion when the silica substrates are covered with different numbers of methane molecules. Note that the pristine silica pore surface is denoted as "0 CH_4".

Finally, the effect of the pore surface morphology by inserting two step-edges along the Y-direction (hence creating a structured pore with a trench on its surface) is quantifed. The procedure implemented is explained in section **4.3.2.** A sample snapshot of the pore is shown in **Figure 5-16**.

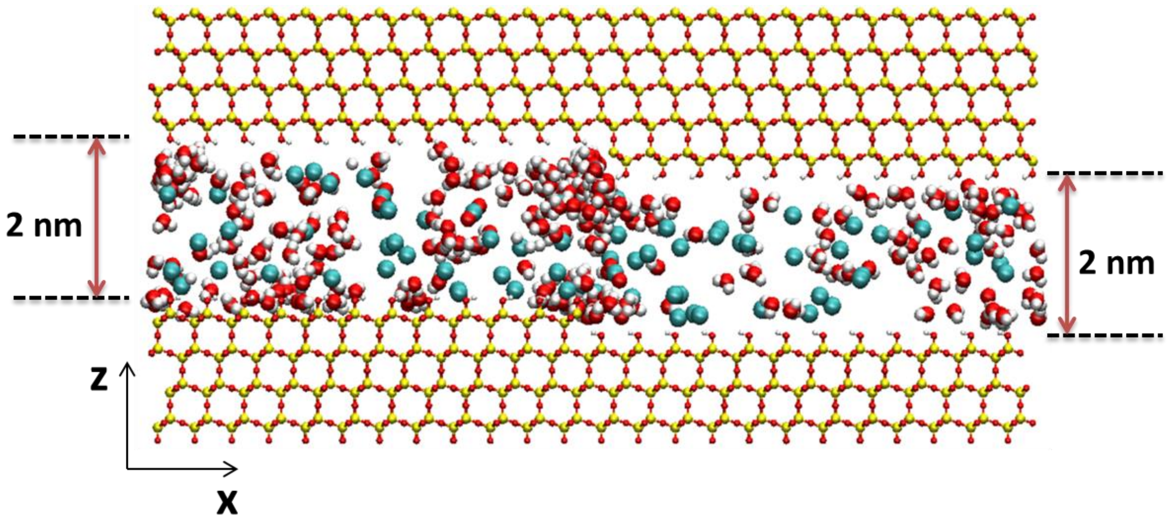

Figure 5-16 Simulated snapshot representing a simulation box containing the 2 nm structured silica pore at 650°C and 50 bar. The solid silica slabs are continuous along both X and Y directions. Cyan spheres are either CH_4 or C in carbon dioxide, red is O, white is either H or H_2, and yellow is Si.

Previously in **Chapter 4**,[18] CO_2 was found to accumulate near the surface edges. In the present system, water accumulates near the surface edges, and CO_2 is present in too little amount within the pores to compete for these preferential adsorption sites (see **Figure 5-16**). As a result, the equilibrium conversion of the reaction can be affected. Results in term of mole fractions are presented in **Figure 5-17**, which, indeed, shows an increase in the amount of adsorbed water and overall reaction yield.

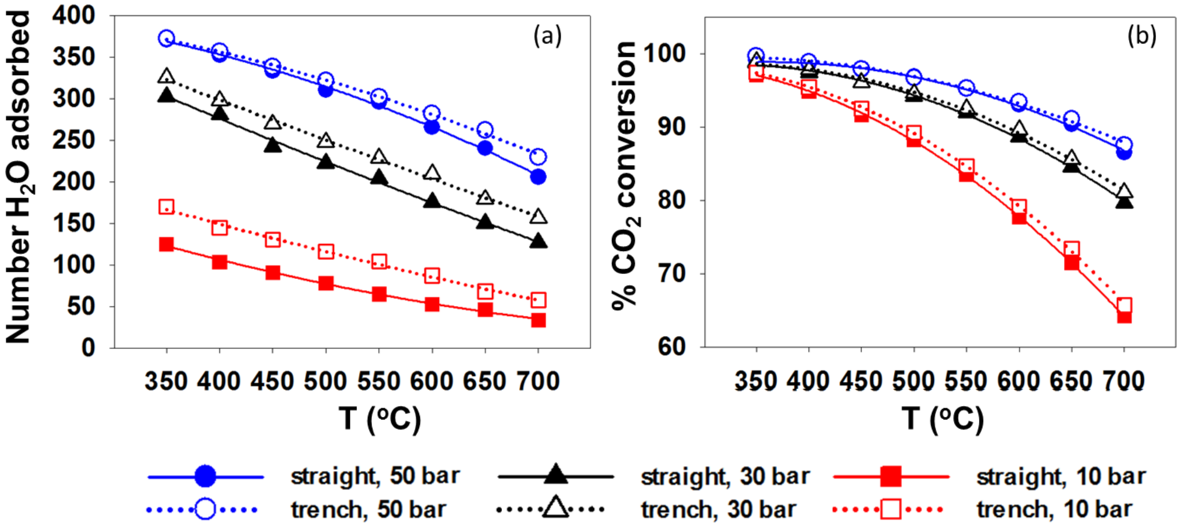

Figure 5-17 (a) Number of water adsorbed in the pore phase and (b) *overall* carbon dioxide conversion for silica substrates of different morphologies. In the figure legend, the term "straight" refers to the pristine silica pore (see **Figure 5-8a**) while "trench" refers to the structured pore (see **Figure 5-16**).

5.6. CONCLUSIONS

Reactive ensemble Monte Carlo simulations were conducted for the methanation reaction in either the bulk phase or for the bulk phase in equilibrium with a silica nanopore (a fracture-nanopore network system). The results in the bulk phase are in agreement with prior reports, and show that high pressures and low temperatures favour the production of methane from CO_2. The situation can be affected by the adsorption of the fluids in pores. To explicitly consider the effect of confinement, slit-shaped pores carved out of silica was generated. The silica surfaces were constructed from β–cristobalite crystals. The results show that preferential adsorption of the fluids in the narrow pores can affect equilibrium. In agreement with Le Chatelier's principle, when water, one product, is preferentially adsorbed, "*the position of equilibrium moves to partially reverse the change*", yielding more water, and consequently more methane, thus enhancing the overall reaction conversion. The effects of pore size, pore chemistry and pore morphology were investigated. All conditions that enhance water adsorption (i.e., increasing pore hydrophilicity or roughness) result in an enhancement of reaction yield.

This study could shed light on the possibility of abiotic conversion of CO_2 to hydrocarbons within hydrothermal vent systems. Should the Sabatier reaction occur in these environments, it would take place within the oceanic crust perhaps influenced by strong confinement effects. The work presented in this chapter suggests that confinement can shift the reaction equilibrium towards facilitating methane formation at conditions that should not be strongly kinetically limited (i.e., moderately high temperature and low pressure). These results support the possible existence of realistic pathways for the abiotic organic synthesis discussed by, e.g., McDermott and coworkers.[183]

Chapter 6. Summary and Outlook

6.1. SUMMARY

Nanoporous materials, together with their inherent interfacial and confinement effects, have played crucial roles in numerous subsurface phenomena, from adsorption to diffusivity to reactivity. Understanding the fundamental underlines for the behaviors of fluids in confinement at atomistic level has been proven critical for the practical applications of carbon dioxide capture and storage strategies and tertiary enhanced oil recovery strategies, or for clarifying the possibility of new hypotheses.

Throughout the course of my research, the structural, thermodynamic and kinetic properties of various fluids confined within β-cristobalite silica substrate were investigated in great details by the means of Molecular Dynamics (MD) simulations. Additionally, thermodynamics of chemical equilibrium of the carbon dioxide methanation in nano-porous matrix was studied using Reactive Ensemble Monte Carlo (RxMC) method. All simulated results were compared to experimental and/or theoretic reports from literature, wherever applicable.

Explicitly, in **Chapter 3**, equilibrium MD simulations are performed for pure propane in silica pore of different pore widths and operating conditions. Adsorption isotherms and excess sorption were quantified at constant temperatures and increasing bulk pressures. At fixed temperature the excess sorption is found to show a maximum near the pressure at which the pores fill. At fixed pressure the excess adsorption is found to decrease as the temperature increases and as the pore width expands. At equilibrium, pronounced layering was observed for propane near the pore surface, especially in the narrower pore and at the highest densities considered. The propane molecules at contact with silica tend to lay with their molecular plane and CH_3-CH_3 vector parallel to the pore surface. The mean square displacement as a function of time was used to quantify the self-diffusion coefficient of confined propane as a function of temperature, pressure and pore width. The results show that as the system T rises and as the pore expands, D_s increases. On the other hand, as P increases, D_s decreases.

Chapter 4 presents the MD simulated results for the binary mixtures of CO_2 and either n-butane or n-octane in silica confinement at a range of mixture concentration, mixture composition and temperature. Atomic density profiles substantiate strong interactions between CO_2 molecules and the protonated pore walls. Preferential adsorption of carbon dioxide near the –OH groups on the surface was observed, where the adsorbed CO_2 molecules tend to interact simultaneously with more than one –OH group. CO_2 self-diffusion coefficients depend on pore loadings following the type IV behavior in the classification proposed by Karger and Pfeifer.[113] Non-monotonic change in n-octane self-diffusion coefficients as a function of CO_2 loading was observed. In general, CO_2 preferential adsorption to the pore surface is likely to attenuate the surface adsorption of n-alkanes, lower the activation energy for n-alkanes diffusivity, and consequently enhance n-alkanes mobility at low CO_2 loading. At high CO_2 loading, n-octane diffusivity is hindered by molecular crowding and displays a maximum. In contrast, within the concentration range considered, the self-diffusion coefficient predicted for CO_2 exhibits a monotonic increase with loading, which is attributed to a combination of effects including the saturation of the adsorption capacity of the silica surface. Test simulations suggest that the results are strongly dependent on the pore morphology, and in particular on the presence of edges that can preferentially adsorb CO_2 molecules and therefore affect the distribution of these molecules equally on the pore surface, which is required to provide the effective enhancement of the hydrocarbon diffusivity.

Lastly, in **Chapter 5**, RxMC in conjunction with constant pressure Gibbs ensemble Monte Carlo was performed to study the chemical equilibrium of carbon dioxide to methane under silica nano-confinement at different pore properties and operating conditions. In the bulk phase, excellent agreement with thermodynamic expectations based on the Gibbs free energy minimization was obtained. The results in confinement show strong dependency of the reaction equilibrium conversions, X_{CO_2}, and equilibrium constants, K_p, on pore size, pore chemistry, and pore morphology. Conclusively, the results could provide some insights to settle various controversial literature observations within this field of research and reasonable supports for the origin of life from deep sea through abiotic synthesis of organic compounds.

6.2. MULTI-REACTIONS REACTIVE ENSEMBLE MONTE CARLO, REACTIVE FORCE FIELD MONTE CARLO AND RXMC IN COMBINATION WITH TRANSITION-STATE THEORY

The study of carbon dioxide methanation in confinement can be improved by adapting more complex reaction mechanism (e.g., two-step mechanism proposed by Park and McFarland).[180] In fact, at temperatures greater than 500°C, classic thermodynamics supports a large production of CO in competition with CH_4.[130] Moreover, as mentioned in **Chapter 5**, all of the experiments on abiotic FTT reactions are heavily limited by kinetic barriers. Therefore, a more comprehensive understanding of the reaction mechanism in the silica nano-pore should be investigated. Is it possible that confinement reduces the reaction activation energy E_a as seen elsewhere?[151] Potential methods may involve the use of ReaxFF,[165] a reactive force field which describes the properties of bond breaking and bond forming, thus providing information on the rate of reaction. Another alternate approach is the method combines the transition-state theory formalism with the RxMC simulation to investigate the chemical reaction rate and the structure and activation energy of the transition states.[152] Lastly, a substrate model that is more similar to those found in the ocean crust (e.g., serpentinite, basalt, etc.) coating with possible natural catalytic sites (e.g., metals and oxides) could be employed to obtain more realistic and reliable results.

The results in **Chapter 5** can also be used to further understanding and optimization toward new applications (e.g., carbon capture and utilisation or CCU). Perhaps, methane production quantity and production rate via Sabatier reactions could be increased with the use of nano-reactor instead of the traditional fluidized bed reactor employed in many industrial Fischer-Tropsch applications.

Appendix – Quasielastic Incoherent Neutron Scattering and Bridge to Molecular Dynamics Simulation

The material presented in this chapter is the result of a joint project, collaborated with Dr. David Cole and Dr. Siddharth Gautam at The Ohio State University, USA. Molecular Dynamics simulations were carried out at UCL whereas experiments were implemented at the Oak Ridge National Laboratory (ORNL), Tennessee, USA. Data analysis was performed by Dr. Siddharth Gautam at The Ohio State University.

A.1. INTRODUCTION TO NEUTRON SCATTERING

Neutron scattering is a powerful experimental technique where a concentrated beam of neutrons, carrying initial energy E_i and neutron wave-vector $\boldsymbol{k}_i$, is made to scatter from sample substances of interest. Returning signals from the scattered neutrons, containing final E_f and $\boldsymbol{k}_f$, give intensive information about the material structural and dynamic properties at molecular scale. The measured intensity is proportional to the dynamic structure factor $S(\boldsymbol{Q}, \omega)$, also called the scattering law. Here, $\boldsymbol{Q} = \boldsymbol{k}_f - \boldsymbol{k}_i$ is the momentum transfer and $\hbar\omega = E_f - E_i$ is the energy transfer with ħ being the reduced Planck constant.

Depending on the nuclear isotope, the scattering can be *predominantly* incoherent or coherent. In coherent scattering, neutron waves can either (1) combine in phase and add up to relatively high irradiance (constructive interference) or (2) combine 180° out of phase and cancel each other, which yield zero irradiance (destructive interference). Random waves that combine in different phases and nearly cancel out or yield very low irradiance are classified as incoherent scattering. Note that all nuclear isotopes can scatter coherently. However, in the case of hydrogen, incoherent scattering is dominant over the coherent contribution. Inelastic incoherent scattering describes the dynamic of individual particles (self-correlated motion, e.g., self-diffusion) while inelastic coherent scattering provide information about material structure and collective dynamics (correlated motion) of the whole system. This study is limited to incoherent scattering.

A typical incoherent neutron scattering spectrum can be divided into the following basic parts:

(1) Elastic scattering – no energy transfer ($E_f - E_i = 0$). In theory, dynamic structure factor, $S(\boldsymbol{Q}, \omega)$, should be a delta function at $\omega = 0$ (red line in **Figure A.0-1**). However, due to the instrumental limitation, experimental signals are convoluted with instrumental resolution and thus have a finite width.

(2) Inelastic scattering – some energy transfer ($\mathrm{E_f - E_i} \neq 0$). Signals have peaks at non-zero energy transfer. This part reflects periodic motions, including lattice vibrations (phonons) and intramolecular vibrational modes.

(3) Quasielastic scattering – special case of inelastic scattering with small energy transfer leading to a broadening of elastic line ($E_f - E_i \approx$ up to meV around ‘0’). Signals have peaks at zero energy transfer, but are broadened compared to the instrumental resolution due to diffusive processes.

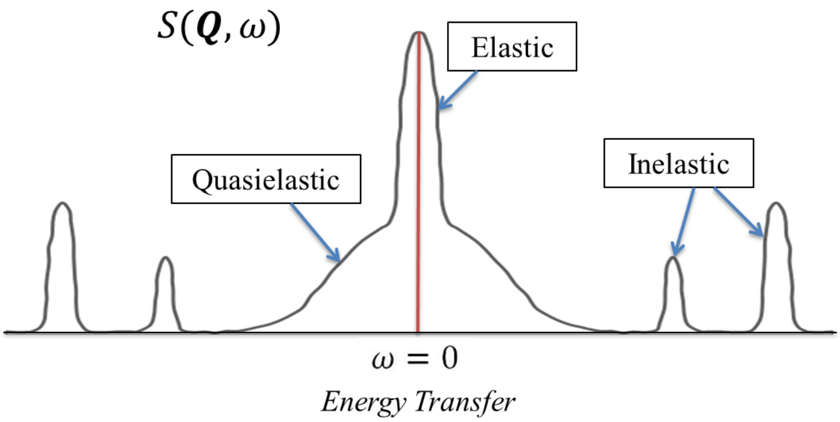

Figure A.0-1 Schematic spectrum (dynamic structure factor) showing different peaks.

Quasielastic neutron scattering (QENS) is often used in combination with MD simulation to study the properties of confined fluids because of their unique compatibility (in term of length scale and time scale) which render direct comparison and complementary explanation between experimental results and simulated observations. Explicitly, from the trajectories obtained in MD simulation, one can obtain the van Hove self-correlation function, $G_s(\boldsymbol{r}, t)$, defined as

$$G_s(\boldsymbol{r}, t) = \frac{1}{N} \langle \sum_{i=1}^{N} \delta\big(\boldsymbol{r} + \boldsymbol{r}_i(0) - \boldsymbol{r}_i(t)\big) \rangle \qquad (A.1)$$

where $\langle\,.\,\rangle$ represents an ensemble average and $\delta(\,.\,)$ is the three dimensional Dirac delta function, N is the number of particles and $\boldsymbol{r}_i$ is the position vector of particle i.

The spatial Fourier transform of $G_s(\boldsymbol{r},t)$ results in the self-part of the intermediate scattering function (ISF), $I(\boldsymbol{Q},t)$

$$I(\boldsymbol{Q},t) = FT[G_s(\boldsymbol{r},t)] = \frac{1}{N}\int_{-\infty}^{\infty}\langle\sum_{i=1}^{N}\delta(\boldsymbol{r}+\boldsymbol{r_i}(0)-\boldsymbol{r_i}(t))\rangle\exp(-i\boldsymbol{Q}.\boldsymbol{r})\,dr$$

$$= \frac{1}{N}\sum_{i=1}^{N}\langle\exp(i\boldsymbol{Q}.[\boldsymbol{r_i}(t)-\boldsymbol{r_i}(0)])\rangle \qquad \text{(A.2)}$$

where i is the imaginary number $\sqrt{-1}$, $\boldsymbol{Q} = \boldsymbol{k}_i - \boldsymbol{k}_f$ is the momentum transfer. For molecules made up from more than one atom, $I(\boldsymbol{Q},t)$ can be broken down into translational (TISF) and rotational (RISF) components

$$TISF = \frac{1}{N}\sum_{i=1}^{N}\langle\exp\left(i\boldsymbol{Q}.\left[\boldsymbol{r_{COM,i}}(t)-\boldsymbol{r_{COM,i}}(0)\right]\right)\rangle \qquad \text{(A.3)}$$

$$RISF = \frac{1}{N}\sum_{i=1}^{N}\langle\exp(i\boldsymbol{Q}.[\boldsymbol{u_i}(t)-\boldsymbol{u_i}(0)])\rangle \qquad \text{(A.4)}$$

where $\boldsymbol{r_{COM}}$ denotes the COM position of a molecule and $\boldsymbol{u}$ is the unit vector along the position vector of a selected atom in the *COM frame of reference*.

The temporal Fourier transform of ISF results in the dynamic scattering function $S(\boldsymbol{Q},\omega)$, which is directly proportional to the signal from QENS experiment

$$S(\boldsymbol{Q},\omega) = FT[\,I(\boldsymbol{Q},t)] = \frac{1}{2\pi N}\int_{-\infty}^{\infty}\sum_{i=1}^{N}\langle\exp(i\boldsymbol{Q}.[\boldsymbol{r_i}(t)-\boldsymbol{r_i}(0)])\rangle\exp(-i\omega t)\,dt$$

$$\text{(A.5)}$$

where $\hbar\omega$ represents the energy transfer with $\hbar$ being the reduced Planck constant.

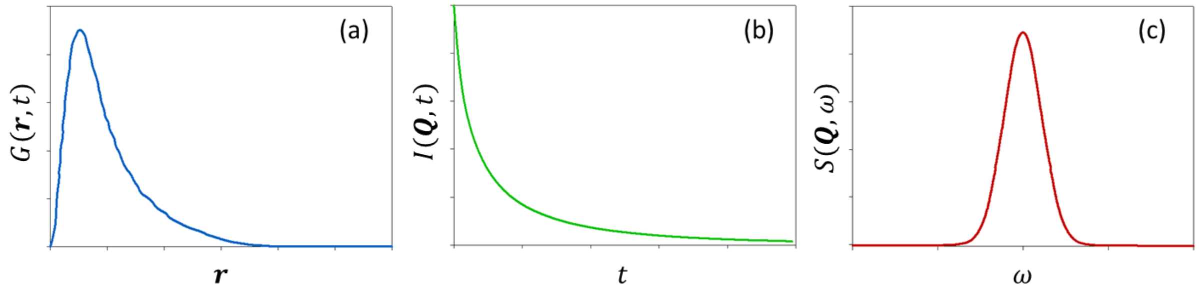

Figure A.0-2 Sample plots of (a) van Hove self-correlation function, (b) intermediate scattering function and (c) dynamic structure factor.

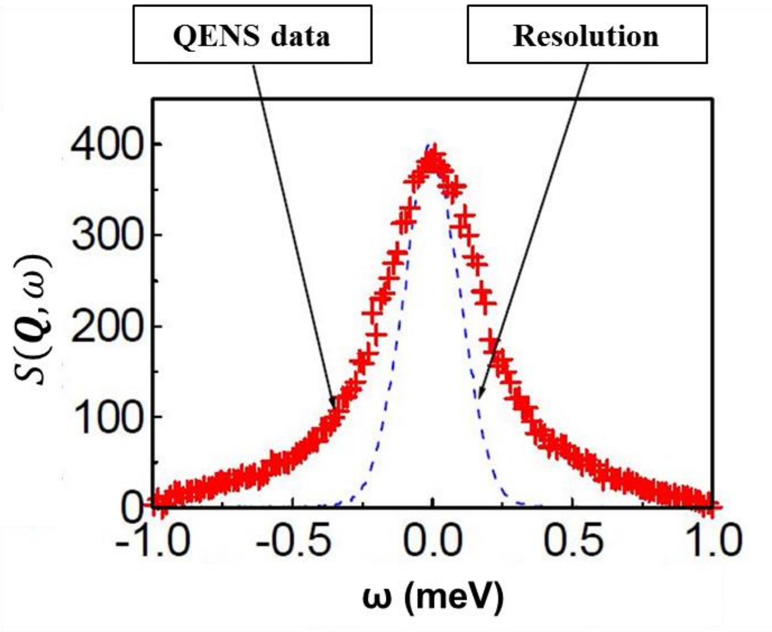

Figure A.0-3 Representative scattering signal from QENS

The dynamic scattering function obtained from a QENS experiment can be expressed as a sum of an elastic part and a quasielastic part along with a background term, convoluted with the instrumental resolution. In particular, for a QENS signal from diffusive motions, the dynamic scattering function can be written as

$$S(\boldsymbol{Q},\omega) = \{S(\boldsymbol{Q})\delta(\omega) + [1 - S(\boldsymbol{Q})]L(\Gamma,\omega) + B(\boldsymbol{Q},\omega)\} \otimes R(\boldsymbol{Q},\omega) \qquad \text{(A.6)}$$

In the above equation, the first term, $S(\boldsymbol{Q})\delta(\omega)$, has a Dirac delta function representing the elastic component. The significance of the prefactor $S(\boldsymbol{Q})$ shall be discussed shortly. In case of diffusive motion, the quasielastic term, $[1 - S(\boldsymbol{Q})]L(\Gamma,\omega)$, can be represented by a Lorentzian function $L(\Gamma,\omega)$ with Γ its half-width at half maximum (HWHM) (see **Figure A.0-4**). $B(\boldsymbol{Q},\omega)$ is the background term and may indicate noise, or other scattering contributions that have a slow energy dependence. $R(\boldsymbol{Q},\omega)$ is the instrument resolution and the symbol $\otimes$ denotes a convolution product.

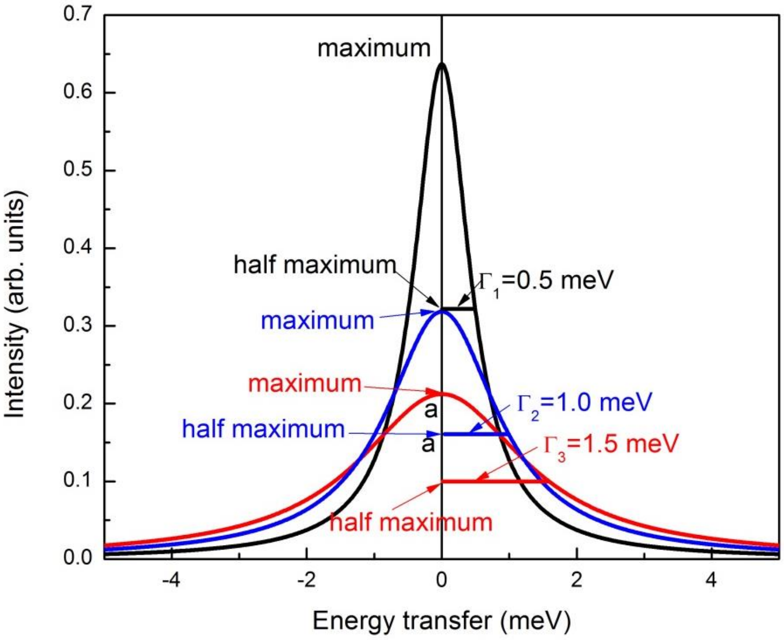

Figure A.0-4 Illustration of the HWHM of sample quasielastic spectra. Three different quasielastic spectra are shown with different colors. HWHM of the three spectra are denoted by $\boldsymbol{\Gamma_i}$ with *i*=1 (black), 2 (blue) and 3 (red) denoting the three different spectra. The black spectrum with HWHM of 0.5 meV represents small broadening in energy and thus very slow motions while the red spectrum with HWHM of 1.5 meV represents very fast motion.

Prefactor $S(\boldsymbol{Q})$ is defined as the fraction of the incoherent signal that is elastic to that of the sum of elastic and quasielastic and is therefore called elastic incoherent structure factor (EISF). It can be obtained from the QENS experiment simply as

$$S(\boldsymbol{Q}) = \frac{I_{elastic}(\boldsymbol{Q})}{I_{elastic}(\boldsymbol{Q}) + I_{quasielastic}(\boldsymbol{Q})} \tag{A.7}$$

where $I(\boldsymbol{Q})$ is the signal intensity and the subscript quasielastic and elastic stand for the two contributions. From MD simulations, it can be obtained as the long-time value of the intermediate scattering function

$$I(\boldsymbol{Q}, t \to \infty) = S(\boldsymbol{Q}) \tag{A.8}$$

In other word, EISF is identical to the long-time value of TISF and/or RISF. For fluid with unrestricted movement in at least one dimension, TISF will eventually decay to zero. However, due to the restriction inherent in the rotational motion, RISF may or may not decay to zero, depending on $\boldsymbol{Q}$ value. Explicitly, small $\boldsymbol{Q}$ corresponds to large length scale, much larger than the magnitude of the unit vector $\boldsymbol{u}$. Consequently, there is no motion observed in the system and both EISF and RISF → 1. On the contrary, large $\boldsymbol{Q}$ means small length scale used (<< $\boldsymbol{u}$ magnitude) and EISF/RISF will decay to 0. Variation of EISF with $\boldsymbol{Q}$ provides information on the geometry of motion involved. In case EISF has a finite non-zero value that is independent of $\boldsymbol{Q}$, it indicates presence of a fraction of molecules that are stationary on the time scales of interest.

The HWHM, $\Gamma(Q)$, of the Lorentzian function represents the quasielastic contribution in case of diffusive motions and it is inversely proportional to the time scale of the diffusivity. Note that a Lorentzian function is the Fourier transform pair of an exponential decay function. Therefore, if the quasielastic part of the $S(\boldsymbol{Q},\omega)$ follows a Lorentzian profile in case of diffusive motions, the corresponding ISF can be expected to have an exponential decay behaviour. By modelling the TISF obtained from the simulation with an exponential decay function, one can thus obtain the decay times which can then be directly compared with the time scales obtained from the HWHM of the Lorentzian profile of the QENS signal in the experiment.

The variation of HWHM with Q can be modelled to resolve the underlying diffusive mechanism. For bulk system following Brownian motion, HWHM is given by

$$\Gamma(Q) = D_s Q^2 \tag{A.9}$$

where $\boldsymbol{D_s}$ is the self-diffusion coefficient.

For fluids with strong enough intermolecular interactions which follow Singwi-Sjolander jump diffusion model, HWHM can be expressed as[185]

$$\Gamma(Q) = \frac{D_s Q^2}{(1 + D_s Q^2 \tau)} \tag{A.10}$$

with $D_s = \frac{l^2}{6\tau}$ where l is the jump length and τ is the residence time (Note that this residence time is different from the residence time obtained from residence autocorrelation functions obtained in the previous chapters. In fact, τ here is the time during which a typical molecule undergoing jump diffusion resides at a site before instantly jumping to another site).

Self-diffusion coefficient can also be extracted from MD simulated data. Detailed explanation is provided in section **2.4**.

The purpose of this study is to make a direct connection and comparison between MD simulations and QENS experiments carried out for pure propane in silica aerogel.[186] The main objectives are to (1) first validate the simulation results by comparing simulated values with the experimental data and then to (2) calculate quantities of interest which are inaccessible from experiments.

A.2. SIMULATION DETAILS

A.2.1. Molecular Models

The total system energy is obtained as the sum of dispersive (van der Waals), electrostatic, bond stretch, bond angle, and dihedral interactions [see equation (2.1)].

E_{VDW} and $E_{\mathrm{electrostatic}}$ are expressed by 12-6 Lennard-Jones and Coulombic potentials, respectively. Lennard-Jones parameters for non-like components were obtained using Lorentz-Berthelot mixing rules from the values of the pure compounds.[34, 187-188] Intramolecular potentials were represented by harmonic functions. The CLAYFF force field[35] was implemented to simulate the silica substrate while propane were modeled using the TraPPE-UA force field. Within this model, propane is a flexible molecule described by bond stretching, angle bending, and dihedral constraints. Methyl (CH_3) and ethyl (CH_2) groups of prpane are treated within the united-atom formalism. The hydrocarbon does not bear partial charges. All atoms on the solid silica, except for H of the surface –OH groups, remain rigid throughout the whole length of the simulations.

A.2.2. Silica Models

The silica models used in this work were obtained by cutting the β-cristobalite SiO_2 crystal along the (1 1 1) crystallographic face. A detailed description of the solid morphology was provided in **Chapter 2**. Because the experimental crystals have a pore size distribution ranging from 15-25 nm, the simulated pore width was chosen to be 20 nm and the corresponding simulation box dimensions are $4.37 \times 4.79 \times 23.3$ nm^3. Because of periodic boundary conditions, the systems are composed by silica slabs that are infinitely long along the X and Y directions, and separated along the Z direction by the slit-shaped pore. The solid substrate bears no net charge, and all the non-bridging O atoms in the solid are fully protonated, yielding a high density of surface –OH groups. **Figure A.0-5** shows sample snapshots for the simulated system at 337K and $P = 8$ bar (panel a) and $P = 58$ bar (panel b), respectively.

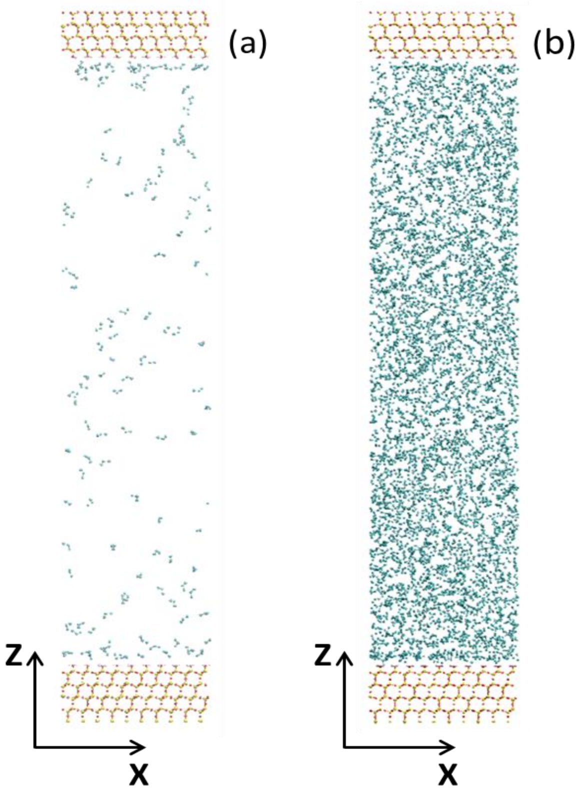

Figure A.0-5. Simulation snapshot representing a simulation box containing consists of pure propane molecules in a 20 nm silica pore at *T* = 337K and *P* = 8 bar – panel (a), and 58 bar – panel (b). The solid silica slabs are continuous along both X and Y directions. No bulk region exists. Cyan spheres are CH_2 and CH_3 groups in propane, white is H, and yellow is Si.

A.2.3. Simulation Methodology

At first, Gibbs ensemble Monte Carlo (GEMC) simulations were employed to determine the equilibrium configurations and densities of the absorbed propane phase within the silica slit pore at *T* = 337 and 365K and *P* = 8 and 58 bars, conditions which mimic experimental studies. For each simulation, 15^3 propane molecules were initially placed in a bulk phase, at a desired pressure, which is set to be in equilibrium with the pore phase consisting of empty silica pore (no confined propane). Molecular exchanges of propane between the two phases were allowed to equilibrate for 2×10^6 moves and the averages were analyzed for 1×10^6 moves. Equilibration was considered achieved based on chemical potential equality for the bulk phase and the confined phase. The potential cut-off was set at 14 Å, in accordance with the TraPPE-UA force field.[32] Tail correction method was applied for long range van der Waals interactions.

Next, molecular dynamics (MD) simulations were carried out to investigate the kinetic properties of the systems. All simulations were carried out within orthorhombic simulation boxes containing a constant number of molecules at fixed volume and constant T. T of silica and fluid were controlled separately by two Nosé-Hoover thermostats[42-43] with relaxation times of 200 fs each. Corrections for long-range electrostatic interactions were taken into account by the particle-mesh Ewald summation.[44] The cutoff distance for all interactions was set at 14 Å. The simulations were conducted using the Groningen Machine for Chemical Simulations (GROMACS) simulation package, version 5.0.4.[4-5] The leapfrog algorithm[40] with time steps of 1 fs was implemented. Simulations were conducted for 5 ns for all systems investigated, with their initial configurations taken from the previous corresponding GEMC studies. Data analysis was carried out over the next 2 ns of each simulation.

It is important to emphasize that, as in the experiments, the amount of propane at an initial pressure was kept constant while the temperature was raised from 337K to 365K in isolated chamber (i.e., the number of propane molecule does not changes). Accordingly, 2 simulations were initially carried out corresponding to a starting propane density at 337K and P = 8 or 58 bars. Then, the temperature was raised to 365K for the 2 systems described above, thus keeping the number of propane molecules constant. The section below discusses (1) the validation of these simulated results by comparing them with the experimental data and (2) further calculation of other quantities.

A.3. RESULTS

A.3.1. Comparison with the Experiment

In QENS experiments, individual spectra were modelled using Lorentzian function with the corresponding HWHM, Γ, showing a monotonic behaviour with wave-vector transfer ($\boldsymbol{Q}$). Moreover, the EISF obtained from the individual spectra showed no systematic variation, implying absence of a contribution from localized motion to the spectra. Therefore, the QENS spectra only contained information from translational diffusion motion of propane molecules.

In order to make comparison with the experimental data, TISF were calculated from propane molecules COM trajectories, obtained from MD simulations. Recall that intermediate scattering functions $I(\boldsymbol{Q},t)$ are the inverse Fourier transforms of scattering law $S(\boldsymbol{Q},\omega)$ that is measured from the QENS experiment. Thus, the spectra in the experiment on propane in silica aerogel should be proportional to the Fourier transform of the TISFs calculated here. Moreover, if the experimental spectra could be modelled by a Lorentzian function, the corresponding TISFs should be describable by an exponential decay function, since a Lorentzian and an exponential decay function form a Fourier transform pair. With this expectation, the TISFs were modelled using an exponential as a component. These modelling attempts and some results are described in the following sections.

A.3.2. Translational Motion and TISF

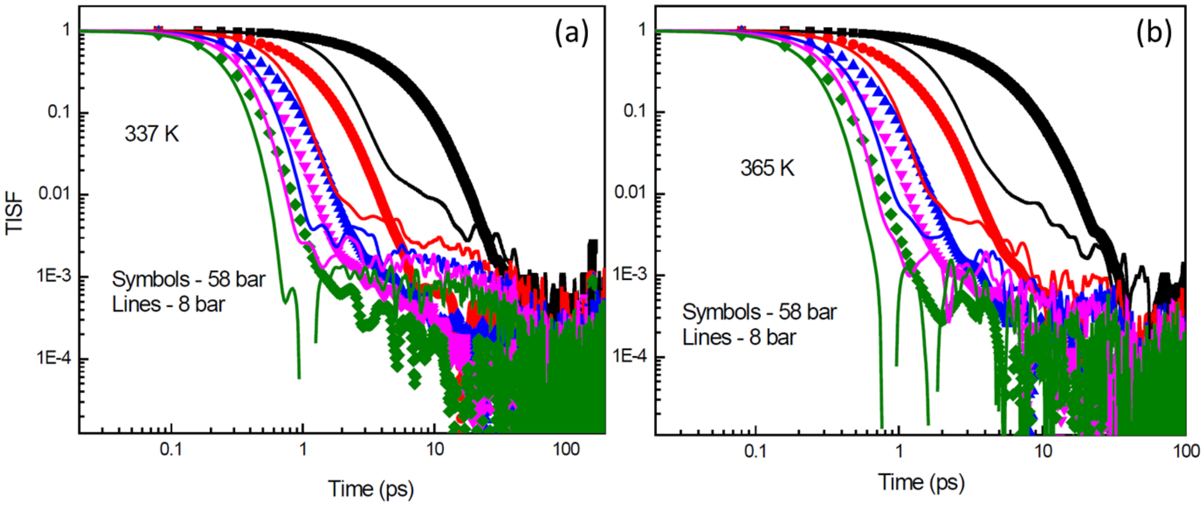

Figure A.0-6 TISFs for different *T* and *P* at ***Q*** values between 0.3 (black) and 1.8 Å^{-1} (olive).

Figure A.0-6 shows the TISFs calculated for the 4 sets of simulation data. The TISFs have complex behaviour. In general, three different regimes could be identified – very short time regime (sub-picosecond, i.e., very fast decay of TISF), intermediate time regime (few tens of picoseconds, i.e., slower decay of TISF) and long time regime (hundreds of picoseconds, where the TISFs have almost decayed to ‘0’). Based on this, a combination of a Gaussian with two exponential decay functions to model the TISFs across the entire time range was made. The Gaussian was chosen for short times, as it would represent free particle motion before a typical molecule collides with the neighbouring molecules. Although the fits were visibly of good enough quality, this modelling approach suffers from an inherent limitation of the data. These fits gave a good estimate of the Gaussian component as it represented the region with largest TISF values. By the time exponential decay takes over the TISF description, these functions have already decayed to very low values (<0.001, for most ***Q*** values). In other words, the fitting program would attach very little weightage to this region and the exponential decay components would not be estimated with enough accuracy. An attempt to use three exponentials gave similar results with only the very short time exponential being estimated accurately. An attempt was also made by smoothening the functions by skipping time frames, resulting in less number of data points and hence slightly smoother functions. However, no significant improvement could be made with these fitting. The problem is akin to measuring a very small quantity in presence of a very large one. One possible solution is to remove the large quantity portion. Thus, a final attempt was made to model *only the intermediate time scale* of the TISFs.

Note that the QENS experiment was carried out at a backscattering spectrometer that could measure energy transfers between 3.5 to 200 μeV, corresponding to a time scale range of a few tens of picoseconds. Therefore, it was decided to model only the intermediate regime of the TISFs that corresponds with this time scale with a single exponential decay function. A time interval of 0.2 ps was used. This attempt resulted in good agreement between the experiments and the simulations (see **Figure A.0-7** and **Figure A.0-8**). The decay constants of the exponential decay functions were converted to the energy scale and were directly comparable with Γ obtained from the experiments. In conclusion, at higher pressures, the motion is faster.

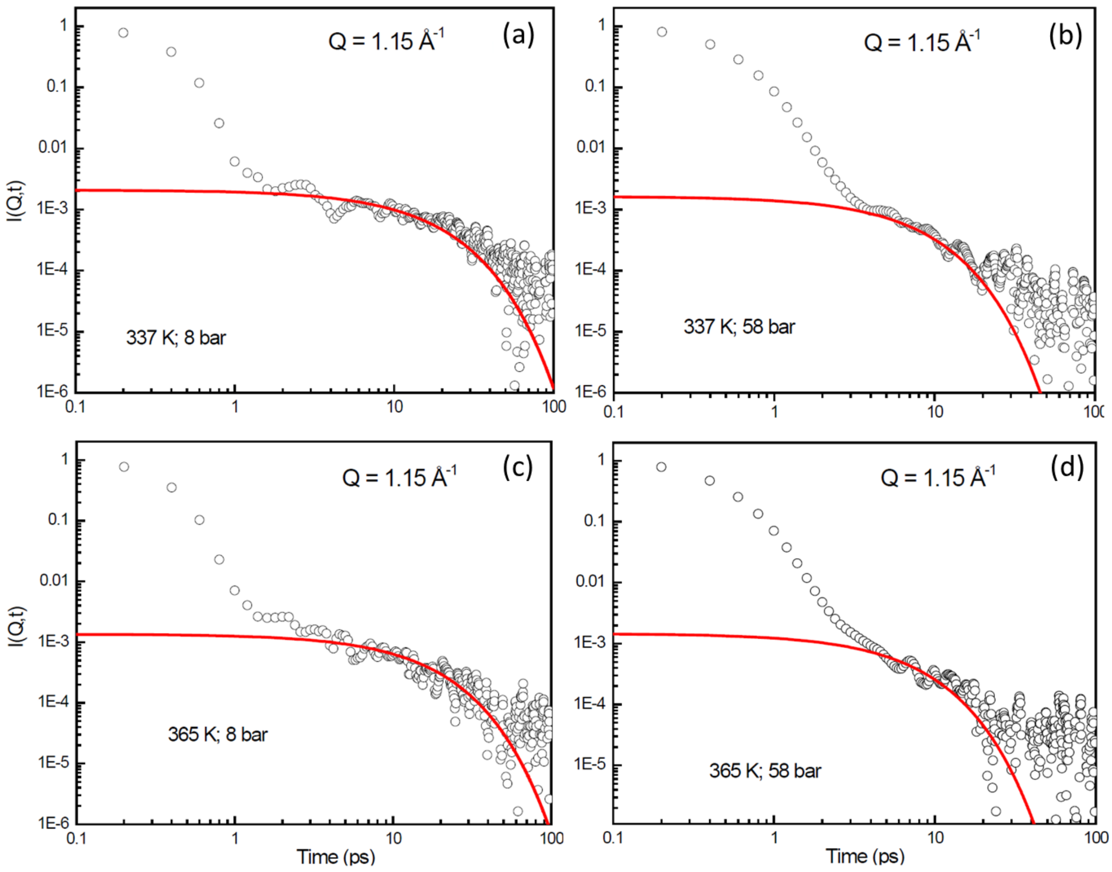

Figure A.0-7. Fits of the intermediate time range of TISFs at a ***Q*** value of 1.15 Å^{-1} with exponential decay function (red line). At this Q value, the long-time behaviour of TISFs starts at around 40 ps.

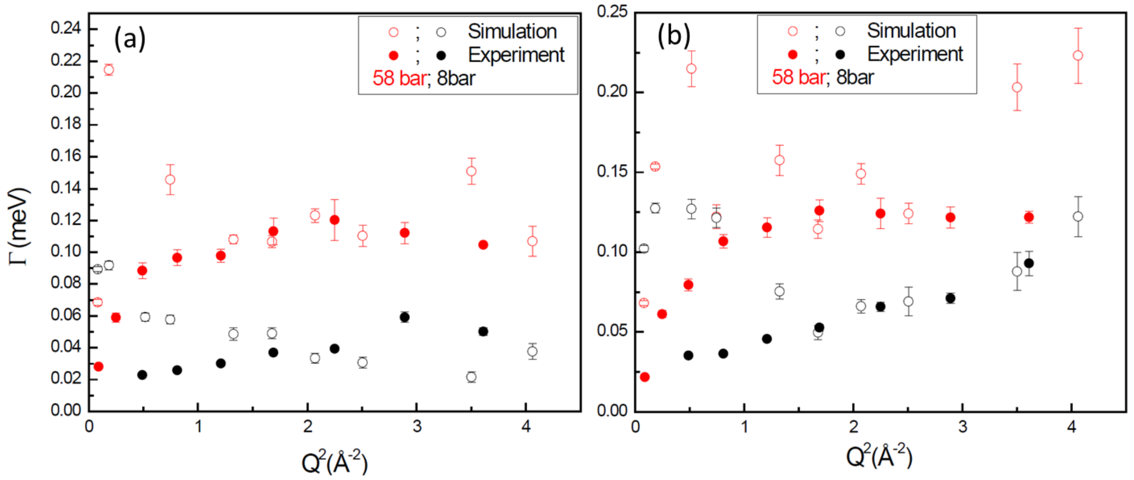

Figure A.0-8. Comparison of the decay constants of model exponential decay functions (converted to energy scale) from the simulation (open symbols) with the Γ values (solid symbols) obtained from fitting of the experimental spectra. Red symbols denote the high pressure data at 58 bar while the black symbols stand for the low pressure data at 8 bar. Left panel shows the comparison for 337K and the right panel for 365K.

A.3.3. MSD and Diffusivity

In addition to the TISFs, information about the overall translational motion can be obtained by studying the variation of MSD with time, as seen in **Figure A.0-9**. The MSD at lower pressure is an order of magnitude higher than that at higher pressure. The variation in temperature however is very mild as compared to that in pressure. (Recall that the density of propane in the pore was kept constant while changing the temperature in order to make comparison with the experiment.) Moreover, this variation in temperature is even more suppressed at higher pressure. This could be an effect of a crowded environment at higher pressure. Another interesting feature that can be observed in a log-log plot of MSD is the extent of ballistic motion. The initial short time ballistic motion, where a molecule moves free from collisions extends up to about 30 ps at lower pressures. At higher pressure, it remains in only a short duration of less than 1 ps. This is also a consequence of the crowding effect, as higher number of neighbouring molecules makes intermolecular collisions easier and more frequent. From MSD values, propane mean free path was estimated to be around 10 nm at low pressures and about 0.3 nm at high pressure. Thus at high pressure, propane can be said to be a viscous fluid while at low pressure it is close to transition between a viscous fluid and a Knudsen fluid. (Note that for viscous fluid, the mean free path is much smaller than the confinement dimension; the opposition is true for Knudsen fluid).

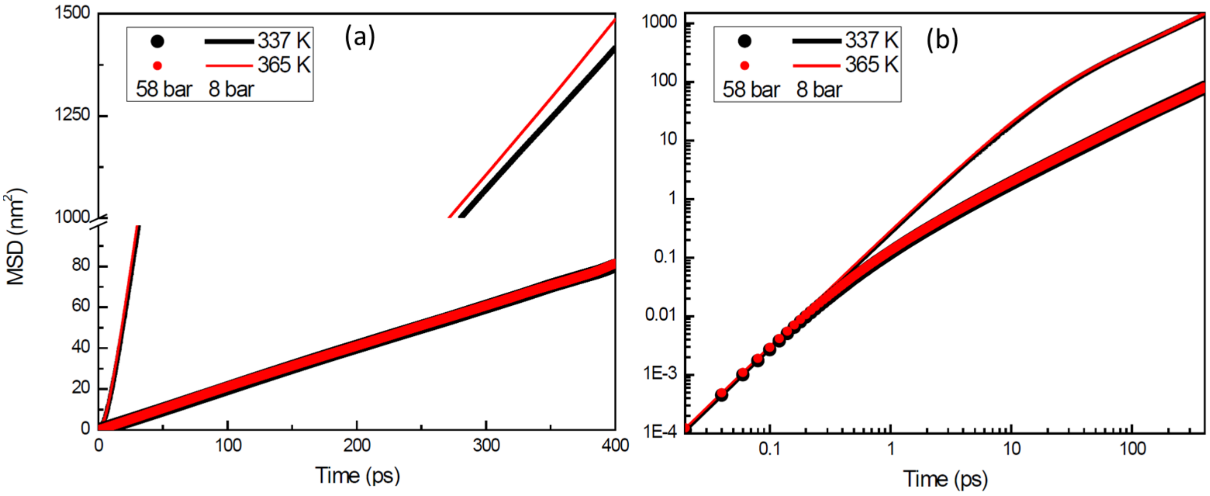

Figure A.0-9. MSD curves for 337K (black) and 365K (red) simulations. Lines correspond to the lower pressure of 8 bar whereas symbols represent the higher pressure of 58 bar at either temperature. The left panel (a) is in linear scale while the right panel (b) shows the same quantities in log-log scale. Notice a break in the vertical scale on the left plot.

A.3.4. Molecular Distribution Corroborates Experimental Findings

From the QENS experiments, it was found that propane diffusivity increases as the system pressure increases. Although the overall simulated MSD shows contradictory behaviour, the intermediate time scale behaviour of TISFs is consistent with experimental observation. Possible explanation is as follow. At low pressure, most of propane molecules were adsorbed to the pore walls and hence immobile due to strong interaction with the silica substrates. At higher pressure, more propane molecules occupied the central region of the pore, free from the wall adsorption, and more mobile, thus enhancing the overall diffusivity. Such conclusion can be obtained from the density profiles of propane at different pressures, as seen in **Figure A.0-10**. At low pressure, a larger fraction of propane molecules lies close to the walls and are very slow due to strong interaction with the pore substrate. Thus, they contribute little to the diffusivity. At higher pressure, the fraction of molecules close to the wall is relatively smaller and consequently the number of fast mobile molecules is larger. This enhances the diffusivity at high pressure. At the two pressures, the variation in the fraction of molecules occupying different regions is smaller than the variation between the two pressures. Moreover, this variation gets further diminished at higher pressure. At low pressures, the extra kinetic energy provided to the system in the form of a raised temperature helps some molecules adsorbed on the pore surface overcome the strong surface interactions and move away from the pore wall. This results in the fraction of molecules residing close to the pore wall decreasing with temperature. At higher pressure the difference in temperatures is smaller due to a large total number of molecules.

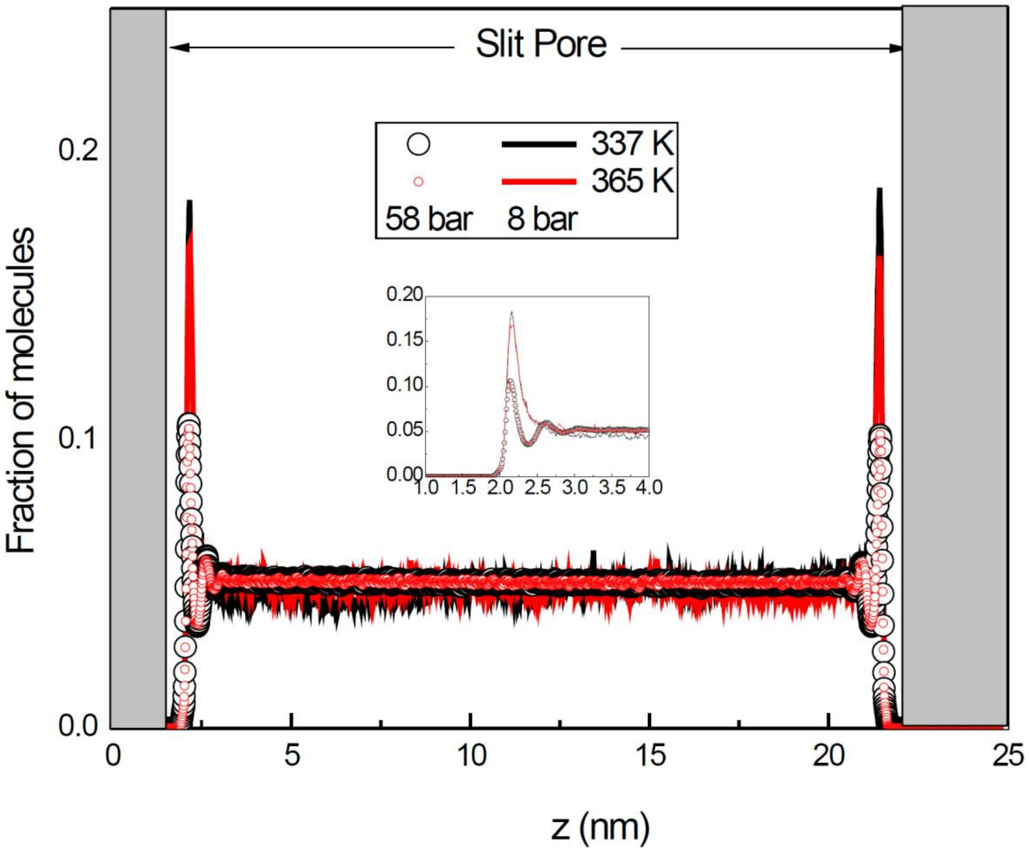

Figure A.0-10. Fraction of total number of molecules occupying the pore. The pore space is the space between two grey regions marked in the plot. Lines correspond to the lower pressure data (8 bar) whereas the symbols denote higher pressure data (58 bar).

A.3.5. Rotational Motion and RISF

Rotational motion of propane molecules was probed by following the evolution of a unit vector (***u***) attached to the position vector of CH$_3$ site in the molecular frame of reference which has its origin at the COM of the molecule. In particular, first, the orientational correlation functions (OCFs) of order 1 and 2 were calculated. (Note that OCF of order *l* is $<P_il[(\boldsymbol{u}(t).\boldsymbol{u}(0)]>$ where $P_il[\boldsymbol{x}]$ is Legendre polynomial of order *l* of specie *i*). The first of these functions is the dipole correlation function. **Figure A.0-11** shows the OCFs for all simulations studied. As in the case of translational motion, the variation of OCFs in pressure is dominant over the variation in temperature. Moreover, the difference in the OCFs for two pressures is not only quantitative but also qualitative. It can be seen that the first order OCF at low pressures shows a conspicuous negative dip. This is a signature of a rotational motion characterized by large angular jumps. The time scales of rotational motion can be obtained by integrating the OCFs up to times long enough for these functions to decay zero. The OCFs were integrated up to 40 ps to obtain the time scales from OCFs of order 1 and 2. These time scales are tabulated in **Table A.0.1** below. The rotational motion gets faster at higher pressures. Similar enhancement of rotational motion on increase in loading has been observed for ethane and propane in ZSM5 both in simulations[189] as well as in experiments,[190] as also for propane in TiO_2.[191] Also listed in **Table A.0.1** are the ratios of the two time scales, $\boldsymbol{\tau_1/\tau_2}$. Debye model for Brownian rotational motion (in which there is a random change in the orientation of a polar molecule due to collisions with other molecules) predicts that $\boldsymbol{\tau_1}$ decays 3 times faster than $\boldsymbol{\tau_2}$. In our MD simulations, however, $\boldsymbol{\tau_1/\tau_2}$ ratios are all less than 2. The lower the pressure and temperature, the smaller the $\boldsymbol{\tau_1/\tau_2}$ ratios. The time scales obtained in this study have the same order of magnitude as those obtained for propane in 4 nm cylindrical pores of TiO_2.[190-191]

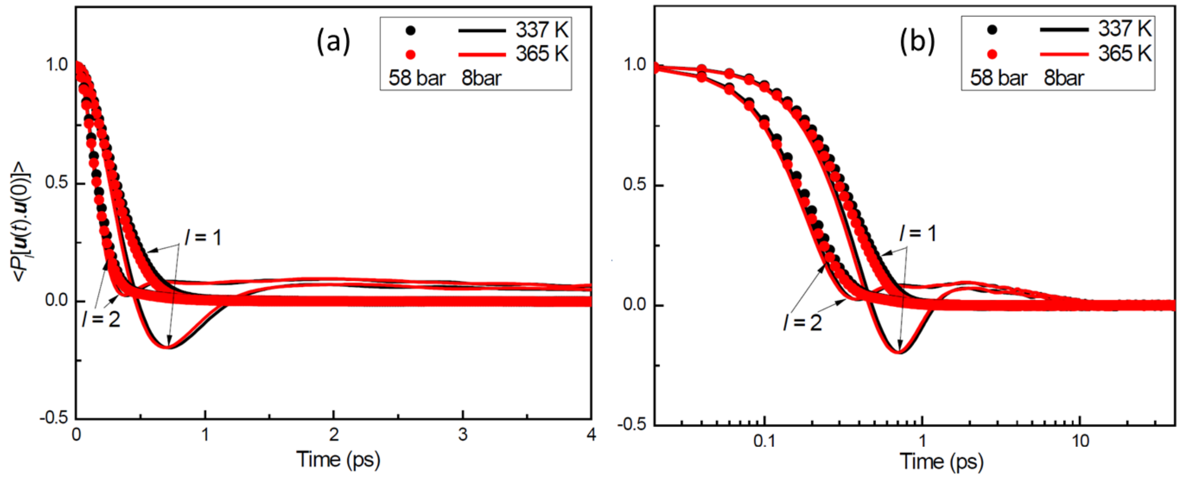

Figure A.0-11. OCFs calculated at different temperatures and pressures. The left panel (a) is in linear scale while the right panel (b) shows the same quantities in log-log scale.

Table A.0.1. Time scales of rotational motion.

Pressure (bar)	**Temperature (K)**	**τ_1 (ps)**	**τ_2 (ps)**	**τ_1/τ_2**
8	337	0.631	0.818	0.7714
	365	0.635	0.813	0.7811
58	337	0.335	0.203	1.6502
	365	0.33	0.19	1.7368

The RISF corresponding to several ***Q*** values were also calculated. Results are shown in **Figure A.0-12**. The overall qualitative information content in these functions is similar to that in the OCFs. However, these functions can provide additional information on the geometry of rotational motion by their long time behaviour. This long time behaviour of the RISFs is identical to the EISF. The variation of EISF with ***Q*** can reveal the geometry of motion. **Figure A.0-12** shows that the differences in RISFs for all cases are limited to very short time periods, up to 20 ps. Thereafter, RISF for a given ***Q*** value for different *T* and *P* conditions converge to the same EISF values and hence, the geometry of rotational motion remains unchanged between different *T* and *P* conditions.

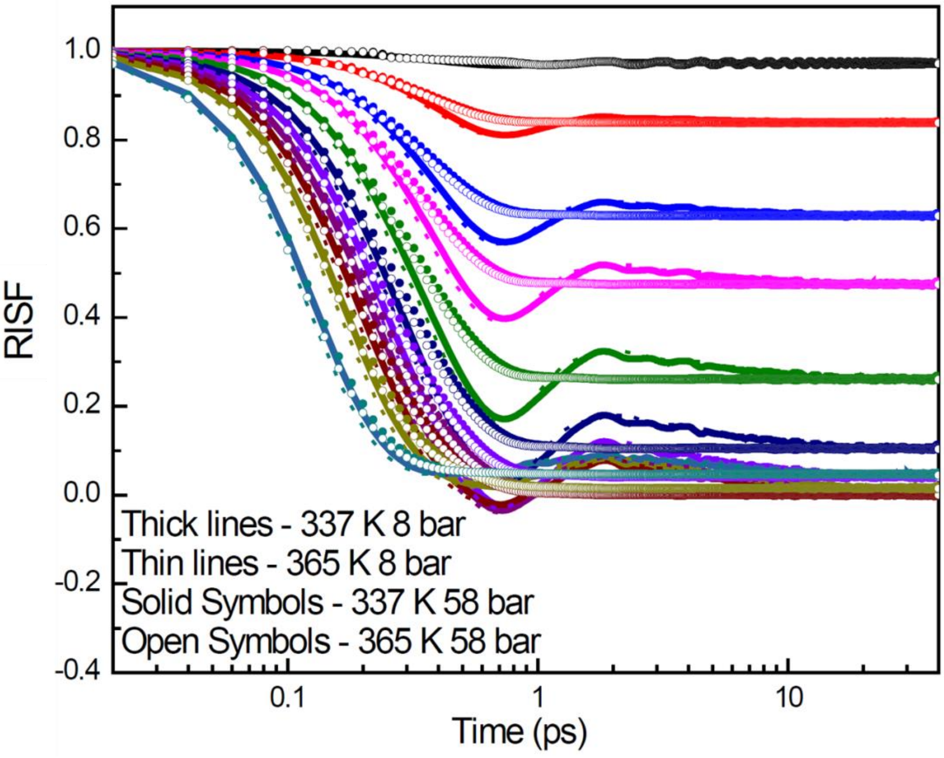

Figure A.0-12. RISFs for different temperatures and pressures for ***Q*** values between 0.29 and 4.6 Å^{-1} (top to bottom at 0.1 ps).

Figure A.0-13 shows the variation of EISF as function of ***Q***. EISF for a unit vector undergoing isotropic rotational diffusion was also modelled and calculated. Good agreement was obtained between the two set of data. This result is within expectation, as the propane molecules do not exhibit any preference for a particular orientation.

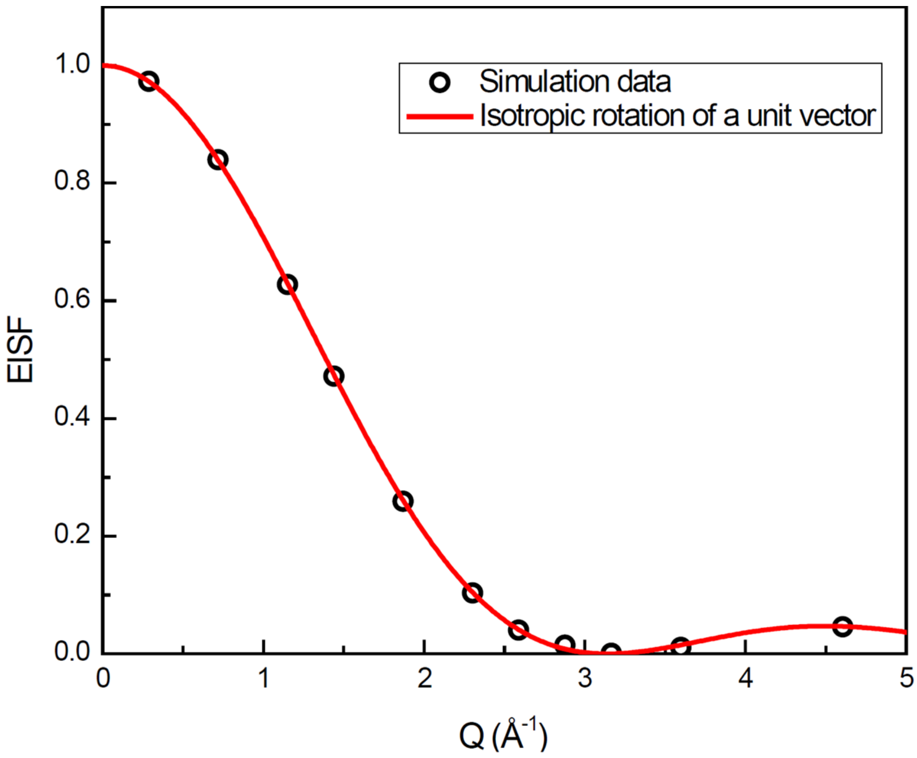

Figure A.0-13. EISF obtained from the long time values of RISFs from the simulation (symbols). Solid red line is the calculated EISF variation for a unit vector undergoing isotropic rotational diffusion.

A.3.6. Properties in Different Regions

In this section, the results are differentiated and discussed for the properties of propane molecules in two regions – Region 1 consists of *two* propane first adsorbed layers close to *either* of pore walls parallel to each other; and Region 2 is the rest of the pore.

Sample trajectories of the COM of 5 randomly chosen propane are shown in **Figure A.0-14** for the two systems of 8 bar and 58 bar at 337K. Panel (a) reflects the behaviour of the fluid at low pressure, where a typical molecule is more likely to traverse the whole pore, shuttling back and forth between the two opposite pore walls. On the other hand, panel (b) shows that at higher pressure, a typical molecule remains confined in a narrow portion of the pore and seldom approaches both the opposite pore walls during the whole simulation time of 1 ns. Such result is obtained because of a larger number of molecules at higher pressure, i.e., the crowding effect.

Next, we identified 5 molecules that remain within Region 1 continuously for at least 50 ps. Similarly, 5 molecules spending at least 50 ps continuously in Region 2 were identified. The latter is easier because of the large geometric size of Region 2. Refer to the green ellipses in **Figure A.0-14** for sample trajectories of an individual molecule which stayed in Region 1 for the time interval required at different loading. Because the effect of pressure dominates the effects of temperature, only the study of simulations at 337K is presented for the sake of brevity.

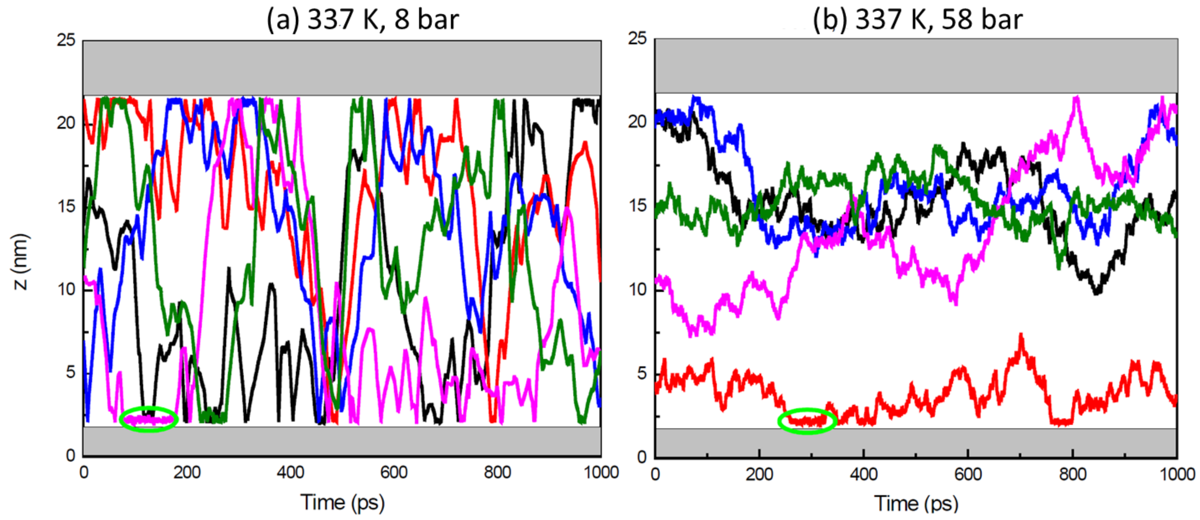

Figure A.0-14. Trajectories in the Z-direction of the COM of 5 randomly chosen propane molecules at 337K and (a) 8 bar and (b) 58 bar. The SiO_2 slabs making the slit pore are represented by grey rectangles. Periods of continuous stay of a representative molecule close to the pore wall are highlighted by green ellipses (t ~ 100 - 150 ps for the low pressure and 270 – 320 ps for the high pressure).

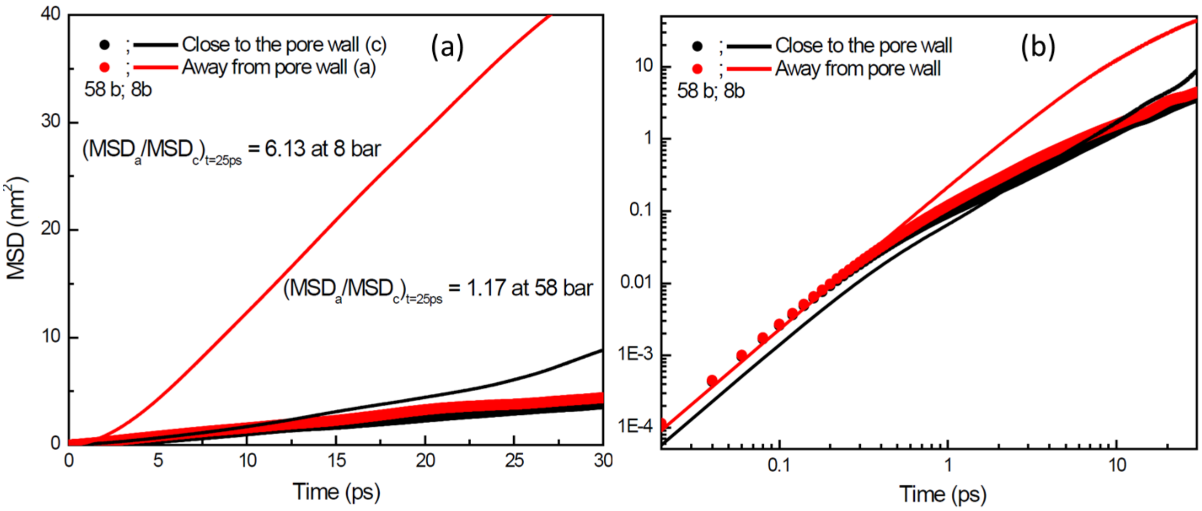

Figure A.0-15. MSD for the COM of 5 representative propane molecules close to (black) and away from (red) the pore wall for the two pressures at 337K. The higher pressure data are denoted by symbols whereas the lines denote the low pressure data. The left panel (a) is in linear scale while the right panel (b) shows the same quantities in log-log scale.

MSD calculated for the molecules in different regions are presented in **Figure A.0-15**. Results show that even the molecules that are close to the pore wall have higher displacements at low pressure compared to that at high pressure. Again, this is due to the crowding a typical molecule would encounter at higher pressure. At low pressure, the fluid-fluid interactions are weaker than the fluid-surface interactions close to the pore wall. Consequently, propane molecules close to the pore wall get considerably slowed down. At higher pressure, a larger number of fluid molecules results in a stronger total fluid-fluid interaction and so the difference in the mobility of propane molecules close to the pore wall and away from it gets suppressed.

Another interesting result obtained is the duration of ballistic regime. For the higher pressure data, as fluid-fluid collisions become equally likely, as fluid-surface collisions the ballistic regime extends to the same amount of time for molecules close to and away from the pore wall. At lower pressure though, as the fluid-fluid collisions are less likely to occur in the pore centre than the fluid-surface collisions are close to the surface, the ballistic regime lasts longer for molecules away from the surface. However, for molecules close to the pore surface, the ballistic regime lasts only as long as it does for higher pressure.

The difference in the motions of propane in the two regions is also reflected in the behaviours of the TISFs, as seen in **Figure A.0-16** below.

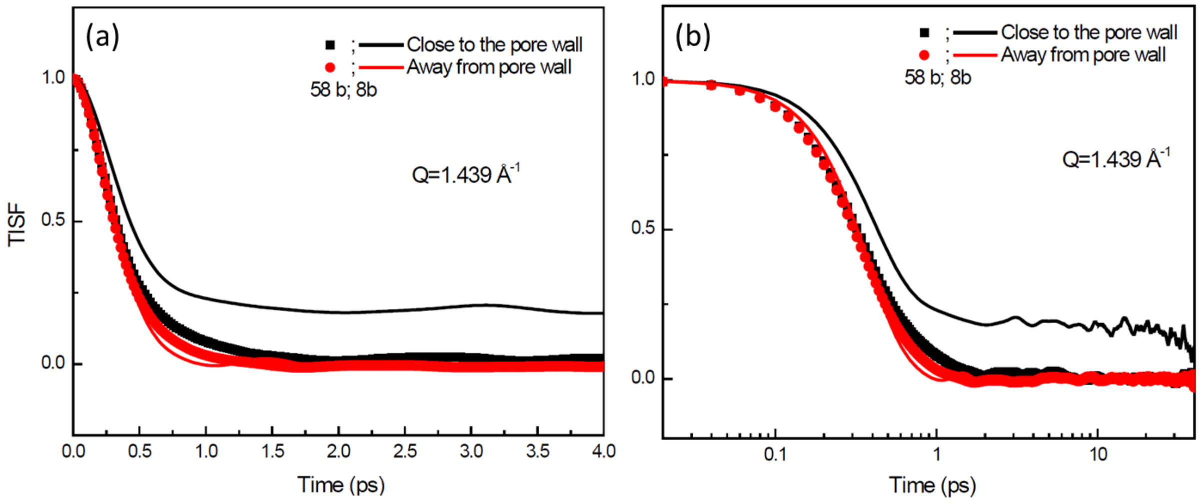

Figure A.0-16. TISF of 5 representative propane molecules close to (black) and away from (red) the pore wall for the two pressures at 337K. The higher pressure data are denoted by symbols whereas the lines denote the low pressure data. The left panel (a) is in linear scale while the right panel (b) shows the same quantities in log-log scale.

A.3.7. Orientational Structure and Dynamics in Different Regions

The orientational distributions of propane molecules in the two regions were calculated. Because this distribution is a static property, it was possible to calculate this function for all molecules that occupy the two regions at any instant. Hence, the results are statistically more accurate than those obtained with just 5 molecules. **Figure A.0-17** shows the distribution of the orientation of a CH_3 site in the molecular frame of reference with respect to the three Cartesian directions. For reference, the distribution function expected when there is no orientational ordering (or the distribution is isotropic) is also shown with a thick dark yellow line. The distribution is statistically more accurate for higher pressure because of a larger number of molecules. Furthermore, it can be seen that in Region 2, the distribution is isotropic whereas, there seems to be a tendency towards orientational ordering for molecules close to the pore wall in Region 1. This is evident as the distribution with respect to Z-direction gets sharper at right angle of 90° and those with respect to the X and Y-direction get suppressed at 90°. In other words, closer to the pore wall, propane molecules have a slight preferential orientation so that the CH_3-CH_2 bond (which is close to the position vector of CH_3 in the molecular frame of reference) is aligned parallel to the pore surface. This preference is, however, quite weak as would be expected for a non-polar molecule like propane.

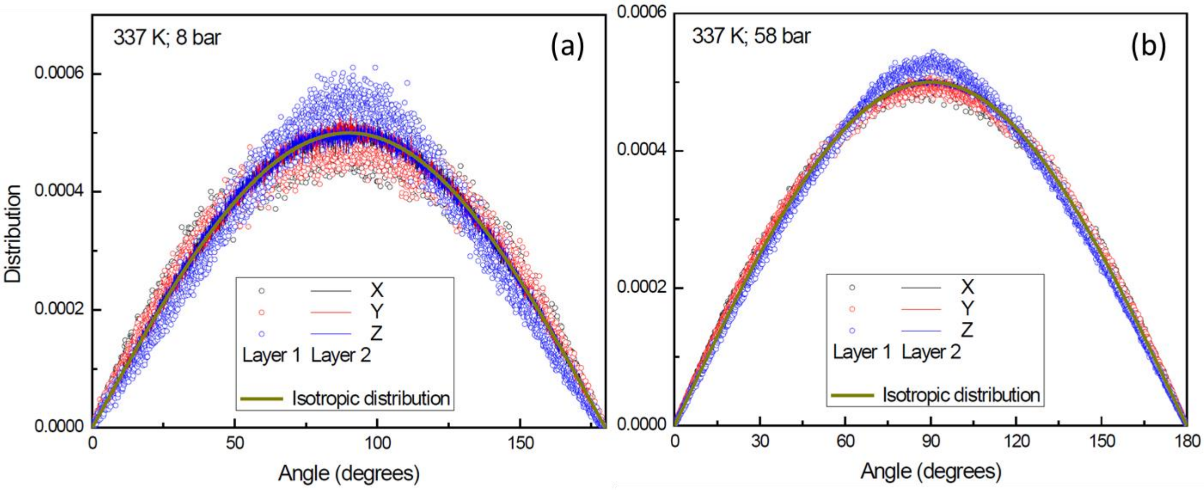

Figure A.0-17. Orientational distribution of CH_3 position vector in the molecular frame of reference with respect to the Cartesian directions X (black), Y (red) and Z (blue) at 337K and (a) 8 bar and (b) 58 bar. Symbols denote the distribution for molecules in Region 1 and lines are those in Region 2. For reference the expected curve for an ideal isotropic distribution is shown as a thick dark yellow line.

The orientational (or rotational) dynamics of propane molecules in the two regions was probed using the OCFs and RISFs. Unlike COM motion, the rotational motion exhibits a qualitative change between the two regions, especially at low pressure. **Figure A.0-18** shows the OCFs of the order 1 and 2. At low pressure, shown in panel (a) and (b), significant differences can be seen between the Region 1 and 2. This is evident in the first order OCFs that show a conspicuous negative minimum for Region 2, a signature of large angle turns. In fact, the first order OCF can be seen to represent the average value of the angular displacement and the first minimum in these functions can thus represent a measure of maximum angular displacement before a turnaround occurs. This angle is found to be 101° for Region 2 and 86° for Region 1. The overall behaviour of the OCFs follow the OCF behaviour for Region 2 as this region is larger in size and hence, weight. A slower decay of the OCF in Region 1 signifies a slower rotation, as expected, due to the attractive fluid-surface interactions. At higher pressure, shown in panel (c) and (d), neither of the two regions exhibit long angle jumps; however, the rotation in Region 1 is slower at high pressure, similar to that at low pressure.

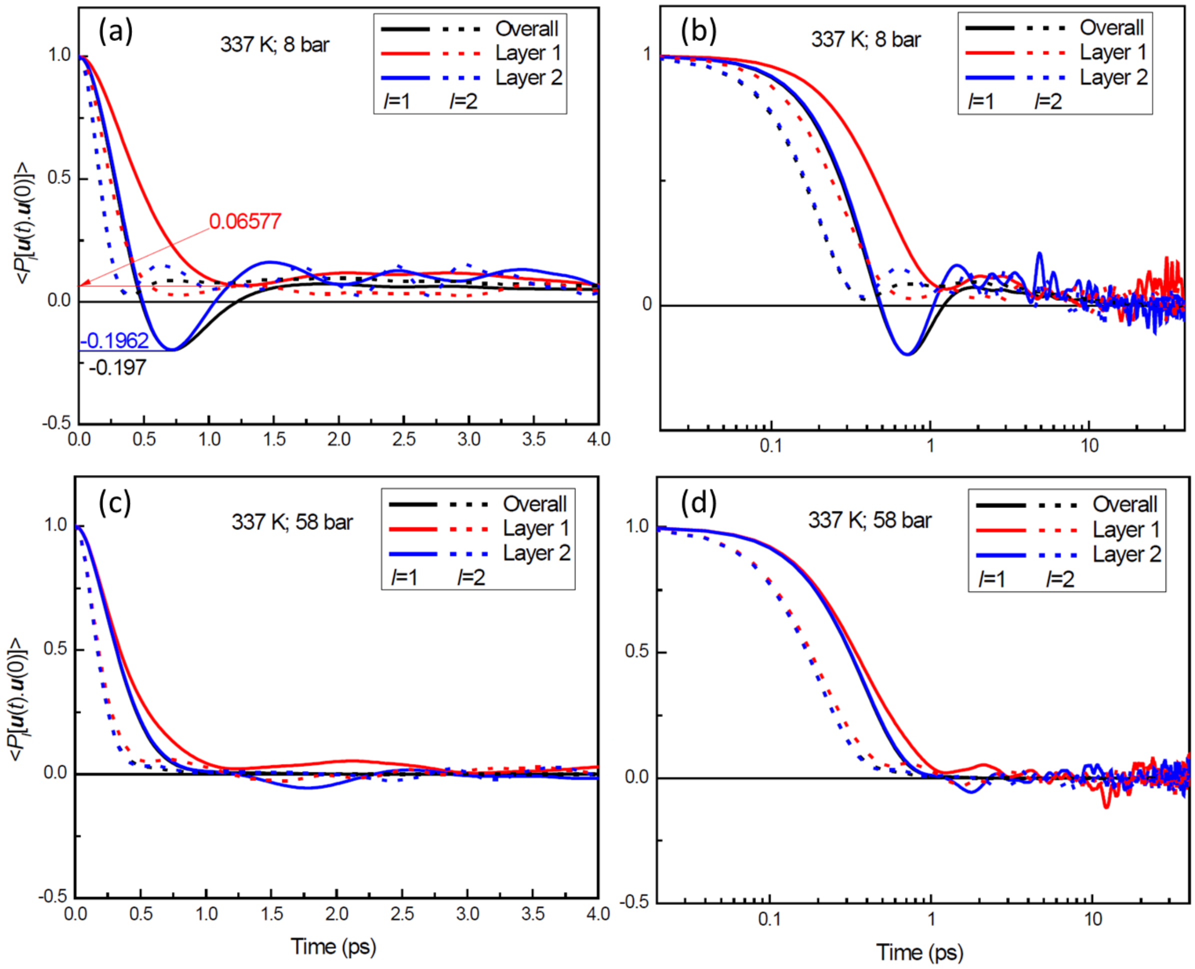

Figure A.0-18. Orientational Correlation Functions in different regions at 337K for two pressures. The first order functions are shown as solid lines whereas the dotted lines represent the second order OCFs. The left panel (a) is in linear scale while the right panel (b) shows the same quantities in log-log scale

The RISFs calculated for the different regions are shown in **Figure A.0-19**. Similar behavioural changes can be observed as in the case of OCFs. Even though for lower pressure the RISFs for the two regions are not calculated for times long enough to have a stable value, it can be seen that beyond 10 ps, the RISFs for different regions become identical within statistical uncertainties, see panel (a). This is also true for the RISFs at high pressure in panel (b). Thus, there is no change in the EISF values as the pressure or the location of propane molecules changed. Therefore, the geometry of rotational motion remains unchanged for all the simulations in all regions within the pore. This result is as expected, since no significant orientational ordering is observed from the orientational distribution function for any simulations (see **Figure A.0-17**). The only change in rotational motion is the change in the speed of rotation and the extent of the angular jumps.

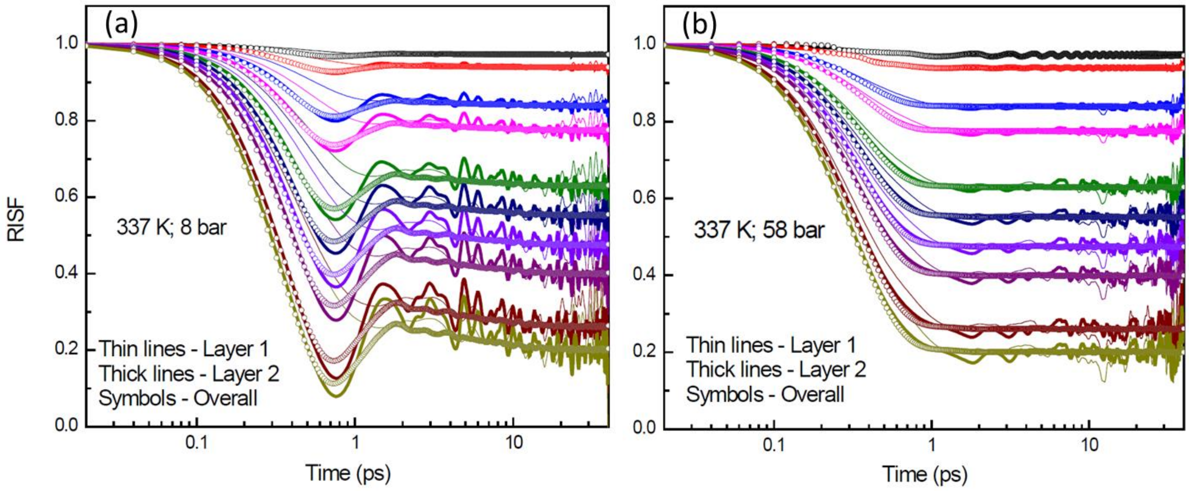

Figure A.0-19. RISFs corresponding to different ***Q*** values (different colors) between 0.29 and 2.01 Å^{-1} for Region 1 (thin lines), Region 2 (thick lines) and overall (symbols). The RISFs exhibit similar behavioural change as the OCFs.

A.4. CONCLUSIONS

Molecular dynamics simulations in combination with quasielastic neutron scattering experiments were used to study dynamic properties of propane confined in nanoporous silica as functions of temperature and pressure. The effects of pressure were found to dominate the effects of temperature. The time scales obtained from the intermediate scattering functions from MD simulations agree well with the time scaled obtained in the experiment. Although the MSD curves are in contrast with the experimental finding of an enhanced diffusion at higher pressures, it is corroborated with the time scales obtained from TISFs. It is worth mentioning that while MSD curves give a length scale averaged contribution to diffusivity, the TISFs take into account motion at different length scales by the virtue of their Q dependence. This difference in MSD and TISFs might help explain the discrepancy observed in the pressure dependence of time scales obtained from these quantities.

A larger fraction of propane molecules residing close to the pore wall at low pressure explains the enhancement of diffusivity at high pressure. Overall motion of molecules close to the pore wall is slower than the rest of the molecules. This motion of molecules close to the pore wall at low pressure however, is faster than the motion of molecules away from the pore wall at high pressure. This is because of a highly crowded environment at high pressure. Results also show that the rotational motion of propane molecules is isotropic at all temperatures and pressures, as also in all the regions of the pore. Rotational motion shows a slight enhancement at higher loading similar to findings elsewhere. Lastly, there is a slight tendency towards orientational ordering o propane molecules close to the pore wall, while no such orientational ordering exists for overall system.

List of Publication

Le, T.; Striolo, A.; Cole, D. R. Propane Simulated in Silica Pores: Adsorption Isotherms, Molecular Structure, and Mobility. *Chem. Eng. Sci.* **2015**, *121*, 292-299

Le, T.; Striolo, A.; Cole, D. R. CO_2–C_4H_{10} Mixtures Simulated in Silica Slit Pores: Relation between Structure and Dynamics. *J. Phys Chem. C* **2015**, *119*, 15274-15284

Le, T.; Ogbe, S.; Striolo, A.; Cole, D. R. N-Octane Diffusivity Enhancement via Carbon Dioxide in Silica Slit-Shaped NanoPores – A Molecular Dynamics Simulation. *Mol. Simul.* **2015**, *121*, 1-8

Le, T.; Striolo, A.; Turner, C.H.; Cole, D. R. Confinement Effects on Carbon Dioxide Methanation: A Novel Mechanism for Abiotic Methane Formation. [Submitted]

Gautam, S.; **Le, T.**; Striolo, A.; Cole, D. R. Molecular Dynamics Simulations of Propane in Nanoslit Silica Pore: Direct Comparison with Quasielastic Neutron Scattering Experiment. [In preparation]

Bibliography

(1) Dillon, E. C.; Wilton, J. H.; Barlow, J. C.; Watson, W. A. Large Surface Area Activated Charcoal and the Inhibition of Aspirin Absorption. *Annals of Emergency Medicine* **1989**, *18*, 547-552.

(2) Du, X.; Wu, E. Porosity of Microporous Zeolites a, X and ZSM-5 Studied by Small Angle X-Ray Scattering and Nitrogen Adsorption. *J. Phy. Chem. Solids* **2007**, *68*, 1692-1699.

(3) McNaught , A. D.; Wilkinson, A. *IUPAC. Compendium of Chemical Terminology*, 2nd ed.; Blackwell Scientific Publications: Oxford, 1997.

(4) Hess, B.; Kutzner, C.; van der Spoel, D.; Lindahl, E. Gromacs 4: Algorithms for Highly Efficient, Load-Balanced, and Scalable Molecular Simulation. *J. Chem. Theory Comput.* **2008**, *4*, 435-447.

(5) Van Der Spoel, D.; Lindahl, E.; Hess, B.; Groenhof, G.; Mark, A. E.; Berendsen, H. J. C. Gromacs: Fast, Flexible, and Free. *J. Comput. Chem.* **2005**, *26*, 1701-1718.

(6) Gruszkiewicz, M. S.; Rother, G.; Wesolowski, D. J.; Cole, D. R.; Wallacher, D. Direct Measurements of Pore Fluid Density by Vibrating Tube Densimetry. *Langmuir* **2012**, *28*, 5070-5078.

(7) Rother, G.; Melnichenko, Y. B.; Cole, D. R.; Frielinghaus, H.; Wignall, G. D. Microstructural Characterization of Adsorption and Depletion Regimes of Supercritical Fluids in Nanopores†. *J. Phy. Chem. C* **2007**, *111*, 15736-15742.

(8) Arrhenius, S. Xxxi. On the Influence of Carbonic Acid in the Air Upon the Temperature of the Ground. *Phil. Magazine Series 5* **1896**, *41*, 237-276.

(9) Gaus, I. Role and Impact of CO_2–Rock Interactions During CO_2 Storage in Sedimentary Rocks. *Bull. Pol. Acad. Sci., Tech. Sci.* **2010**, *4*, 73-89.

(10) Institute, G. C. Large Scale Ccs Projects. http://www.globalccsinstitute.com/projects/large-scale-ccs-projects (accessed June 3).

(11) Himeno, S.; Komatsu, T.; Fujita, S. High-Pressure Adsorption Equilibria of Methane and Carbon Dioxide on Several Activated Carbons. *J. Chem. Eng. Data* **2005**, *50*, 369-376.

(12) Huang, L.; Zhang, L.; Shao, Q.; Lu, L.; Lu, X.; Jiang, S.; Shen, W. Simulations of Binary Mixture Adsorption of Carbon Dioxide and Methane in Carbon Nanotubes: Temperature, Pressure, and Pore Size Effects. *J. Phys Chem. C* **2007**, *111*, 11912-11920.

(13) Cavenati, S.; Grande, C. A.; Rodrigues, A. E. Adsorption Equilibrium of Methane, Carbon Dioxide, and Nitrogen on Zeolite 13X at High Pressures. *J. Chem. Eng. Data* **2004**, *49*, 1095-1101.

(14) Bleken, B.-T. L.; Lillerud, K. P.; Splith, T.; Pusch, A.-K.; Stallmach, F. PFG NMR Diffusion Measurements of CH_4 and CO_2 through Large ZSM-58-Crystals. *Microporous Mesoporous Mater.* **2013**, *182*, 25-31.

(15) Ohlin, L.; Bazin, P.; Thibault-Starzyk, F.; Hedlund, J.; Grahn, M. Adsorption of CO_2, CH_4, and H_2O in Zeolite ZSM-5 Studied Using in Situ Atr-Ftir Spectroscopy. *J. Phys Chem. C* **2013**, *117*, 16972-16982.

(16) Rosenbauer, R. J.; Thomas, B.; Bischoff, J. L.; Palandri, J. Carbon Sequestration Via Reaction with Basaltic Rocks: Geochemical Modeling and Experimental Results. *Geochim. Cosmochim. Ac.* **2012**, *89*, 116-133.

(17) Gislason, S. R.; Wolff-Boenisch, D.; Stefansson, A.; Oelkers, E. H.; Gunnlaugsson, E.; Sigurdardottir, H.; Sigfusson, B.; Broecker, W. S.; Matter, J. M.; Stute, M., et al. Mineral Sequestration of Carbon Dioxide in Basalt: A Pre-Injection Overview of the CarbFix Project. *Int. J. Greenh. Gas Control* **2010**, *4*, 537-545.

(18) Schaef, H. T.; McGrail, B. P.; Owen, A. T. Carbonate Mineralization of Volcanic Province Basalts. *Int. J. Greenh. Gas Control* **2010**, *4*, 249-261.

(19) Maiti, A. Atomistic Modeling toward High-Efficiency Carbon Capture: A Brief Survey with a Few Illustrative Examples. *Int. J. Greenh. Gas Control* **2014**, *114*, 163-175.

(20) Berndt, M. E.; Allen, D. E.; Seyfried, W. E. Reduction of CO_2 During Serpentinization of Olivine at 300°C and 500 Bar. *Geology* **1996**, *24*, 351-354.

(21) McCollom, T. M.; Seewald, J. S. A Reassessment of the Potential for Reduction of Dissolved CO_2 to Hydrocarbons During Serpentinization of Olivine. *Geochim. Cosmochim. Ac.* **2001**, *65*, 3769-3778.

(22) Johnson, J. K.; Panagiotopoulos, A. Z.; Gubbins, K. E. Reactive Canonical Monte Carlo. *Mol. Phys.* **1994**, *81*, 717-733.

(23) Smith, W. R.; Triska, B. The Reaction Ensemble Method for the Computer Simulation of Chemical and Phase Equilibria. I. Theory and Basic Examples. *J. Chem. Phys* **1994**, *100*, 3019-3027.

(24) Lemmon, E. W.; McLinden, M. O.; Friend, D. G. Thermophysical Properties of Fluid Systems. In *NIST Chemistry WebBook*; NIST Standard Reference Database Number 69; National Institute of Standards and Technology, Gaithersburg MD, 20899, http: //webbok.nist.gov, (retrived July 16, 2013).

(25) Argyris, D.; Cole, D. R.; Striolo, A. Hydration Structure on Crystalline Silica Substrates. *Langmuir* **2009**, *25*, 8025-8035.

(26) Ho, T. A.; Argyris, D.; Cole, D. R.; Striolo, A. Aqueous NaCl and CsCl Solutions Confined in Crystalline Slit-Shaped Silica Nanopores of Varying Degree of Protonation. *Langmuir* **2011**, *28*, 1256-1266.

(27) Ho, T. A.; Argyris, D.; Papavassiliou, D. V.; Striolo, A.; Lee, L. L.; Cole, D. R. Interfacial Water on Crystalline Silica: A Comparative Molecular Dynamics Simulation Study. *Mol. Simul.* **2011**, *37*, 172-195.

(28) Phan, A.; Ho, T. A.; Cole, D. R.; Striolo, A. Molecular Structure and Dynamics in Thin Water Films at Metal Oxide Surfaces: Magnesium, Aluminum, and Silicon Oxide Surfaces. *J. Phys Chem. C* **2012**, *116*, 15962-15973.

(29) Argyris, D.; Tummala, N. R.; Striolo, A.; Cole, D. R. Molecular Structure and Dynamics in Thin Water Films at the Silica and Graphite Surfaces. *J. Phys Chem. C* **2008**, *112*, 13587-13599.

(30) Rother, G.; Krukowski, E. G.; Wallacher, D.; Grimm, N.; Bodnar, R. J.; Cole, D. R. Pore Size Effects on the Sorption of Supercritical CO_2 in Mesoporous CPG-10 Silica. *J. Phys Chem. C* **2011**, *116*, 917-922.

(31) Salles, F.; Kolokolov, D. I.; Jobic, H.; Maurin, G.; Llewellyn, P. L.; Devic, T.; Serre, C.; Ferey, G. Adsorption and Diffusion of H_2 in the MOF Type Systems MIL-47(V) and MIL-53(Cr): A Combination of Microcalorimetry and QENS Experiments with Molecular Simulations. *J. Phys Chem. C* **2009**, *113*, 7802-7812.

(32) Martin, M. G.; Siepmann, J. I. Transferable Potentials for Phase Equilibria. 1. United-Atom Description of N-Alkanes. *J. Phys Chem. B* **1998**, *102*, 2569-2577.

(33) Berendsen, H. J. C.; Grigera, J. R.; Straatsma, T. P. The Missing Term in Effective Pair Potentials. *J. Phys. Chem.* **1987**, *91*, 6269-6271.

(34) Allen, M. P.; Tildesley, D. J. *Computer Simulation of Liquids*; Clarendon Pr.: Oxford, 2004.

(35) Cygan, R. T.; Liang, J.-J.; Kalinichev, A. G. Molecular Models of Hydroxide, Oxyhydroxide, and Clay Phases and the Development of a General Force Field. *J. Phys Chem. B* **2004**, *108*, 1255-1266.

(36) Prausnitz, J. M.; Lichtenthaler, R. N.; de Azevedo, E. G. *Molecular Thermodynamics of Fluid-Phase Equilibria*; American Institute of Chemical Engineers: Prentice Hall, New Jersey, 1998.

(37) Herzberg, G. *Electronic Spectra and Electronic Structure of Polyatomic Molecules*; Van Nostrand: New York, 1966.

(38) Huber, K. P.; Herzberg, G. *Molecular Spectra and Molecular Structure IV. Constants of Diatomic Molecules*; Van Nostrand: New York, 1979.

(39) Frank C. De Lucia; Paul Helminger; Kirchhoff, W. H. Microwave Spectra of Molecules of Astrophysical Interest, V. Water Vapor. *J. Phys. Chem. Ref. Data 3* **1974**, 211-219.

(40) Hockney, R. W.; Goel, S. P.; Eastwood, J. W. Quiet High-Resolution Computer Models of a Plasma. *J. Comput. Phys.* **1974**, *14*, 148-158.

(41) Bai, L.; Breen, D. Calculating Center of Mass in an Unbounded 2D Environment. *Journal of Graphics, GPU, and Game Tools* **2008**, *13*, 53-60.

(42) Hoover, W. G. Canonical Dynamics: Equilibrium Phase-Space Distributions. *Phys. Rev. A* **1985**, *31*, 1695-1697.

(43) Nosé, S. A Molecular Dynamics Method for Simulations in the Canonical Ensemble. *Mol. Phys.* **1984**, *52*, 255-268.

(44) Essmann, U.; Perera, L.; Berkowitz, M. L.; Darden, T.; Lee, H.; Pedersen, L. G. A Smooth Particle Mesh Ewald Method. *J. Chem. Phys.* **1995**, *103*, 8577-8593.

(45) Lísal, M.; Smith, W. R.; Nezbeda, I. Accurate Computer Simulation of Phase Equilibrium for Complex Fluid Mixtures. Application to Binaries Involving Isobutene, Methanol, Methyl Tert-Butyl Ether, and N-Butane. *J. Phys Chem. B* **1999**, *103*, 10496-10505.

(46) Lísal, M.; Smith, W. R.; Nezbeda, I. Accurate Vapour–Liquid Equilibrium Calculations for Complex Systems Using the Reaction Gibbs Ensemble Monte Carlo Simulation Method. *Fluid Phase Equilib.* **2001**, *181*, 127-146.

(47) Einstein, A. Über Die Von Der Molekularkinetischen Theorie Der Wärme Geforderte Bewegung Von in Ruhenden Flüssigkeiten Suspendierten Teilchen. *Annalen der Physik* **1905**, *322*, 549-560.

(48) Babarao, R.; Jiang, J. Diffusion and Separation of CO_2 and CH_4 in Silicalite, C168 Schwarzite, and IRMOF-1: A Comparative Study from Molecular Dynamics Simulation. *Langmuir* **2008**, *24*, 5474-5484.

(49) Jackson, R. B.; Vengosh, A.; Darrah, T. H.; Warner, N. R.; Down, A.; Poreda, R. J.; Osborn, S. G.; Zhao, K.; Karr, J. D. Increased Stray Gas Abundance in a Subset of Drinking Water Wells near Marcellus Shale Gas Extraction. *Proc. Natl. Acad. Sci. U.S.A.* **2013**.

(50) Yethiraj, A.; Striolo, A. Fracking: What Can Physical Chemistry Offer? *The Journal of Physical Chemistry Letters* **2013**, *4*, 687-690.

(51) Grande, C. A.; Rodrigues, A. E. Adsorption Equilibria and Kinetics of Propane and Propylene in Silica Gel. *Industrial & Engineering Chemistry Research* **2001**, *40*, 1686-1693.

(52) Rouquerol, J.; Avnir, D.; Fairbridge, C. W.; Everett, D. H.; Haynes, J. M.; Pernicone, N.; Ramsay, J. D. F.; Sing, K. S. W.; Unger, K. K. Recommendations for the Characterization of Porous Solids (Technical Report, IUPAC Recommendations). *Pure and Applied Chemistry* **1994**, *66*, 1739.

(53) Sing, K. S. W.; Everett, D. H.; Haul, R. A. W.; Moscou, L.; Pierotti, R. A.; Rouquerol, J.; Siemieniewska, T. Reporting Physisorption Data for Gas/Solid Systems with Special Reference to the Determination of Surface Area and Porosity (IUPAC Recommendations 1984). *Pure and Applied Chemistry* **1985**, *57*, 603-619.

(54) Monson, P. A. Understanding Adsorption/Desorption Hysteresis for Fluids in Mesoporous Materials Using Simple Molecular Models and Classical Density Functional Theory. *Microporous and Mesoporous Materials* **2012**, *160*, 47-66.

(55) Wu, J.; Li, Z. Density-Functional Theory for Complex Fluids. *Annual Review of Physical Chemistry* **2007**, *58*, 85-112.

(56) Ravikovitch, P. I.; Haller, G. L.; Neimark, A. V. Density Functional Theory Model for Calculating Pore Size Distributions: Pore Structure of Nanoporous Catalysts. *Advances in Colloid and Interface Science* **1998**, *76–77*, 203-226.

(57) Sarkisov, L.; Monson, P. A. Modeling of Adsorption and Desorption in Pores of Simple Geometry Using Molecular Dynamics. *Langmuir* **2001**, *17*, 7600-7604.

(58) Duren, T.; Bae, Y.-S.; Snurr, R. Q. Using Molecular Simulation to Characterise Metal-Organic Frameworks for Adsorption Applications. *Chemical Society Reviews* **2009**, *38*, 1237-1247.

(59) Nicholson, D.; Parsonage, N. G. *Computer Simulation and the Statistical Mechanics of Adsorption*; Academic Press, 1982.

(60) Striolo, A.; Chialvo, A. A.; Cummings, P. T.; Gubbins, K. E. Water Adsorption in Carbon-Slit Nanopores. *Langmuir* **2003**, *19*, 8583-8591.

(61) Striolo, A.; Gubbins, K. E.; Gruszkiewicz, M. S.; Cole, D. R.; Simonson, J. M.; Chialvo, A. A.; Cummings, P. T.; Burchell, T. D.; More, K. L. Effect of Temperature on the Adsorption of Water in Porous Carbons. *Langmuir* **2005**, *21*, 9457-9467.

(62) Jorge, M.; Schumacher, C.; Seaton, N. A. Simulation Study of the Effect of the Chemical Heterogeneity of Activated Carbon on Water Adsorption. *Langmuir* **2002**, *18*, 9296-9306.

(63) McCallum, C. L.; Bandosz, T. J.; McGrother, S. C.; Müller, E. A.; Gubbins, K. E. A Molecular Model for Adsorption of Water on Activated Carbon: Comparison of Simulation and Experiment. *Langmuir* **1998**, *15*, 533-544.

(64) Liu, J. C.; Monson, P. A. Monte Carlo Simulation Study of Water Adsorption in Activated Carbon. *Industrial & Engineering Chemistry Research* **2006**, *45*, 5649-5656.

(65) Puibasset, J.; Pellenq, R. Water Adsorption in Disordered Mesoporous Silica (Vycor) at 300K and 650K: A Grand Canonical Monte Carlo Simulation Study of Hysteresis. *The Journal of Chemical Physics* **2005**, *122*, 094704.

(66) Hung, F.; Bhattacharya, S.; Coasne, B.; Thommes, M.; Gubbins, K. Argon and Krypton Adsorption on Templated Mesoporous Silicas: Molecular Simulation and Experiment. *Adsorption* **2007**, *13*, 425-437.

(67) Gavalda, S.; Gubbins, K. E.; Hanzawa, Y.; Kaneko, K.; Thomson, K. T. Nitrogen Adsorption in Carbon Aerogels: A Molecular Simulation Study. *Langmuir* **2002**, *18*, 2141-2151.

(68) Müller, E. A.; Hung, F. R.; Gubbins, K. E. Adsorption of Water Vapor−Methane Mixtures on Activated Carbons. *Langmuir* **2000**, *16*, 5418-5424.

(69) Walton, K. S.; Millward, A. R.; Dubbeldam, D.; Frost, H.; Low, J. J.; Yaghi, O. M.; Snurr, R. Q. Understanding Inflections and Steps in Carbon Dioxide Adsorption Isotherms in Metal-Organic Frameworks. *Journal of the American Chemical Society* **2007**, *130*, 406-407.

(70) Yazaydın, A. O. z. r.; Benin, A. I.; Faheem, S. A.; Jakubczak, P.; Low, J. J.; Willis, R. R.; Snurr, R. Q. Enhanced CO_2 Adsorption in Metal-Organic Frameworks Via Occupation of Open-Metal Sites by Coordinated Water Molecules. *Chemistry of Materials* **2009**, *21*, 1425-1430.

(71) Macedonia, M. D.; Moore, D. D.; Maginn, E. J.; Olken, M. M. Adsorption Studies of Methane, Ethane, and Argon in the Zeolite Mordenite: Molecular Simulations and Experiments. *Langmuir* **2000**, *16*, 3823-3834.

(72) Larsen, G.; Lin, P.; Siperstein, F.; Colina, C. Methane Adsorption in PIM-1. *Adsorption* **2011**, *17*, 21-26.

(73) Abbott, L. J.; Colina, C. M. Atomistic Structure Generation and Gas Adsorption Simulations of Microporous Polymer Networks. *Macromolecules* **2011**, *44*, 4511-4519.

(74) Turner, A. R. *A Grand Canonical Monte Carlo Study of Adsorption on Graphite Surfaces with Defects*; University of Wales Bangor (Chemistry): UK, 1998.

(75) Rajput, N. N.; Monk, J.; Hung, F. R. Structure and Dynamics of an Ionic Liquid Confined inside a Charged Slit Graphitic Nanopore. *The Journal of Physical Chemistry C* **2012**, *116*, 14504-14513.

(76) Awati, R. V.; Ravikovitch, P. I.; Sholl, D. S. Efficient and Accurate Methods for Characterizing Effects of Framework Flexibility on Molecular Diffusion in Zeolites: CH_4 Diffusion in Eight Member Ring Zeolites. *The Journal of Physical Chemistry C* **2013**, *117*, 13462-13473.

(77) Lee, S. H.; Rasaiah, J. C. Molecular Dynamics Simulation of Ion Mobility. 2. Alkali Metal and Halide Ions Using the SPC/E Model for Water at 25 °C†. *The Journal of Physical Chemistry* **1996**, *100*, 1420-1425.

(78) Feng, H.; Gao, W.; Nie, J.; Wang, J.; Chen, X.; Chen, L.; Liu, X.; Lüdemann, H.-D.; Sun, Z. MD Simulation of Self-Diffusion and Structure in Some N-Alkanes over a Wide Temperature Range at High Pressures. *J. Mol. Model.* **2013**, *19*, 73-82.

(79) Lemmon, E. W.; McLinden, M. O.; Friend, D. G. Thermophysical Properties of Fluid Systems. NIST Standard Reference Database 69: NIST Chemistry Webbook. Http: //Webbook.Nist.Gov/Chemistry/Fluid/ (Accessed Oct, 2013).

(80) Teja, A. S.; Lee, R. J.; Rosenthal, D.; Anselme, M. Correlation of the Critical Properties of Alkanes and Alkanols. *Fluid Phase Equilibria* **1990**, *56*, 153-169.

(81) Everett, D. H.; Powl, J. C. Adsorption in Slit-Like and Cylindrical Micropores in the Henry's Law Region. A Model for the Microporosity of Carbons. *Journal of the Chemical Society, Faraday Transactions 1: Physical Chemistry in Condensed Phases* **1976**, *72*, 619-636.

(82) Do, D. D.; Do, H. D. Evaluation of 1-Site and 5-Site Models of Methane on Its Adsorption on Graphite and in Graphitic Slit Pores. *The Journal of Physical Chemistry B* **2005**, *109*, 19288-19295.

(83) Myers, A. L.; Monson, P. A. Adsorption in Porous Materials at High Pressure: Theory and Experiment. *Langmuir* **2002**, *18*, 10261-10273.

(84) Do, D. D.; Do, H. D.; Fan, C.; Nicholson, D. On the Existence of Negative Excess Isotherms for Argon Adsorption on Graphite Surfaces and in Graphitic Pores under Supercritical Conditions at Pressures up to 10,000 Atm. *Langmuir* **2010**, *26*, 4796-4806.

(85) Thommes, M. Physical Adsorption Characterization of Nanoporous Materials. *Chemie Ingenieur Technik* **2010**, *82*, 1059-1073.

(86) Wang, Y.; Mahle, J. J.; Furtado, A. M. B.; Glover, T. G.; Buchanan, J. H.; Peterson, G. W.; LeVan, M. D. Mass Transfer and Adsorption Equilibrium for Low Volatility Alkanes in BPL Activated Carbon. *Langmuir* **2013**, *29*, 2935-2945.

(87) Krekelberg, W. P.; Siderius, D. W.; Shen, V. K.; Truskett, T. M.; Errington, J. R. Connection between Thermodynamics and Dynamics of Simple Fluids in Highly Attractive Pores. *Langmuir* **2013**, *29*, 14527-14535.

(88) Mittal, J.; Errington, J. R.; Truskett, T. M. Thermodynamics Predicts How Confinement Modifies the Dynamics of the Equilibrium Hard-Sphere Fluid. *Phys. Rev. Lett.* **2006**, *96*, 177804.

(89) Kleine, H.; Eckhardt, M.; Fick, D. Mean Residence Time of Li Atoms Adsorbed on Si(100) and Si(111) Surfaces. *Surface Science* **1995**, *329*, 71-76.

(90) Cox, P. M.; Betts, R. A.; Jones, C. D.; Spall, S. A.; Totterdell, I. J. Acceleration of Global Warming Due to Carbon-Cycle Feedbacks in a Coupled Climate Model. *Nature* **2000**, *408*, 184-187.

(91) Jenkinson, D. S.; Adams, D. E.; Wild, A. Model Estimates of CO_2 Emissions from Soil in Response to Global Warming. *Nature* **1991**, *351*, 304-306.

(92) Thomas, C. D.; Cameron, A.; Green, R. E.; Bakkenes, M.; Beaumont, L. J.; Collingham, Y. C.; Erasmus, B. F. N.; de Siqueira, M. F.; Grainger, A.; Hannah, L., et al. Extinction Risk from Climate Change. *Nature* **2004**, *427*, 145-148.

(93) Gislason, S. R.; Oelkers, E. H. Carbon Storage in Basalt. *Science* **2014**, *344*, 373-374.

(94) Fathi, E.; Akkutlu, I. Y. In *Counter Diffusion and Competitive Adsorption Effects During CO_2 Injection and Coalbed Methane Production*, SPE Annual Technical Conference and Exhibition, Denver, Colorado, USA, Sept 21-24, 2008.

(95) Brochard, L.; Vandamme, M.; Pellenq, R. J. M.; Fen-Chong, T. Adsorption-Induced Deformation of Microporous Materials: Coal Swelling Induced by CO_2–CH_4 Competitive Adsorption. *Langmuir* **2011**, *28*, 2659-2670.

(96) White, C. M.; Smith, D. H.; Jones, K. L.; Goodman, A. L.; Jikich, S. A.; LaCount, R. B.; DuBose, S. B.; Ozdemir, E.; Morsi, B. I.; Schroeder, K. T. Sequestration of Carbon Dioxide in Coal with Enhanced Coalbed Methane Recoverya Review†. *Energy Fuels* **2005**, *19*, 659-724.

(97) Harpalani, S.; Prusty, B. K.; Dutta, P. Methane/ CO_2 Sorption Modeling for Coalbed Methane Production and CO_2 Sequestration. *Energy Fuels* **2006**, *20*, 1591-1599.

(98) Khosravi, M.; Bahramian, A.; Emadi, M.; Rostami, B.; Roayaie, E. Mechanistic Investigation of Bypassed-Oil Recovery During CO_2 Injection in Matrix and Fracture. *Fuel* **2014**, *117, Part A*, 43-49.

(99) Tudor, R.; Poleschuk, A. Low-Viscosity, Low-Temperature Fracture Fluids. *SPE* **1996**, *35*, 31-36.

(100) Niezgoda, T.; Miedzińska, D.; Małek, E.; Kędzierski, P.; Sławiński, G. Study on Carbon Dioxide Thermodynamic Behavior for the Purpose of Shale Rock Fracturing. *Bull. Pol. Acad. Sci., Tech. Sci.* **2013**, *61*, 605-612.

(101) Ishida, T.; Aoyagi, K.; Niwa, T.; Chen, Y.; Murata, S.; Chen, Q.; Nakayama, Y. Acoustic Emission Monitoring of Hydraulic Fracturing Laboratory Experiment with Supercritical and Liquid CO_2. *Geophys. Res. Lett.* **2012**, *39*, L16309.

(102) Wörmeyer, K.; Smirnova, I. Breakthrough Measurements of CO_2 through Aminofunctionalised Aerogel Adsorbent at Low Partial Pressure: Experiment and Modeling. *Microporous Mesoporous Mater.* **2014**, *184*, 61-69.

(103) Mueller, R.; Zhang, S.; Neumann, B.; Bäumer, M.; Vasenkov, S. Self-Diffusion of Carbon Dioxide in Samaria/Alumina Aerogel Catalyst Using High Field Nmr Diffusometry. *J. Chem. Phys* **2013**, *139*, 154703.

(104) Golzar, K.; Amjad-Iranagh, S.; Amani, M.; Modarress, H. Molecular Simulation Study of Penetrant Gas Transport Properties into the Pure and Nanosized Silica Particles Filled Polysulfone Membranes. *J. Membr. Sci.* **2014**, *451*, 117-134.

(105) Mebane, D. S.; Kress, J. D.; Storlie, C. B.; Fauth, D. J.; Gray, M. L.; Li, K. Transport, Zwitterions, and the Role of Water for CO_2 Adsorption in Mesoporous Silica-Supported Amine Sorbents. *J. Phys Chem. C* **2013**, *117*, 26617-26627.

(106) Ferey, G.; Serre, C.; Devic, T.; Maurin, G.; Jobic, H.; Llewellyn, P. L.; De Weireld, G.; Vimont, A.; Daturi, M.; Chang, J.-S. Why Hybrid Porous Solids Capture Greenhouse Gases? *Chem. Soc. Rev.* **2011**, *40*, 550-562.

(107) Le, T.; Striolo, A.; Cole, D. R. Propane Simulated in Silica Pores: Adsorption Isotherms, Molecular Structure, and Mobility. *Chem. Eng. Sci.* **2015**, *121*, 292-299.

(108) Arthur, M. A.; Cole, D. R. Unconventional Hydrocarbon Resources: Prospects and Problems. *Elements* **2014**, *10*, 257-264.

(109) Hirschfelder, J. O.; Curtiss, C. F.; Bird, R. B. *Molecular Theory of Gases and Liquids*; John Wiley & Sons: New York, 1964.

(110) Rother, G.; Vlcek, L.; Gruszkiewicz, M. S.; Chialvo, A. A.; Anovitz, L. M.; Bañuelos, J. L.; Wallacher, D.; Grimm, N.; Cole, D. R. Sorption Phase of Supercritical CO_2 in Silica Aerogel: Experiments and Mesoscale Computer Simulations. *J. Phys Chem. C* **2014**, *118*, 15525-15533.

(111) Arunan, E.; Desiraju, G. R.; Klein, R. A.; Sadlej, J.; Scheiner, S.; Alkorta, I.; Clary, D. C.; Crabtree, R. H.; Dannenberg, J. J.; Hobza, P., et al. Definition of the Hydrogen Bond (Iupac Recommendations 2011). *Pure Appl. Chem.* **2011**, *83*, 1637-1641.

(112) Sato, H.; Matubayasi, N.; Nakahara, M.; Hirata, F. Which Carbon Oxide Is More Soluble? Ab Initio Study on Carbon Monoxide and Dioxide in Aqueous Solution. *Chem. Phys. Lett.* **2000**, *323*, 257-262.

(113) Kärger, J.; Pfeifer, H. N.M.R. Self-Diffusion Studies in Zeolite Science and Technology. *Zeolites* **1987**, *7*, 90-107.

(114) Sholl, D. S. Testing Predictions of Macroscopic Binary Diffusion Coefficients Using Lattice Models with Site Heterogeneity. *Langmuir* **2006**, *22*, 3707-3714.

(115) Snurr, R. Q.; Kärger, J. Molecular Simulations and NMR Measurements of Binary Diffusion in Zeolites. *J. Phys Chem. B* **1997**, *101*, 6469-6473.

(116) Vidoni, A. Adsorption and Diffusion of Light Hydrocarbon in DDR Zeolite. Ph.D. Dissertation, The University of Maine, Orono, ME, 2011.

(117) Patankar, S.; Gautam, S.; Rother, G.; Podlesnyak, A.; Ehlers, G.; Liu, T.; Cole, D. R.; Tomasko, D. L. Role of Confinement on Adsorption and Dynamics of Ethane and an Ethane–CO_2 Mixture in Mesoporous Cpg Silica. *J. Phys Chem. C* **2016**, *120*, 4843-4853.

(118) Zhou, J.; Lu, X.; Wang, Y.; Shi, J. Molecular Dynamics Investigation on the Infinite Dilute Diffusion Coefficients of Organic Compounds in Supercritical Carbon Dioxide. *Fluid Phase Equilib.* **2000**, *172*, 279-291.

(119) Elliott, R. W.; Watts, H. Diffusion of Some Hydrocarbons in Air: A Regularity in the Diffusion Coefficients of a Homologous Series. *Can. J. Chem.* **1972**, *50*, 31-34.

(120) Goel, G.; Krekelberg, W. P.; Errington, J. R.; Truskett, T. M. Tuning Density Profiles and Mobility of Inhomogeneous Fluids. *Phys. Rev. Lett.* **2008**, *100*, 106001.

(121) Le, T.; Striolo, A.; Cole, D. R. CO_2–C_4H_{10} Mixtures Simulated in Silica Slit Pores: Relation between Structure and Dynamics. *J. Phys Chem. C* **2015**, *119*, 15274-15284.

(122) Kaneko, K.; Cracknell, R. F.; Nicholson, D. Nitrogen Adsorption in Slit Pores at Ambient Temperatures: Comparison of Simulation and Experiment. *Langmuir* **1994**, *10*, 4606-4609.

(123) McCollom, T. M.; Seewald, J. S. Abiotic Synthesis of Organic Compounds in Deep-Sea Hydrothermal Environments. *Chem. Rev.* **2007**, *107*, 382-401.

(124) Shock, E. Chemical Environments of Submarine Hydrothermal Systems. *Origins Life Evol Biosphere* **1992**, *22*, 67-107.

(125) Shock, E. L. Geochemical Constraints on the Origin of Organic Compounds in Hydrothermal Systems. *Origins Life Evol Biosphere*, *20*, 331-367.

(126) Helgeson, H. C.; Delany, J. M.; Nesbitt, H. W.; Bird, D. K. *Summary and Critique of the Thermodynamic Properties of Rock Forming Minerals*: New Haven, Connecticut, 1978; Vol. 278A.

(127) Chou, I.-M. Oxygen Buffer and Hydrogen Sensor Techniques at Elevated Pressures and Temperatures. In *Hydrothermal Experimental Techniques*, Ulmer, G. C.; Barnes, H. L., Eds. Wiley-Interscience: New York, 1987; 61-99.

(128) Chou, I. M. Calibration of Oxygen Buffers at Elevated P and T Using the Hydrogen Fugacity Sensor. *Am. Mineral.* **1978**, *63*, 690-703.

(129) Swickrath, M. J.; Anderson, M., The Development of Models for Carbon Dioxide Reduction Technologies for Spacecraft Air Revitalization. In *42nd International Conference on Environmental Systems (ICES)*, San Diego, CA; United States 2011.

(130) Gao, J.; Wang, Y.; Ping, Y.; Hu, D.; Xu, G.; Gu, F.; Su, F. A Thermodynamic Analysis of Methanation Reactions of Carbon Oxides for the Production of Synthetic Natural Gas. *RSC Adv.* **2012**, *2*, 2358-2368.

(131) Holm, N. G. *Marine Hydrothermal Systems and the Origin of Life : Report of Scor Working Group 91.*; Kluwer: Dordrecht, 1992.

(132) N.G., H.; E.M., A. *The Molecular Origin of Life*; Cambridge University Press: Cambridge, UK, 1998.

(133) Martin, W.; Baross, J.; Kelley, D.; Russell, M. J. Hydrothermal Vents and the Origin of Life. *Nat. Rev. Micro.* **2008**, *6*, 805-814.

(134) McCollom, T. M.; Seewald, J. S. Serpentinites, Hydrogen, and Life. *Elements* **2013**, *9*, 129-134.

(135) McCollom, T. M. Laboratory Simulations of Abiotic Hydrocarbon Formation in Earth’s Deep Subsurface. *Rev. Mineral. Geochem.* **2013**, *75*, 467-494.

(136) Proskurowski, G.; Lilley, M. D.; Seewald, J. S.; Früh-Green, G. L.; Olson, E. J.; Lupton, J. E.; Sylva, S. P.; Kelley, D. S. Abiogenic Hydrocarbon Production at Lost City Hydrothermal Field. *Science* **2008**, *319*, 604-607.

(137) Müntener, O. Serpentine and Serpentinization: A Link between Planet Formation and Life. *Geology* **2010**, *38*, 959-960.

(138) Früh-Green, G. L. The Lost City 2005 Expedition. http://oceanexplorer.noaa.gov/explorations/05lostcity/background/serp/serpentinization.html (accessed September 2016).

(139) McCollom, T. M.; Seewald, J. S. Experimental Constraints on the Hydrothermal Reactivity of Organic Acids and Acid Anions: I. Formic Acid and Formate. *Geochim. Cosmochim. Ac.* **2003**, *67*, 3625-3644.

(140) Shilobreeva, S.; Martinez, I.; Busigny, V.; Agrinier, P.; Laverne, C. Insights into C and H Storage in the Altered Oceanic Crust: Results from ODP/IODP Hole 1256d. *Geochim. Cosmochim. Ac.* **2011**, *75*, 2237-2255.

(141) Foustoukos, D. I.; Seyfried, W. E. Hydrocarbons in Hydrothermal Vent Fluids: The Role of Chromium-Bearing Catalysts. *Science* **2004**, *304*, 1002-1005.

(142) Cole, D. R.; Ok, S.; Striolo, A.; Phan, A. Hydrocarbon Behavior at Nanoscale Interfaces. *Rev. Mineral. Geochem.* **2013**, *75*, 495-545.

(143) Argyris, D.; Ho, T.; Cole, D. R.; Striolo, A. Molecular Dynamics Studies of Interfacial Water at the Alumina Surface. *J. Phys Chem. C* **2011**, *115*, 2038-2046.

(144) Phan, A.; Ho, T. A.; Cole, D.; Striolo, A. Molecular Structure and Dynamics in Thin Water Films at Metal Oxide Surfaces: Magnesium, Aluminum, and Silicon Oxide Surfaces. *J. Phys Chem. C* **2012**, *116*, 15962-15973.

(145) Ho, T. A.; Argyris, D.; Papavassiliou, D. V.; Striolo, A.; Lee, L. L.; Cole, D. R. Interfacial Water on Crystalline Silica: A Comparative Molecular Dynamics Simulation Study. *Mol. Simul.* **2011**, *37*, 172-195.

(146) Ho, T. A.; Argyris, D.; Cole, D.; Striolo, A. Aqueous NaCl and CsCl Solutions Confined in Crystalline Slit-Shaped Silica Nanopores of Varying Degree of Protonation. *Langmuir* **2011**, *28*, 1256-1266.

(147) Kalluri, R.; Ho, T.; Biener, J.; Biener, M.; Striolo, A. Partition and Structure of Aqueous NaCl and $CaCl_2$ Electrolytes in Carbon-Slit Electrodes. *J. Phys Chem. C* **2013**, *117*, 13609-13619.

(148) Ho, T. A.; Striolo, A. Water and Methane in Shale Rocks: Flow Pattern Effects on Fluid Transport and Pore Structure. *AlChE J.* **2015**, *61*, 2993-2999.

(149) Phan, A.; Cole, D. R.; Striolo, A. Factors Governing the Behaviour of Aqueous Methane in Narrow Pores. *Phil. Trans. R. Soc. A* **2016**, *374*, 20150019.

(150) Le, T.; Ogbe, S.; Striolo, A.; Cole, D. R. N-Octane Diffusivity Enhancement Via Carbon Dioxide in Silica Slit-Shaped Nanopores – a Molecular Dynamics Simulation. *Mol. Simul.* **2015**, *121*, 1-8.

(151) Santiso, E. E.; George, A. M.; Sliwinska-bartkowiak, M.; Nardelli, M. B.; Gubbins, K. E. Effect of Confinement on Chemical Reactions. *Adsorption* **2005**, *11*, 349-354.

(152) Turner, C. H.; Brennan, J. K.; Johnson, J. K.; Gubbins, K. E. Effect of Confinement by Porous Materials on Chemical Reaction Kinetics. *J. Chem. Phys* **2002**, *116*, 2138-2148.

(153) Turner, C. H.; Johnson, J. K.; Gubbins, K. E. Effect of Confinement on Chemical Reaction Equilibria: The Reactions $2NO \Leftrightarrow (NO)_2$ and $N_2+3H_2 \Leftrightarrow 2NH_3$ in Carbon Micropores. *J. Chem. Phys* **2001**, *114*, 1851-1859.

(154) Turner, C. H.; Gubbins, K. E. Effects of Supercritical Clustering and Selective Confinement on Reaction Equilibrium: A Molecular Simulation Study of the Esterification Reaction. *J. Chem. Phys* **2003**, *119*, 6057-6067.

(155) Turner, C. H.; Pikunic, J.; Gubbins, K. E. Influence of Chemical and Physical Surface Heterogeneity on Chemical Reaction Equilibria in Carbon Micropores. *Mol. Phys.* **2001**, *99*, 1991-2001.

(156) Turner, C. H.; Brennan, J. K.; Lísal, M.; Smith, W. R.; Karl Johnson, J.; Gubbins, K. E. Simulation of Chemical Reaction Equilibria by the Reaction Ensemble Monte Carlo Method: A Review†. *Mol. Simul.* **2008**, *34*, 119-146.

(157) Ingebritsen, S. E.; Geiger, S.; Hurwitz, S.; Driesner, T. Numerical Simulation of Magmatic Hydrothermal Systems. *Rev. Geophys.* **2010**, *48*, RG1002.

(158) Ross, M. A High-Density Fluid-Perturbation Theory Based on an Inverse 12th-Power Hard-Sphere Reference System. *J. Chem. Phys* **1979**, *71*, 1567-1571.

(159) Cummings, P. T.; Stell, G. Statistical Mechanical Models of Chemical Reactions. *Mol. Phys.* **1984**, *51*, 253-287.

(160) Cummings, P. T.; Stell, G. Statistical Mechanical Models of Chemical Reactions. *Mol. Phys.* **1985**, *55*, 33-48.

(161) Cummings, P. T.; Stell, G. Statistical Mechanical Models of Chemical Reactions. *Mol. Phys.* **1987**, *60*, 1315-1342.

(162) Santiso, E. E.; Gubbins, K. E. Multi-Scale Molecular Modeling of Chemical Reactivity. *Mol. Simul.* **2004**, *30*, 699-748.

(163) Brenner, D. W. Empirical Potential for Hydrocarbons for Use in Simulating the Chemical Vapor Deposition of Diamond Films. *Phys. Rev. B* **1990**, *42*, 9458-9471.

(164) Elert, M. L.; Zybin, S. V.; White, C. T. Molecular Dynamics Study of Shock-Induced Chemistry in Small Condensed-Phase Hydrocarbons. *J. Chem. Phys* **2003**, *118*, 9795-9801.

(165) van Duin, A. C. T.; Dasgupta, S.; Lorant, F.; Goddard, W. A. ReaxFF: A Reactive Force Field for Hydrocarbons. *J. Phys Chem. A* **2001**, *105*, 9396-9409.

(166) Johnson, J. K. *Reactive Canonical Monte Carlo, in Advances in Chemical Physics: Monte Carlo Methods in Chemical Physics*; John Wiley & Sons, Inc.: Hoboken, NJ, USA., 1999; Vol. 105.

(167) Shaw, M. S. Monte Carlo Simulation of Equilibrium Chemical Composition of Molecular Fluid Mixtures in the Natoms Pt Ensemble. *J. Chem. Phys* **1991**, *94*, 7550-7553.

(168) Lísal, M.; Smith, W. R.; Nezbeda, I. Computer Simulation of the Thermodynamic Properties of High-Temperature Chemically-Reacting Plasmas. *J. Chem. Phys* **2000**, *113*, 4885-4895.

(169) Lísal, M.; Smith, W. R.; BureŠ, M.; Vacek, V.; NavrÁTil, J. Remc Computer Simulations of the Thermodynamic Properties of Argon and Air Plasmas. *Mol. Phys.* **2002**, *100*, 2487-2497.

(170) Brennan, J. K.; Rice, B. M. Molecular Simulation of Shocked Materials Using the Reactive Monte Carlo Method. *Phys. Rev. E* **2002**, *66*, 021105.

(171) Bezkrovniy, V.; Schlanges, M.; Kremp, D.; Kraeft, W. D. Reaction Ensemble Monte Carlo Technique and Hypernetted Chain Approximation Study of Dense Hydrogen. *Phys. Rev. E* **2004**, *69*, 061204.

(172) Borówko, M.; Zagórski, R. Chemical Equilibria in Slitlike Pores. *J. Chem. Phys* **2001**, *114*, 5397-5403.

(173) Cheung, J. K.; Shen, V. K.; Errington, J. R.; Truskett, T. M. Coarse-Grained Strategy for Modeling Protein Stability in Concentrated Solutions. III: Directional Protein Interactions. *Biophys. J.* **2007**, *92*, 4316-4324.

(174) Turner, C. H. Monte Carlo Simulation of Equilibrium Reactions at Modified Vapor−Liquid Interfaces. *Langmuir* **2007**, *23*, 2525-2530.

(175) Fujita, S.; Terunuma, H.; Kobayashi, H.; Takezawa, N. Methanation of Carbon Monoxide and Carbon Dioxide over Nickel Catalyst under the Transient State. *React. Kinet. Catal. Lett.* **1987**, *33*, 179-184.

(176) Schild, C.; Wokaun, A.; Baiker, A. On the Mechanism of CO and CO_2 Hydrogenation Reactions on Zirconia-Supported Catalysts: A Diffuse Reflectance Ftir Study. *J. Mol. Catal.* **1990**, *63*, 243-254.

(177) Sleep, N. H.; Bird, D. K.; Pope, E. C. Serpentinite and the Dawn of Life. *Phil. Trans. R. Soc. B* **2011**, *366*, 2857-2869.

(178) Jacquemin, M.; Beuls, A.; Ruiz, P. Catalytic Production of Methane from CO_2 and H_2 at Low Temperature: Insight on the Reaction Mechanism. *Catal. Today* **2010**, *157*, 462-466.

(179) Thampi, K. R.; Kiwi, J.; Gratzel, M. Methanation and Photo-Methanation of Carbon Dioxide at Room Temperature and Atmospheric Pressure. *Nature* **1987**, *327*, 506-508.

(180) Park, J.-N.; McFarland, E. W. A Highly Dispersed Pd–Mg/SiO_2 Catalyst Active for Methanation of CO_2. *J. Catal.* **2009**, *266*, 92-97.

(181) Li, T. D.; Gao, J. P.; Szoszkiewicz, R.; Landman, U.; Riedo, E. *Phys. Rev. B* **2007**, *75*, 115415.

(182) III, R. D. J.; Richter, U.; Manichaikul, A.; Schneider, B.; Acevedo, C.; Cockrell, B.; Minne, E.; Reed, J.; Parsons, M.; Fahey, M. NIST Computational Chemistry Comparison and Benchmark Database. NIST Standard Reference Database 101. Release 17b. http://cccbdb.nist.gov/ (accessed October 2015).

(183) McDermott, J. M.; Seewald, J. S.; German, C. R.; Sylva, S. P. Pathways for Abiotic Organic Synthesis at Submarine Hydrothermal Fields. *Proc. Natl. Acad. Sci.* **2015**, *112*, 7668-7672.

(184) Hanano, M. Two Roles of Fractures in Geothermal Development Contribution to Occurrence of Geothermal Resources and Well Production. *J. Geoth. Res. Soc. Japan* **2000**, *22*, 107-116.

(185) Singwi, K. S.; Sjölander, A. Diffusive Motions in Water and Cold Neutron Scattering. *Phy. Rev.* **1960**, *119*, 863-871.

(186) Gautam, S.; Liu, T.; Rother, G.; Jalarvo, N.; Mamontov, E.; Welch, S.; Sheets, J.; Droege, M.; Cole, D. R. Dynamics of Propane in Nanoporous Silica Aerogel: A Quasielastic Neutron Scattering Study. *J. Phys Chem. C* **2015**, *119*, 18188-18195.

(187) Berthelot, D. Sur Le Mélange Des Gaz. *Comptes rendus hebdomadaires des séances de l'Académie des Sciences* **1898**, 1703-1855.

(188) Lorentz, H. A. Ueber Die Anwendung Des Satzes Vom Virial in Der Kinetischen Theorie Der Gase. *Annalen der Physik* **1881**, *248*, 127-136.

(189) Gautam, S.; Liu, T.; Patankar, S.; Tomasko, D.; Cole, D. Location Dependent Orientational Structure and Dynamics of Ethane in ZSM-5. *Chem. Phys. Lett.* **2016**, *648*, 130-136.

(190) Jobic, H.; Bée, M.; Kearley, G. J. Dynamics of Ethane and Propane in Zeolite ZSM-5 Studied by Quasi-Elastic Neutron Scattering. *Zeolites* **1992**, *12*, 146-151.

(191) Gautam, S.; Cole, D. Molecular Dynamics Simulation Study of Meso-Confined Propane in TiO_2. *Chem. Phys.* **2015**, *458*, 68-76.